SPATIAL AND TEMPORAL VARIABILITY OF TORNADIC VERSUS NON-TORNADIC HIGH-SHEAR, LOW-CAPE ENVIRONMENTS

by

Lindsay Nicole Hochstatter

A thesis submitted to the faculty of
The University of North Carolina at Charlotte
in partial fulfillment of the requirements
for the degree of Master of Science in
Earth Science

Charlotte

2021

Approved by:

_____
Dr. Casey Davenport

_____
Mr. Terry Shirley

_____
Dr. Keith Sherburn

ABSTRACT

LINDSAY NICOLE HOCHSTATTER. Spatial and Temporal Variability of Tornadic versus Non-Tornadic High-Shear, Low-Cape Environments. (Under the direction of DR. CASEY DAVENPORT)

High-shear low-CAPE (HSLC) severe weather events, defined as those in which surface-based CAPE is below 500 J/kg and most unstable CAPE is less than 1000 J/kg and have a 0-6 km bulk wind difference of at least 18 m/s, are uniquely challenging to forecasters due to their rapid evolution times and relatively infrequent production of severe weather. Additionally, these environments tend to occur during the cool season and overnight hours, which present their own challenges in terms of current conceptual understanding, forecaster verification, and societal impacts.

To better understand how rapid environmental evolution contributes to severe weather production in HSLC environments, 224 tornado reports from HSLC events in the southeastern U.S. between 2014-2018 were categorized based on their radar signature near the time of tornadogenesis. More than half of the reports were from supercells, with the next largest contributor being bowing segments. Next, Rapid Refresh (RAP) model analysis soundings are used to characterize the near-storm environment and its spatiotemporal evolution, focusing on the time of tornadogenesis, as well as the hour before. For comparison, two other storm-relative locations (offset to the north and south, forming a grid) also had their environmental changes quantified. Perhaps unsurprisingly, as is also the case for radar signals of HSLC tornadogenesis, many of the observed environmental differences were very subtle. The most useful parameters for mesoanalysis as events unfold appear to be related to environmental moisture, as instability uniquely decreases preceding tornadogenesis for many cases within the dataset, and kinematic variables show very marginal changes. The key for increased potential for tornadogenesis

appears to be most directly related to the spatial variations in surface and mid-level moisture, both of which are most favorably enhanced at the tornadic inflow environment.

ACKNOWLEDGEMENTS

I would like to thank Dr. Casey Davenport for being the most supportive, flexible, and encouraging advisor anyone could ask for, and for challenging me to become a better scientist. I truly could not have navigated these strange times without your guidance – and I've completed a project I'm really proud of as a result! Thank you to the other members of my committee, Dr. Keith Sherburn and Mr. Terry Shirley, for their suggestions in refining the vision for my thesis and for putting up with my frantic scheduling emails. To the other former inhabitants of MCE 426, thank you for the endless impromptu tension relief sessions (from slingshots to Guess Who…but with hurricanes to Halloween candy rankings), coding advice, and too-long lunch breaks. That room could've used soundproof walls to muffle the ridiculous laughter, but I enjoyed every day I spent on campus because of all of you. Anna, Katie, and Sarah: you guys are the best girl squad I could've asked for. To my friends, family, and fiancé Bennett, thank you for loving me, for supporting me, and for believing in me even when I didn't think I'd make it to the defense.

Finally, thank you to melatonin, the cloth mask, and açai bowls for helping me (mentally and physically) make it through the pandemic that plagued almost 3/4 of my graduate school experience.

TABLE OF CONTENTS

LIST OF TABLES

LIST OF FIGURES

LIST OF ABBREVIATIONS

ACCB	buoyant acceleration
ACCD	dynamic acceleration
BWER	bounded weak echo region
CAPE	convective available potential energy
EF	enhanced Fujita
EHI	energy helicity index
EL	equilibrium level
ESHR	effective layer shear
FAR	false alarm rate
HSLC	high shear, low CAPE
KDGX	Jackson, Mississippi NEXRAD Radar
KFFC	Peachtree City, Georgia NEXRAD Radar
KGSP	Greer, South Carolina NEXRAD Radar
KGWX	Columbus, Mississippi NEXRAD Radar
KMXX	Maxwell, Alabama NEXRAD Radar
LLLR	low-level lapse rate
LR75	700-500 hPa lapse rate
MCS	mesoscale convective system
MLCAPE	mixed-layer convective available potential energy
MLCIN	mixed-layer convective inhibition
MOSH	Modified Severe Hazards in Environments with Reduced Buoyancy
MUCAPE	most-unstable convective available potential energy

MUCIN	most-unstable convective inhibition
NCEI	National Centers for Environmental Information
NEXRAD	next-generation radar
NST	non-supercell tornado
NWSWFO	National Weather Service weather forecast office
POD	probability of detection
QLCS	quasi-linear convective system
RAP	Rapid Refresh model
S3MG	0-3 km shear magnitude
SBCAPE	surface-based convective available potential energy
SBCIN	surface-based convective inhibition
SHERB	Severe Hazards in Environments with Reduced Buoyancy
SHERBE	Severe Hazards in Environments with Reduced Buoyancy, effective layer shear variant
SHERBS3	Severe Hazards in Environments with Reduced Buoyancy, 0-3 km shear variant
SPC	Storm Prediction Center
SRH	storm relative helicity
STP	significant tornado parameter
SWEA	Severe Weather Event Archive
UTC	Coordinated Universal Time
VPPGA	total vertical perturbation pressure gradient accelerations
WSR-88D	Weather Surveillance Radar 88 Doppler

I. Introduction and Motivation

A wide variety of instability and vertical wind shear combinations are conducive to the production of severe and tornadic storms (e.g., Brooks et al. 2003). Commonly, these events occur in high instability, high shear environments, though a notable subset occurs outside this norm. High-shear, low-CAPE (HSLC) severe weather events are defined as those with surface-based convective available potential energy (SBCAPE) ≤ 500 J/kg, or most-unstable CAPE (MUCAPE) ≤ 1000 J/kg to eliminate instances of elevated convection (Sherburn and Parker 2014), and 0-6 km bulk shear magnitude ≥ 18 m/s (35 kts). Deep moist convection that occurs in the presence of high instability is commonly the focal point of scientific investigations and publications, leaving its low instability complement less studied and less understood. Most of the existing pool of research into these environments consists of case studies of individual storms and climatologies of the synoptic features that lead to the development of these environments, with most agreement on the ingredient constraints for HSLC events coming in just the past 15 years.

Despite having reduced instability, HSLC events contribute to a modest percentage of annual tornado reports, including 63% of strong-violent tornadoes as identified by Schneider et al. (2006), though their definition includes a MLLCL constraint (≤ 1000m) and a low level (0-1 km) shear constraint (≥ 10 m/s), and present more frequently than high-shear, high-CAPE environments (Dean and Schneider 2008; Schneider and Dean 2008; Anderson-Frey et al. 2016). HSLC setups pose significant challenges to operational forecasters, as is evident by their existence within the high false-alarm rate and low probability-of-detection portion of the forecasting efficacy matrix (Dean and Schneider 2008; Schneider and Dean 2008). HSLC events are most common during the cool season when situational awareness of severe threats is lower,

and present most frequently in the southeastern United States, which presents its own difficulties in terms of demographics, population density, and topography (Ashley 2007; Ashley and Strader 2016). By definition, HSLC events are characterized by low CAPE, making CAPE-based diagnostic parameters, such as the significant tornado parameter (STP) or energy helicity index (EHI), fail to accurately represent the severe threat they pose (Sherburn and Parker 2014). Simulations and observations have shown that HSLC events tend to evolve rapidly, especially those classified as severe (King et al. 2017). This rapid environmental evolution combined with the compact nature of HSLC vortices (Markowski and Straka 2000; Cope 2004; Lane and Moore 2006) makes reliance on NEXRAD radar and previously forecasted quantities difficult.

Current recommended guidance for forecasters is based in pattern recognition (Lane and Moore 2006) of characteristic radar presentations, which include both supercellular and non-supercellular modes (Davis and Parker 2014). This study utilizes a large dataset of tornado reports from within HSLC environments, with the goal of first classifying tornado reports based on their primary radar signature, and then quantifying the environmental variability (both temporal and spatial) of tornadic versus non-tornadic portions of an HSLC event to enhance short-term forecasts and warnings of HSLC convective events. In the process, some operationally relevant avenues will be explored, including the frequency of signature type by time of day and distribution of tornadoes and intensity by signature type.

II. Background

A. Synoptic and Mesoscale Environment

The earliest research conducted in the realm of low instability severe environments focused on profiling single storms or storm systems through detailed case studies (Markowski and Straka 2000; Cope 2004; Lane and Moore 2006; Clark 2009). These examinations identified a common thread of strong synoptic-scale support contributing to their severity, in contrast to other severe events with reduced buoyancy (e.g., mini-supercells; Markowski and Straka 2000). Progressive, frequently negatively tilted mid-to-upper-level shortwave troughs on the fringes of the severe environment (e.g., Fig. 2.1) provided the framework for the development of modest instability (Markowski and Straka 2000; Cope 2004; Lane and Moore 2006; Clark 2009). The strong observed values of low-to-mid level shear that characterize HSLC events require the influence of potent upper-level jet streaks and low-level jets (Cope 2004; Lane and Moore 2006). In both of the events documented by Cope (2004) and Lane and Moore (2006), the favorable left exit region of an upper-level jet served to locally enhance available lift, bolstering the weak instability, while increased vertical shear allowed for organization of the convection that formed. Evans (2010) found that progressive cold fronts were the driving surface feature behind 70% of the cool season HSLC events that affected National Weather Service Forecast Office (NWSFO) Binghamton. Cold frontal advancement plays a role in further enhancing SRH in the atmospheric column (Cope 2004) by inducing localized veering (Apsley et al. 2016) and is also commonly coincident with large scale dry slots (Lane and Moore 2006; Clark 2009) that steepen lapse rates, providing a boost to marginal values of CAPE.

Given that updraft strength is inherently (though not solely) a function of instability, storms that form in HSLC environments fundamentally possess weaker updrafts than their high

instability counterparts (Markowski and Straka 2000). These typically less-energetic updrafts lead to suppression of storm depth, and as a result, HSLC storms and mesovortices are shallower than the classic convention found in the Great Plains (Markowski and Straka 2000; Cope 2004). Recent work by Wade and Parker (2021) showed that the shallowness of HSLC supercellular mesovortices can be attributed to the inability of the reduced buoyancy in the environment to overcome downward total dynamic acceleration at the upper extent of the low-level mesocyclone (Figs. 2.2-2.4). Tornadic storms in these environments are associated with the highest values of SRH (Cope 2004; Clark 2009) and wind shear (Lane and Moore 2006; Clark 2009) concentrated in the lowest 3 km of the atmosphere (i.e., large values of 0-3 km SRH and wind shear). This marked vortex shallowness is a major contributor to the difficulties associated with forecasting HSLC events, largely in part to the reliance on radar observations. The radar beam notably curves away from the earth with increasing range, leading to these shallow vortices potentially being overtopped and thus not sampled, especially for those that form in radar-spare areas.

B. Radar Appearance and Storm Organization

Severe weather forecasting relies heavily on WSR 88Ds, which have limited sampling capabilities for the shallow storms that characterize HSLC events over long distances. Davis and Parker (2014) found that false alarm rates (FAR) and frequency of signatures associated with non-supercellular HSLC mesovortices decrease between 60-100 km from the radar, with only 27% of their dataset falling within 60 km of the radar with improved resolution and probability of detection (POD). HSLC storm systems have been observed to organize in a variety of different ways, from discrete supercells with all the trappings of their high instability cousins (Markowski and Straka 2000), to subtle, even transient, features embedded within lines of convection, known as quasi-linear convective systems (QLCSs). Cope (2004) investigated a line

of storms that produced multiple tornadoes as it traversed New England, and after analyzing radar data, found that these reports were associated with notches and weak bowing that would "normally not justify a warning." Davis and Parker (2014) identified and defined a subset of radar signatures commonly associated with HSLC non-supercell mesovortices: gust front cusps, forward and rear inflow notches, broken-S's, and bowing segments; to ensure uniformity in the identification of the aforementioned radar signatures, a detailed description was developed for each (Fig. 2.5). Supercell mesovortices were identified via archived radar data by confirming the presence of a hook echo, defined as an appendage in the 40 dBZ reflectivity contour on the right rear flank of the storm, and a bounded weak echo region (BWER), characterized by a hole of sub-40 dBZ reflectivity bounded by 50+ dBZ reflectivity above, in the vicinity of the hook (Davis and Parker 2014).

HSLC non-supercell mesovortices are commonly less pronounced than those associated with discrete supercells, and forecasters may be less informed with their radar presentation. Gust front cusps are inflection points viewable in radial velocity data, and typically appear as an appendage in the 40 dBZ reflectivity contour, as shown in Fig. 2.6c. Forward and rear inflow notches are indentations in 40 dBZ reflectivity, occurring on opposite sides of a line of convection, as illustrated in Fig. 2.6a, d. Bowing segments are surging, convex segments of 40 dBZ reflectivity, commonly seen in QLCS-type HSLC convection (e.g., Fig. 2.6b). Broken-S signatures are characterized by a clean or nearly clean break in the 40 dBZ contour in a line of convection, and specifically in those cases where the southern portion of the break surges ahead of the northern portion. In the case of the broken-S, the mechanisms behind its formation are still relatively unknown, making it difficult to anticipate when a line break will result in tornadogenesis.

Tornado vortex signatures (TVS) typically present as tight couplets in radial velocity, but those in the Cope (2004) study featured only 40 knots of gate-to-gate shear at peak intensity. While not all HSLC tornadoes are weak, as they accounted for 63% of strong-violent tornadoes as identified by Schneider et al. (2006), those that are shallow, spin-up type tornadoes push the limits of radar scan capabilities. For example, analysis of a non-supercell tornado (NST) event near NWSFO Greenville-Spartanburg by Lane and Moore (2006) suggested that by the time a relevant broken-S-type signature would be visible on radar reflectivity, the next velocity scan may be too late to pick up on a TVS. Indeed, Davis and Parker (2014) found that the median lead time for more than 50% of signatures associated with QLCS mesovortices, bowing segments, gust-front cusps, and forward-inflow notches, was just 5 minutes. The transient nature of prognostic radar signatures and the lack of stringent forecasting guidelines make forecasting QLCS tornadogenesis one of the more pertinent challenges presented to operational forecasters.

C. Severe vs. Non-Severe HSLC Convection

The frequency and atypical presentation of HSLC events pushes the identification of precursor environmental conditions that differentiate between severe and non-severe events to the forefront of research, in terms of both importance and applicability. Prognostic radar signatures give lead time on the order of minutes, while homing in on the most important environmental contributors to the development of HSLC tornadogenesis allows for operational anticipation in the hours leading to convective development. On the broad scale, in terms of the development of HSLC tornadoes, the most favorable overlap of strong shear and CAPE falls in the Ohio, Tennessee, and Mississippi Valleys (Sherburn et al. 2016; Fig 2.7a). Schneider et al. (2006) performed the first comprehensive climatology of storm environments associated with all

severe reports in selected years and revealed that tornadoes in the southeast US and mid-Atlantic are characterized by strong deep layer shear and mixed-layer CAPE (MLCAPE) ≤ 1000 J/kg. Further, 63% of the strong (EF2+) tornadoes recorded during 2004-2005 fall in this low MLCAPE portion of the parameter space, with 56% of these occurring in the cool season. Synoptically, investigation into the climatology of HSLC events revealed that severe events tended to occur on the northern nose of the surface-based unstable sector, allowing for maximal access to the reduced instability, and formed in the presence of an enhanced near-surface low pressure system (Fig. 2.8; Sherburn et al. 2016). Further, stronger low-level convergence coupled with upper-level divergence, relating to marginally increased updraft strength, which is a function of CAPE, proved to be useful features to distinguish severe events from nulls, defined as severe warned areas with no valid severe reports (Sherburn et al. 2016).

Strong shear throughout the atmospheric column is, by definition, required for HSLC events, but further investigation reveals a strong relationship between shear and tornadic potential, outweighing that of CAPE and tornadic potential. Approximately one-third of the tornadoes studied by Guyer and Dean (2010) formed with CAPE ≤ 500 J/kg, with a dataset spanning half a decade. Most of these tornadoes were in regions with forecasted values of the significant tornado parameter (STP) < 1.0, the common threshold for anticipation of tornado formation (Thompson et al. 2003; Thompson et al. 2004). The distinction between the strong or violent (EF2+) and general tornadic (EF0-EF1) environment is most pronounced for occurrences within regions with MLCAPE < 1000 J/kg, with only 4% of significant tornadoes occurring in regimes with 0-1 km shear < 10 kt (Schneider et al. 2006). Due to the shallow nature of HSLC vortices, concentration of shear in the layers closest to the surface are most conducive to tornadogenesis (Sherburn and Parker 2019), as is corroborated by King et al. (2017), which

found that the highest mean 3-hour 0-1 km shear in non-severe HSLC events is weaker than the median 0-1 km shear in severe HSLC events.

Several other environmental quantities have been found to have skill in discriminating between severe and non-severe HSLC events, though meaningful changes in these may occur rapidly before tornadogenesis, thus making them difficult to forecast. Near-surface lapse rates are an important prognostic tool, as steepness of low-level lapse rates often serve to locally boost instability. Lapse rates in the 0-3 km layer were found to be the most skillful way to distinguish between the two, most notably in the southeast and mid-Atlantic US where HSLC events are most prevalent and decreasing either 0-1 km shear or 0-3 km lapse rates limited the potential for severe weather in HSLC environments (Sherburn and Parker 2014, 2019). Through analysis and statistical testing of combinations of the environmental quantities revealed to be useful in discriminating between severe and non-severe HSLC convection, the 0-3 km lapse rate was determined to be especially skillful (Sherburn and Parker 2014).

Despite being characteristically low in HSLC events, CAPE and its evolution plays an important role in discriminating between severe and non-severe events. Through numerical simulations of convection within HSLC environments, King et al. (2017) found that non-severe events had lower maximum values of SBCAPE than their severe counterparts, and experienced surface cooling that further stabilized the near-storm environment (Sherburn et al. 2016). Conversely, locally buffed values of SBCAPE result from steepening low-level lapse rates due to increases in near-surface temperatures prior to convective development (Sherburn et al. 2016; King et al. 2017). However, significant differences in low-level instability arise on the sub-3-hour timescale, one that is too fine for both meaningful mesoscale numerical model output and storm-scale observations (King et al. 2017; Fig 2.9b).

HSLC nulls peak in the cool season and overnight, times when situational awareness is lower in operational forecasting of severe weather (Sherburn and Parker 2014). In an effort to mitigate this decreased forecasting skill in HSLC events (Dean and Schneider 2008), in part due to CAPE dependency of historical composite metrics used to forecast tornadic potential, efforts have been made to develop parameters to aid in forecasting of environments with reduced buoyancy (Sherburn and Parker 2014). SHERB, severe hazards in environments with reduced buoyancy, and its suite of modified versions (SHERBE, SHERBS3), were developed with operational forecasters in mind to forecast and diagnose the likelihood of severe HSLC events (Sherburn and Parker 2014). Each of the above parameters consist of the two most conditionally skillful quantities in discriminating between severe and non-severe HSLC events: LLLR, or 0-3 km lapse rate, and LR75, the 700-500 hPa lapse rate. The final component was less well-defined due to sample size issues with the test statistic from the initial investigation, and so several still-skillful quantities remained. SHERBE (the effective shear variant) is calculated and normalized as follows:

$$SHERBE = \left(\frac{ESHR}{27\ \frac{m}{s}}\right) * \left(\frac{LLLR}{5.2\ \frac{K}{km}}\right) * \left(\frac{LR75}{5.6\ \frac{K}{km}}\right) \quad (1)$$

where ESHR is the effective bulk shear, measured over the lower half of the storm depth (Thompson et al. 2007). This variant was determined to be the most skillful discriminator between severe and non-severe HSLC events; however, its reliance on effective layer shear, which is by definition 0 m/s when MUCAPE = 0 J/kg, proved to be problematic for cases in the sample dataset which occurred in regimes of no diagnosed CAPE. As such, the most skillful fixed-layer variant, SHERBS3, was developed to use in times when MUCAPE approaches zero, rendering the effective layer calculation futile:

$$SHERBS3 = \left(\frac{S3MG}{26\ \frac{m}{s}}\right) * \left(\frac{LLLR}{5.2\ \frac{K}{km}}\right) * \left(\frac{LR75}{5.6\frac{K}{km}}\right) \quad (2)$$

where S3MG is the magnitude of the 0-3 km shear.

D. Gaps in Previous Research

The field of high-shear low-CAPE severe research has expanded greatly in the past decade, from in-depth modelling studies to the climatologies and case studies that broke ground on the subject. Something that has remained much the same is the necessity for operationally applicable forecasting tools to propel HSLC events out of the low probability of detection (POD), high false-alarm rate (FAR) portion of the forecasting matrix. Several studies have corroborated the rapid destabilization and evolution of HSLC environments (Sherburn et al. 2016; King et al. 2017), but the sources and predictability of this rapid environmental evolution remain open to further investigation (Sherburn et al. 2016). Perhaps most importantly, environmental evolution, both temporal and spatial, is known to influence storm evolution and subsequent severe weather production (e.g., Ziegler et al. 2010; Coffer and Parker 2015; Davenport and Parker 2015; Klees et. al 2016; Gropp and Davenport 2018; Ledbetter 2018; Davenport et al. 2019). Certain environmental parameters have been identified as especially skillful in discriminating between severe and non-severe HSLC convection (Sherburn and Parker 2014; King et al. 2017; Sherburn and Parker 2019), but more investigation into the sensitivities of HSLC convection and other environmental variables is necessary (Sherburn and Parker 2019).

III. Data and Methods

A spreadsheet of candidate events occurring within HSLC environments was collaboratively compiled by meteorologists at several NWS WFOs across the mid-Atlantic and Southeast U.S. This list consisted of 28 unique severe weather days between January 2014 and October 2018 and included nearly 340 tornado reports in its original form. This dataset was further constrained to better line up with literature's documentation of the regions with the most common occurrence of HSLC environments (Sherburn et al. 2016), focusing mainly on the southeast US. Further, only those events that appear in both the Storm Prediction Center (SPC)'s filtered reports within the Severe Weather Event Archive (SWEA) and the National Centers for Environmental Information (NCEI) Storm Events Database were retained to ensure data quality. Due to reliance on archived NEXRAD radar data, which has varying resolution depending on proximity of the tornado report to the nearest WSR-88D, as well as occasional down time resulting in lack of data availability, not all tornado reports were able to be matched definitively with a reflectivity signature. In total, 63 reports were removed for being too far removed from the southeast US, 22 were removed for poor data resolution, and 5 were removed for being tornado path continuations despite being included within filtered SPC reports. After these constraints and considerations, and accounting for strongly convectively contaminated data points, the finalized dataset contains 224 tornado reports (Fig. 3.1)

Using archived radar data from NCEI's Weather and Climate Toolkit, each tornado report was classified as being associated with one of eight radar signatures (either one previously defined in literature as being associated with HSLC tornadogenesis, as in Davis and Parker (2014), or one appended to the list of previously defined signatures due to frequent observation in the dataset): supercell, embedded supercell, bowing segment, forward inflow notch, rear

inflow notch, gust front cusp, broken-S, or mesovortex/line-end vortex (Fig. 3.2). Several tornado families, historically defined as collections of tornadoes spawned by the same supercell, or in this case several tornadoes produced by the same evolving reflectivity signature, were included within the dataset. Each tornado report from within a tornado family was counted, classified, and recorded as an individual. There is likely a nontrivial time lag between the recorded time of the tornado report and the actual start time, which adds an extra layer of subjectivity to the attribution of a report to a particular reflectivity signature. Once a primary signature associated with the time of the tornado report was identified, that signature was tracked to determine a time of genesis and dissipation, and a total duration. Additional information was collected for each tornado report from the SPC SWEA and NCEI Storm Events Database, including EF rating and time of day (UTC), for use in further statistical analysis.

Once each report was tracked and classified, the time and latitude and longitude coordinates associated with the tornado report were used to begin to compile a spatiotemporal database of environmental characteristics. Using the 0-h analyses of archived Rapid Refresh (RAP) model data (Benjamin et al. 2016) with 13 km resolution, along with the Sounding and Hodograph Analysis and Research Program in Python (SHARPpy) sounding generation package and MetPy's sounding plotter capabilities (Blumberg et al. 2017; May et al. 2020), soundings were generated representing the inflow environment at three storm-relative points: ~40 km (approximately 3 grid points) away from the tornado report (hereafter referred to as the "storm inflow" point), ~40 km to the north, and ~40 km to the south; and at two times relative to tornadogenesis: at the time of the tornado report and one hour before the tornado report (Fig. 3.3).

The construction of this grid, including the spacing between the tornado report and sounding points, is rooted in prior research analyzing proximity soundings near severe convection (Potvin et al. 2010; Parker 2014). These studies illustrated the variability present within convective environments, and thus the representativeness of a single environmental profile is dependent on its location relative to the storm; there is a need to be close, but not too close, identified as the "Goldilocks zone" of 30-70 km from the updraft (Potvin et al. 2010). Furthermore, this set of data points was collected to quantify both the spatial and temporal variability present in HSLC environments, with the north and south points designed to measure the variability present in non-tornadic portions of a reflectivity signature. Notably, spatial and temporal variability is potentially a driving factor in storm evolution and severe weather production (e.g., Ziegler et al. 2010; Coffer and Parker 2015; Davenport and Parker 2015; Klees et al. 2016; King et al. 2017; Gropp and Davenport 2018; Ledbetter 2018; Davenport et al. 2019). Because all reports in the dataset were post-2012, RAP analysis was available for each case, eliminating the induced source of uncertainty that switching between the RUC and RAP provides as a result of differing boundary layer schemes (Cohen et al. 2015). The RAP was chosen due to its spatial and temporal resolution, but its limitations, especially in regard to errors in calculation of instability, low-level shear, and storm-relative helicity are acknowledged (Thompson et al. 2003; Thompson et al. 2007; Coniglio 2012).

Generated soundings were compared to the closest, in both location and time, observed sounding to determine representativeness. Usage of model data to generate soundings comes with the potential for convective contamination, especially in cases where the feature of interest is accompanied by trailing or leading convection. Soundings were considered to be convectively contaminated if layers became saturated, or very nearly moist-adiabatic, abruptly between one of

the hour time steps (T-1 hr or T=0 hr), often accompanied by a pronounced backing of near-surface winds and thus a strongly curved hodograph. Should a chosen environmental point produce a contaminated sounding, subsequent points were tested in the vicinity of the original point in an attempt to produce a more representative sounding. If no suitable model sounding analysis points are available, the case was thrown out. Four tornado reports, all collocated with regions of trailing or leading stratiform convection, were removed due to extensive convective contamination to arrive at the final count of 224 tornado reports.

After the complete set of representative environmental soundings was collected for all tornado reports within the dataset, composite soundings were generated for each reflectivity signature at all points within the constructed temporal and spatial grid (a total of six per signature). During the construction of the initial proximity environmental soundings for each tornado report, profile data — including height (m), pressure (hPa), temperature (C), dewpoint (C), lifted parcel temperature (C), the u and v-components of the wind vector, and wind speed (m/s) — was collected for all six environmental grid points. This profile data was interpolated to standardize by height (in 100 m intervals from the surface to 15 km) to ensure consistency between tornado reports from locations of varying elevation across the southeastern and mid-Atlantic US. Finally, these interpolated profile parameters were averaged to create a mean set of eight variables throughout the atmospheric column at all six environmental grid points per reflectivity signature. That averaged data was used in conjunction with the SHARPpy sounding package to arrive at complete composite soundings, including an inset composite hodograph.

Several environmental quantities and parameters previously identified as relevant to distinguishing between severe vs. non-severe nature of high-shear low-CAPE environments were then recorded for each of the six generated model soundings per tornado report: surface based

CAPE and CIN (SBCAPE, SBCIN), most-unstable CAPE and CIN (MUCAPE, MUCIN), mixed-layer CAPE and CIN (MLCAPE, MLCIN), 0-1 km shear, 0-3 km shear, 0-6 km shear, 0-1 km storm relative helicity (SRH), 0-3 km SRH, effective layer shear, effective layer SRH, and SHERBE (Thompson et al. 2003; Schneider et al. 2006; Thompson et al. 2007; Sherburn and Parker 2014; King et al. 2017; Sherburn and Parker 2019). Effective layer parameters improve upon other environmental quantities, such as shear or SRH, that are typically calculated from the surface regardless of the presence of capping inversions that may prevent surface-based convection, allowing for customization of the calculation based on the local environment and storm tops (Thompson et al. 2004; Thompson et al. 2007). These parameters utilize an effective base layer, defined as the first parcel that obtains CAPE > 100 J/kg and CIN > -250 J/kg when lifted. From there, effective layer shear is calculated up to 50% of the equilibrium level of the most unstable near-surface (lowest 300 mb) parcel, and effective layer SRH is calculated up to the pressure level where the lifted parcel has CAPE < 100 J/kg or CIN < -250 J/kg.

IV. Results

A. Summary Statistics

High-shear low-CAPE severe events present most commonly during the cool season and in the evening to overnight hours, which introduces its own operational problems related to situational awareness. The difficulties inherent to the forecasting of severe HSLC events cannot be understated; for example, 20/25 (80%) of the severe weather event days within the studied dataset fell within a marginal or slight risk for severe weather, per the SPC outlook forecast. Viewing the dataset broken down month-by-month reveals January to be the most active month for HSLC tornadoes (Table 4.1), with 97/224 (or ~43%) of all tornado reports. Further, 3 of the 6 severe weather days with the most signature diversity occurred within the month of January (Table 4.2). A secondary peak, valid across all reflectivity signatures, pops up in October, which featured 23 of the remaining 127 (or ~18%) tornado reports that occurred outside of January (Table 4.1). There does not seem to be a correlation between signature type and month of the year, apart from the most active months showing the most variety in observed reflectivity signatures (Tables 4.1-4.2).

Of the 224 HSLC tornado reports included in the dataset, the most numerous associated reflectivity signatures were the supercell and the bowing segment, accounting for 57% of the included cases (Table 4.3). Approximately 85% (178/209) of tornado reports were rated EF0 or EF1 (Table 4.4; Fig. 4.1); note that 14 of the included tornado reports did not have ratings listed in either the SWEA or NCEI Storm Events Database (labeled “EFU”). Significant tornadoes (rated EF2 or higher) make up 15% of the dataset (Table 4.4; Fig. 4.1). Perhaps unsurprisingly, supercells and embedded supercells are responsible for 23/34 (~68%) of the significant tornadoes, though a variety of other reflectivity signatures were associated with EF2 tornadoes

(Table 4.4; Fig. 4.1); this finding is consistent with prior work such as Anderson-Frey et al. (2016). Further consistency with other HSLC studies arises from the diurnal trends of HSLC tornadoes; in this study, these, specifically bowing segment, rear inflow notch, and supercellular tornadoes, have an earlier diurnal peak and persist well into the evening, particularly between 1700 and 0000 UTC, which matches up well with what the literature suggests (Fig. 4.2; Guyer and Dean 2010; Sherburn and Parker 2014; Sherburn et al. 2016). All other included signatures have secondary peaks, either earlier (~0500-1200 UTC; broken S, embedded supercell, gust front cusp, line end mesovortex), or later (~2200-2300 UTC; forward inflow notch), that are not seen in the aggregated dataset.

B. Synoptic Patterns

In an effort to discern the large-scale features that contributed to each HSLC severe weather event day, pseudo-composite synoptic maps (in the style of Fig. 2.8 from Sherburn and Parker 2016) were constructed for subjectively identified "bins" of synoptic patterns using RAP-13 km analysis data and archived WPC surface analyses from the time closest to the peak in severe activity. Four distinct synoptic set-ups were identified from the group of 25 unique severe weather days. Eleven (44%) of the severe weather days resemble the synoptic pattern seen in Fig. 2.8, with a broad surface cyclone placed in the Ohio River valley, a strong, southern-displaced jet streak, and a slightly digging mid-level trough in the Mid-West. This set-up maximizes the interplay between upper-level divergence and the warm sector, as discussed in Sherburn and Parker (2016). The most common reflectivity signature associated with produced HSLC tornadoes from this subset of the included dataset was the supercell, and the average tornado report location was in west-central Georgia. A similar but northern-displaced version of

this setup accounted for 7 (28%) HSLC event cases in the present dataset (Fig. 4.3). In addition to the surface cyclone being displaced to the northeast, this pattern is characterized by a sweeping cold front that extends across much of the eastern CONUS. As a result, this scenario is more frontally-forced compared to other events. Notably, the cold frontal passage may lead to increased lift and curved hodographs from the associated backing of winds aloft. The approximate centroid of tornado report locations within the studied dataset for this synoptic environment was northeast Georgia and featured a majority of produced tornadoes attributed to bowing segments (Fig. 4.3). A small percentage (12%, or 3/25) of the included severe weather days showed a synoptic pattern dominated by large-scale confluent flow oriented towards the northeast (Fig. 4.4). Much like the pattern identified in Fig 2.8, the positioning of the southern-most jet streak allows for a favorable overlap of mid-to-upper-level divergence and the increased moisture that characterizes the warm sector of a surface cyclone. This setup's average tornado report location was east-central Alabama and the most common associated reflectivity signature was the supercell (Fig. 4.4). The least-common synoptic pattern seen in the dataset accounted for 8% (2/25) severe weather days (Fig. 4.5) and features a prominent mid-level trough centered over the western portion of the US, along with a surface cyclone positioned over the Ark-La-Tex region. This specific synoptic pattern's average tornado report location was southeastern Georgia, and the most frequently tornadic signature was the forward inflow notch (Fig. 4.5).

As far as the relationship between each identified synoptic set-up category and their respective production of severe weather, the frequency of each synoptic pattern in the dataset is directly related to their relative potency. The composite synoptic environment described in Fig. 2.8 from Sherburn and Parker (2016) was responsible for approximately 71% (157/224) of the tornado reports in the dataset (Table 4.2). Coincidentally, this type of synoptic environment also

presented most frequently (accounting for 44% of the included severe weather days; Table 4.2). The next most common synoptic pattern, as in Fig. 4.3, contributed to 23.2% (52/224) of included HSLC tornado reports (Table 4.2). The two least common synoptic setups, in the style of Figs. 4.4 and 4.5, produced 4.5% (10/224) and 2.2% (5/224) of all HSLC tornado reports in the dataset.

C. Signature-specific Statistics

When binning by reflectivity signature, there are some small differences that can be seen in diurnal timing, duration of each signature type, and the intensity of any produced tornadoes. Of the eight reflectivity signatures investigated in this study, only three are not associated with at least 1 significant (EF2+) tornado, and each of these are primarily associated with quasi-linear-type convective systems (QLCSs): broken-S, forward inflow notch, and gust front cusp (Table 4.4; Fig. 4.1). A large (85%, or 178/224) proportion of the tornadoes within the dataset were considered "weak," and classified as either EF0 or EF1 (Table 4.4; Fig. 4.1). Further, for all reflectivity signature groups identified within the dataset, weak tornadoes constituted between 68 and 100% of the tornadoes attributed to each reflectivity grouping (Table 4.4; Fig. 4.1). QLCSs are often associated with more marginal tornado reports (e.g., Trapp et al. 2005; Smith et al. 2012; Marion and Trapp 2021), as is corroborated by Cope (2004)'s investigation into tornado reports associated with a line of storms in New England, finding that these reports were associated with notches and weak bowing that would "normally not justify a warning." Supercells and embedded supercells, the most discrete or nearly discrete signatures included within the dataset, showed relatively higher production of significant tornadoes when compared to the rest of the dataset, at 24% (20/82) and 25% (3/12), respectively.

An early evening peak (1800-2200 UTC) is seen in the diurnal pattern of the case dataset as a whole (Fig. 4.2). The diurnal pattern of bowing segment, rear inflow notch, and supercell occurrence matches up well with the pattern of the aggregation of all reports (Fig. 4.2a, g, h), and is likely attributed to their overall dominance in the dataset, contributing to approximately 70% of the total tornado reports (Table 4.3). Broken-S, embedded supercell, and gust front cusp-associated HSLC tornadoes have an earlier, secondary peak (~1000-1200 UTC) that is not matched in the diurnal distribution of all tornado reports in the dataset (Fig. 4.2b, c, e). The gust front cusp subset appears equally most frequently between 1200 and 1500 and 2000 and 0000 UTC, which is offset from the overall dataset (Fig. 4.2e). Forward inflow notch and line end mesovortex-associated tornadoes have primary peaks that are several hours later, ~2200-2300 UTC, and several hours earlier, ~0500-1600 UTC, than that of the combination of all reports, respectively (Fig. 4.2d, f). These signatures, especially so for the line-end mesovortex and broken S, are characteristic of mature linear convection. The late evening and early morning peaks for QLCS-type tornadoes may be due in part to the influence of upscale growth on the development and maintenance of mesoscale convective systems (MCSs) and QLCSs, a process which is directly influenced by the nocturnal low-level jet (LLJ; e.g., Weisman 1993; Corfidi 2003; Coniglio et al. 2007; French and Parker 2010).

The duration of reflectivity signatures associated with HSLC tornado reports is crucial to operational forecasting, as current guidance for these events is based on pattern recognition of radar data due to failure of traditional forecasting methods as a result of environment composition and evolution. Bowing segment signatures persist typically on the order of 30-90 minutes, with isolated reports up to 240 minutes (4 hours; Fig. 4.6a). Similarly, the duration of supercells has the largest range between the largest cluster and the outliers, with a majority of

reports persisting for approximately 90 minutes, but about 5% lasting upwards of nearly 6 hours (Fig. 4.6h). These reflectivity signatures are more pronounced and widely recognized than the more transient non-supercellular signatures, and when combined with durations that commonly exceed 90 minutes, forecasters are provided sufficient insight into lifetime tornadic potential. In terms of duration, the distribution of gust front cusps and forward inflow notches are very similar, with a majority lasting approximately half an hour, and all lasting 65 minutes or less (Fig. 4.6d, e). Broken-S duration consists of two defined bins: sub-half hour (10-30 min) and greater-than-one-hour (60-80 min), with no reports falling between (Fig. 4.6b). Forward inflow notches were one of the most transient reflectivity signatures, with approximately one-third of cases lasting under 15 minutes, and all reports dissipating within an hour (Fig. 4.6d). On the other hand, rear inflow notch durations are very nearly Gaussian, with most reports clustered around 30 minutes, and tails at 15 minute and one-hour duration (Fig. 4.6g). When a nontrivial percentage of lifetimes of a tornadic reflectivity signature fall below 30 minutes, and when considering that many of these signatures are subtle as best even in regions with fine resolution radar data, the existence of HSLC severe events within the high-FAR/low-POD portion of the forecasting matrix becomes more understandable (Dean and Schneider 2008; Schneider and Dean 2008; Davis and Parker 2014).

D. Composite Soundings

In an effort to illustrate and quantify the storm-scale environmental changes that occur in the hour preceding tornadogenesis for HSLC cases, composite soundings were developed for each of the eight identified reflectivity signatures that commonly precede HSLC tornadic activity (e.g., bowing segment, broken-S, embedded supercell, forward inflow notch, gust front cusp, line-end

mesovortex, rear inflow notch, and supercell; cf. Fig. 3.2). Spatially and temporally, the identified environmental differences both within, and even across signatures, are fairly subtle, which underscores the challenge forecasters face with HSLC convection. Across all signatures and both analysis times, the northern environmental point (as in Fig. 3.3) appears to correspond to the weakest values of CAPE (Figs. 4.7a,d-4.14a,d). Conversely, again across all signatures, the southern environmental point was the profile with the most instability, despite not being the location where tornadogenesis occurred (Fig. 4.7c,f-4.14c,f). What appears to set apart the tornadic inflow point from the southern point is the higher low-to-mid-level moisture (Fig. 4.7b,e-4.14b,e); this slightly enhanced dryness at the southern point may be sufficient to reduce the overall intensity of any convective updrafts via entrainment, potentially reducing the likelihood of tornadogenesis (e.g., James and Markowski 2010; Wade and Parker 2021).

The evolution of the pre-tornadic to tornadic environment in bowing segments trended towards slightly more low-to-mid-level curvature in the composite hodographs (Fig. 4.7). The northern and inflow environments show a decrease, on the order of 25-50 hPa, in the value of the EL, acting to further concentrate the modest values of CAPE (Fig. 4.7a,d;b,e). The set of broken-S environmental composite soundings show substantial near-surface moistening, from near dry-adiabatic to almost complete saturation across all three environmental points (Fig. 4.8). Like the bowing segment composite environments, the northern and inflow environments for broken-S HSLC tornadoes show decreases in EL height of a similar magnitude (Fig. 4.8a,d;b,e). Additionally, hodograph curvature appears to increase when moving north across the environment as a whole for broken-S cases, but with no real difference present temporally (Fig. 4.8). The tornadic profiles in the environments that produced embedded supercellular tornadoes show an increased capping inversion/increased CIN at all three analysis points (Fig. 4.9d-f). This

increase in CIN may have proved useful in priming the environment to support more nearly discrete convection, as is the case with embedded supercells. Additionally, minor mid-level drying occurred between the pre-tornadic and tornadic time frames at the inflow and southern environmental points (Fig. 4.9b,c;e,f). The inflow point showed a decrease in EL height of approximately 60 hPa leading to the tornado report time (Fig. 4.9b,e). Unlike the broken-S environments, a subtle temporal difference in low-to-mid level shear is present, with hodograph curvature improving in the hour preceding tornadogenesis (Fig. 4.9). Similar to the embedded supercell environments, a modest increase in CIN, that tapers off moving north to south, was measured in the hour preceding tornadogenesis for forward inflow notch cases (Fig. 4.10d-f). The northern and inflow environments show a decrease in EL height proportional to that of the bowing segment and broken-S cases (Fig. 4.10a,d;b,e). The parcel profile in the inflow environment of gust front cusp-produced tornadoes had a reduced region of positive buoyancy at the time of tornadogenesis versus before tornadogenesis (Fig. 4.11b,e). Slight decreases in EL occurred in the time before tornadogenesis at the inflow and southern analysis points in the environments conducive to line-end mesovortices, rear inflow notches, and supercells (Fig. 4.12-14b,e;c,f). Trivial hodograph changes are seen in the profiles for embedded supercells, gust front cusps, line end mesovortices, rear inflow notches, and supercells, with similar hodograph shapes observed spatially and temporally for each set of composites (Figs. 4.10-4.14).

E. Raw Environmental Parameter Statistics

At the time of tornadogenesis (T=0), generally similar trends are measured across identical environmental points for all types of CAPE (Figs. 4.15, 4.17, 4.19). Consistent with the composite soundings (Figs. 4.7-4.14), the southern environmental analysis point presents as the

most unstable (Figs. 4.15c, 4.17c, 4.19c), despite not being the location of tornadogenesis. Median values of instability tend to decrease moving north in the environments across all signature types (Figs. 4.15, 4.17, 4.19). This may, especially in the cases of the QLCS-type signatures, be a result of the environment being damped by large areal coverage of convection, or the typical poleward decrease in instability. Notably, across all 3 measured subtypes of CAPE and all environment analysis points, broken-S, supercellular, and embedded supercellular HSLC tornadoes tended to be associated with larger median values of instability as compared to the other included reflectivity signatures (Figs. 4.15, 4.17, 4.19). Supercells have the largest range of values of CAPE (Figs. 4.15, 4.17, 4.19), which is likely a consequence of the sample size being much larger, but also the discrete nature of these storms, allowing pockets of greater instability to develop within breaks in the clouds. Several reflectivity signatures have upper-end values of instability well above the typical thresholds for HSLC events – namely broken-S, gust front cusps, embedded supercells, bowing segments, and supercells – that suggests locally greatly enhanced values of CAPE that may occur on too fine a scale for even high-resolution models to pick up on (e.g., as in King et al. 2017).

Unlike the general pattern seen for instability, lower values of convective inhibition (for ML and MU parcels; Figs. 4.18, 4.20), are seen in the tornadic inflow environments, favoring the onset of convection. Values of SBCIN have a broad range but can be quite large across all signatures, and apart from the environments associated with broken-S' and line end mesovortices, may be too large to be overcome through frontal or layer lifting (Fig. 4.16). This suggests the presence of another mechanism to prime the atmosphere for convection, such as the release of potential instability as suggested by Sherburn et al. (2016).

Median surface temperatures for all reflectivity signatures are clustered between 15 and 20°C (Fig 4.21). This is, of course, directly related to the positioning of the dataset within the cool season months, characteristic of HSLC events (Table 4.1). As shown in the composite soundings (Figs. 4.7-4.14), the environments that contributed to tornadogenesis were quite moist, and the distributions of surface dewpoint are very similar to that of surface temperature (Fig. 4.22). Embedded supercells, forward inflow notches, and supercells show longer tails toward cooler dewpoints (Fig. 4.22), suggesting drier surface conditions. This is corroborated by the respective composite soundings (Figs. 4.9, 4.10, 4.14). Dewpoint depression, or the difference between surface temperature and dewpoint, shows several distinct groupings (Fig. 4.23). Forward inflow notches have the largest range in dewpoint depressions, but median values of approximately 2°C (Fig. 4.23). Embedded supercells have the largest median dewpoint depression, with values between 2 and 4°C, with the highest median values associated with the inflow environment (Fig 4.23b). Gust front cusps, line end mesovortices, rear inflow notches, bowing segments, and supercells show marginal dewpoint depressions, all between 1 and 2°C for all environmental points (Fig. 4.23). The broken-S appears to correspond to the most nearly saturated surface environment across the board, with median values between 0 and 1°C (Fig 4.23). This corresponds to a significant moistening occurring in the low levels before the onset of tornadogenesis, apparent in the composite soundings (Fig. 4.8).

Much like the trends seen for instability, 0-1 km shear appears to be have the largest median values at the southern environmental analysis for most signatures (Fig. 4.24). Median values of 15-20 m/s (29-39 kts) for low level (0-1 km) shear are found across all environmental points, and all reflectivity signatures (Fig. 4.24). For low to mid-level shear (0-1 and 0-3 km shear; Figs. 4.24, 4.26), tornadic environments associated with forward inflow notches have the largest range

in values. Median values of 0-1 km SRH are between 50 and 100 m^2/s^2 for all reflectivity signatures and environmental points, with a large proportion around 75 m^2/s^2 (Fig. 4.25). A generally accepted threshold of 100 m^2/s^2 0-1 km SRH (Thompson et al. 2003) exists for increased likelihood of supercellular tornadoes, but the supercells in this dataset have median 0-1 km SRH of ~75 m^2/s^2 (Fig. 4.25). As such, HSLC tornadoes may hinge on smaller-scale features (e.g., surface boundaries) to enhance helicity. 0-3 km SRH was characterized by slightly larger median values, 100-150 m^2/s^2 (Fig. 4.27). HSLC events are typically characterized by deep layer (0-6 km) shear ≥ 18 m/s (35 kts), and this lines up well with median values of 0-6 km shear in the dataset, across all environmental points (Fig. 4.28). The southern environment has the most favorable effective layer parameters at the time of tornadogenesis, SHERBE included (Figs. 4.29-4.31). The severe hazards in environments with reduced buoyancy (SHERB/SHERBE) parameter was developed to serve as a diagnostic parameter for HSLC events, with a threshold of 1.0 to discriminate between significant severe and non-severe HSLC environments (Sherburn and Parker 2014). Interestingly, none of the environmental analysis points or reflectivity signatures have median values of 1 for SHERBE, despite all of the events included within the dataset being considered severe -- that is, being associated with at least one severe report (winds of at least 58 mph [50 kts or ~93 km/h], hail at least 1” in diameter, or a tornado). SHERBE’s normalized effective layer shear component utilizes 27 m/s as a threshold, which is much larger than median values of effective layer shear across all environmental points (c.f. Fig. 4.29).

F. Changes in Calculated Environmental Parameters

To identify whether the temporal changes in the environments at each of the inflow points was impactful for tornadogenesis, raw “deltas” leading up to tornadogenesis (i.e., subtracting

values at T-1 from T=0) in all parameters were calculated. As illustrated by the calculated composite soundings (c.f., Figs. 4.7-4.14), modest median decreases in MUCAPE occurred for nearly all reflectivity signatures; ML and SB parcels also exhibited similar trends (not shown). This is apparent at all 3 environmental analysis points and both times, apart from the northern and inflow environments for gust front cusps and northern environment for broken-S', on the order of 10-20% (Fig. 4.32a,b). Conversely, MUCIN showed a general trend of positive median percent changes (~50-100% in magnitude; Fig. 4.33), meaning that CIN became more favorable for convective maintenance. A small proportion of tornado reports had no measurable CIN in the pre-tornadic environments, producing an undefined result when calculating percent change; these cases were masked from analysis to produce meaningful graphical representations. Additionally, percent changes were computed, calculated by dividing the delta by the reference value (T-1). The negative median percent changes for the northern embedded supercell environment and inflow forward inflow notch environment are depicted on their respective composite soundings as an increased capping inversion (Figs. 4.9a,d; 4.10b,e), while the broken-S changes are more subtle (Fig. 4.8b,e;c,f). SBCIN (and MLCIN, not shown) trended generally towards conditions more unfavorable for convective maintenance, with negative median percent changes, and some upwards of 175% (Fig. 4.34). This decrease in convective favorability is in contrast to Sherburn et al. (2016) and King et al. (2017), which found that rapid destabilization occurs preceding tornadogenesis in severe HSLC environments. This may be partially attributed to varying levels of low-to-mid-level drying measured across the composite soundings (Figs. 4.7-14). Additionally, the work of King et al. (2017) was internally consistent, with the location of soundings being chosen based upon the location of convection within each simulation, which is not the case with this observational study. Small, but non-trivial, negative median percent

changes in dewpoint depression are measured across a large proportion of the reflectivity signature bins (Fig. 4.35). This decrease in dewpoint depression corresponds to increasing moisture, likely related to the building in of the warm sector of surface cyclones responsible for most of the severe weather event days within the dataset. Low-level (0-1 km) and mid-level (0-3 km, not shown) wind shear and SRH, and deep-layer (0-6 km) bulk wind shear have generally positive trends in median percent change, though small in magnitude (Figs. 4.36-4.38). Changes in bulk shear typically result from synoptic scale influence, and in the case of HSLC, are likely due to encroachment of the surface/mid-level trough or frontal system that fed convective development. All effective layer parameters (effective layer shear and SRH, SHERBE) have sweeping negative trends across nearly all reflectivity signatures (Figs. 4.39-4.41). Decreases in EL height, some as low as 10 hPa and some upwards of 75 hPa, were measured preceding tornadogenesis in calculated composite soundings (Figs. 4.7-14). This would affect the calculation of the effective layer and may contribute to the decrease in derived parameters.

G. Statistical Analysis of Calculated Environmental Parameters

Several sets of 2-way Kolmogorov-Smirnov (KS) statistical tests were performed to determine which, if any, differences or changes in data were statistically significant. The KS test was chosen due to being nonparametric in nature, as many of the calculated environmental parameters showed some level of skewness. The first set of KS tests were performed to determine if there was a statistically significant difference between the pre-tornadic (T-1) and tornadic (T=0) environmental data at a single analysis point (e.g., was the pre-tornadic inflow environment statistically significantly different from the tornadic inflow environment?), in an attempt to understand the changes occurring *temporally* to lead to tornadogenesis. A handful of

environmental parameters had calculated statistically significant differences; most commonly (in 67% or 6/9 results), these differences were found at the northern environmental analysis point (Table 4.5). The effective layer parameters (effective layer shear and SRH, SHERBE) showed statistically significant temporal differences for rear inflow notches at the northern and inflow analysis point. Effective layer shear showed median decreases of around 5 m/s at the northern environment for rear inflow notches, which corresponds to a nearly 40% decrease (Fig. 4.39a). Effective layer SRH at the inflow and northern environments for rear inflow notches decreased similarly (~-30-40%), with median deltas of -25 to -50 m^2/s^2, respectively (Fig. 4.40a,b). SHERBE, an effective layer shear derivative, echoed trends seen for effective layer shear (~40% median decreases) at the northern rear inflow notch environment, with median deltas of -0.25 (Fig. 4.41a). Each of these can likely be attributed to a nearly 100 hPa decrease in EL preceding tornadogenesis in the northern environment (Table 4.5; Fig 4.13).

Also of interest are potential *spatial* differences that lead to one portion of the environment being favored over the other. Specifically, how do the northern and southern environments compare to the inflow environment at the time of tornadogenesis (T=0)? Thermodynamically, apart from SBCAPE at the northern environment analysis point for broken-S, all statistically significant differences were between the southern and inflow environments at the time of tornadogenesis (Table 4.6a). For all calculated composite soundings, the southern environment showed the most favorable instability (Figs. 4.7c,f-4.14c,f). This is shown further by small increases, on the order of 100-200 J/kg, in median values of all measured values of CAPE (for surface-based parcels, mixed-layer, and most-unstable; Figs. 4.15, 4.17, 4.19). Similarly, for surface parameters (aside from northern bowing segment surface temperature, and northern broken-S dewpoint depression, surface temperature and dewpoint), all statistically significant

differences occurred between the southern and inflow environments (Table 4.6b). The southern extent of the northern branch of the broken-S is commonly the portion that becomes tornadic (McAvoy et al. 2000; Lane and Moore 2006). Kinematically, the statistically significant differences are much the same, with 71% (5/7) of the significant results being favored for the southern environment (Table 4.7). Median values of 0-1 and 0-3 km shear are approximately 2-3 m/s higher in the southern environment for line end mesovortices and supercells than at the inflow point (Figs. 4.24b,c; 4.26b,c). Conversely, the inflow environment shows more favorable median values of low-level (0-1 km) SRH, by about 25 m^2/s^2, than the northern and southern environments for line end mesovortices and supercells, respectively (Fig. 4.25). The differences in 0-3 km SRH mimicked those of 0-1 km SRH, with the inflow environments of broken-S and supercells more favorable than the northern and southern environments (Fig. 4.27).

There are several hypotheses as to why the southern environment, though favorable, was not observed to be tornadic. The first is the presence of surface boundaries that may act to enhance tornadogenesis at the inflow point, which are not necessarily resolved in the RAP model analysis; it is possible that there was an outflow boundary or other feature at the inflow point that acted to enhance or instigate tornadogenesis (e.g., Markowski et al. 1998; Rasmussen et al. 2000; Magee and Davenport 2020). Model data, while increasingly more reliable with continued advances in resolution and internal physics, is only an estimation of the true atmospheric conditions at a location. These features, if present, may not have been accurately resolved by the RAP. Second, and not mutually exclusive, is the effect of subtly drier mid-levels, which could result in a larger reduction in instability via enhanced entrainment at the southern point (James and Markowski 2010), particularly for convective features with more narrow updrafts (e.g., McCaul and Cohen 2002; Peters et al. 2020). Lastly, a large contributor may be the relative lack

of forcing. Key differences between the composites of significant severe and non-severe environments shown by Sherburn and Parker (2016) include the positioning and strength of forcings for ascent (Fig. 2.8).

Finally, percent changes were computed to quantify how much the near storm environment was changing at each environmental analysis point (e.g., between the percent changes at the northern and southern environment in the hour preceding tornadogenesis). The statistical significance of these changes was investigated, with the results showing only a few thermodynamic parameters of statistical significance (Table 4.8). More than half (3/5) of the statistically significant differences were calculated for measures of convective inhibition (CIN) between the northern and inflow environments. The remaining statistically significant results (2/5) were for values of CAPE between the southern and inflow environments (Table 4.8). Notably, all of the statistically significant percent changes were thermodynamic in nature. The marginal true magnitudes (on the order of 5-15%, with deltas of only 5-10 m/s) of the kinematic changes were the likely contributor to their relative lack of significance (Figs. 4.36, 4.38).

The percent change observed in the northern embedded supercell environment was determined to be statistically significant from that of the inflow environment (Table 4.8). At T=0, the median values of MUCIN for both the northern and inflow environment of embedded supercellular tornadoes were between -2 and -5 J/kg (Fig. 4.20). Within the hour, the northern environment experienced a median percent change of approximately -20% (increasing MUCIN), while the inflow environment saw a +75% change (decreasing MUCIN, or increasing favorability for convective maintenance; Fig. 4.33a,b). This is likely due to a larger capping inversion developing in the northern environment compared to the inflow environment prior to the time of tornadogenesis (Fig. 4.9a,d;b,e). Much like the embedded supercell, the northern and

inflow environments of forward inflow notches experienced statistically significant percent changes in SBCIN and had similar median values of SBCIN (~-50 J/kg) at T=0 (Table 4.8, Fig. 4.16). Between T-1 and T=0, the northern environment underwent an approximately 15% increase in SBCIN (i.e., more positive, less negative SBCIN), while the inflow environment experienced a nearly -125% change (Figs. 4.34a,b). This, thermodynamically much like the case of embedded supercells, is due to the formation of a larger capping inversion at the inflow environment than the northern environment (Figs. 4.10a,d;b,e). The northern and inflow environments of bowing segments exhibited similar environmental (SBCIN, not shown) and profile changes to that of forward inflow notches, resulting in statistically significant differences (Table 4.8).

The two statistically significant differences between the southern and inflow environments were found for broken-S and bowing segments (Table 4.8). MLCAPE (not shown) features similar trends to MUCAPE percent change-wise (Fig. 4.23b,c). As a result, though statistically significant, these differences are likely not physically significant, because the median values for both broken-S and bowing segments at the southern and inflow environments are very similar and centered around 0 J/kg. Further, temporally, the changes in positive buoyancy are marginal at the respective environmental analysis points for both figures (Figs. 4.7-4.8b,e;d,f).

V. Summary and Future Work

HSLC environments are less studied and less understood than their higher instability counterparts, yet constitute large percentages of annual severe hours and contribute to large proportions of annual tornado reports (Schneider et al. 2006, Dean and Schneider 2008; Schneider and Dean 2008). Further, their primary region of occurrence, the southeast US, is uniquely vulnerable due to socioeconomic concerns and population density (Ashley 2007; Ashley and Strader 2016). Previous studies have identified the volatile nature of HSLC environments (i.e., Sherburn et al. 2016; King et al. 2017) and relative heterogeneity of convective structures (Davis and Parker 2014). To quantify the spatial and temporal changes that HSLC environments undergo to become conducive to tornado production, a large dataset of tornado reports from cool-season severe HSLC event days were investigated using RAP model analyses to identify spatial and temporal variations in the near-storm environments that could key on relevant trends to enhance tornadogenesis nowcasting.

In the present dataset, January was the most active month, with a secondary peak observed in October (Table 4.1). The majority of tornado reports occurred between 1700 and 0000 UTC, with any deviations occurring on a signature-by-signature basis and related to the mechanisms behind the formation of linear convection (Fig. 4.2). Of the eight identified reflectivity signatures commonly associated with HSLC events (c.f. Fig. 3.2), no discernible pattern was found in regard to preferential months of occurrence. Supercells and bowing segments were associated with the most numerous tornado reports (57% of the dataset; Table 4.3). Perhaps unsurprisingly, 85% of the tornadoes within the dataset were defined as weak (EF0/EF1; Table 4.4, Fig. 4.1), in line with 87.5 % (7/8) of the reflectivity signatures being

QLCS-type. Supercells and embedded supercells contributed to 68% (23) of the 34 significant tornadoes included in the study (Table 4.4, Fig. 4.1).

A variety of synoptic patterns were identified to contribute to HSLC events (Figs. 2.8, 4.3-4.5), but as a whole, all are strongly synoptically forced. A strong majority (75%, or 3/4) of the synoptic setups involved the influence of adjacent surface cyclones, while the remaining setup is strongly frontally forced (Figs. 2.8, Figs. 4.4-4.5; Fig. 4.3). The potency of each synoptic grouping was found to be directly related to its relative frequency within the dataset. The largest percentage of HSLC tornado reports (~63%) were associated with the average synoptic pattern described by Sherburn and Parker (2016, Fig. 2.8), which included a majority of tornado reports attributable to supercells and accounted for 44% of the severe weather days included in the dataset.

Composite soundings were developed to illustrate the spatial and temporal environmental changes occurring in the near-storm environment leading up to tornadogenesis (Figs. 4.7-4.14). On the whole, all identified variability was extremely subtle, particularly for composite kinematic profiles. This is likely due to lack of meaningful large-scale changes in location of the influencing surface features occurring on a sub-hourly scale. Generally, instability was found to increase moving southward for all reflectivity signatures (Figs. 4.7-4.14). Increased mid-level moisture appears to be what pushed the inflow environment ahead in terms of tornadogenic potential, despite comparatively more marginal instability than the southern environment point. The strongest observed signal was an increase in near-surface moisture observed in the case of the broken S, for all environmental points (Fig. 4.8), from nearly dry-adiabatic to nearly moist-adiabatic. Further, a non-trivial and sometimes significant (~100 hPa) decrease in EL height occurred prior to tornadogenesis in a handful of signatures (bowing segments, broken-S,

embedded supercells, forward inflow notches, and rear inflow notches), serving to concentrate weak instability to the lower levels (Figs. 4.7-4.11, 4.13).

CAPE, for mixed-layer, most-unstable, and surface-based parcels, decreased preceding tornadogenesis for nearly all reflectivity signatures (Fig. 4.32). Median values of MUCIN decreased, indicating increasing convective favorability, between T-1 and T=0, while SB and MLCIN (not shown) increased, indicating decreased convective favorability, respectively (Fig. 4.33, 4.34). This finding contradicts Sherburn and Parker (2016) and King et al. (2017), which found destabilization to occur ahead of tornadogenesis. Subtle surface moistening was also observed via decreasing trends for median dewpoint depression (Fig. 4.35). Marginal increases in median low, mid, and upper-level shear were measured, likely attributable to decreasing proximity to the surface features feeding the HSLC environment (Figs. 4.36-4.38). Consistent with the decreases in EL height found in the composite soundings (Figs. 4.7-4.14), sweeping negative trends were present across all three effective layer parameters (effective layer shear and SRH, SHERBE), for all reflectivity signatures (Figs. 4.39-4.41).

Three sets of KS tests were performed to determine which, if any, calculated trends were of statistical significance. A majority of the measured differences, temporal or spatial, were not statistically significant. The first set, used to determine if a statistically significant change occurred temporally at a single environmental point, was composed largely of effective layer parameters (Table 4.5). The composite soundings revealed a measurable decrease in EL height, especially so for the rear inflow notch, which would affect subsequent calculations of effective layer parameters (Figs. 4.7-4.14). Also of interest were the spatial differences between the northern and southern environments versus the inflow environment at the time of tornadogenesis (T=0; Tables 4.6a,b, 4.7). A large proportion of statistically significant comparisons occurred for

thermodynamic variables (24/31, or 77%), and nearly all of them were between the southern and inflow environments. This is corroborated by the composite soundings, of which the southern environment shows the most pronounced CAPE for all reflectivity signatures (Figs. 4.7-4.14). Despite this, the inflow environment's favorability was likely bolstered by undetected meso or microscale features (Markowski et al. 1998; Rasmussen et al. 2000; Magee and Davenport 2020) and slightly improved moisture profiles that would better combat entrainment (McCaul and Cohen 2002; James and Markowski 2010; Peters et al. 2020).

The final goal of statistical analysis was to quantify the near-storm environment changes at each analysis point, and to determine if significantly different changes occurred between pairs of analysis points (Table 4.8). This set of tests showed the least numerous statistically significant results, at just five in total. The three most impactful environmental changes occurred in reference to the different metrics of CIN (mixed-layer, most-unstable, and surface-based). Each of these likely stemmed from the development of subtle but increased capping inversions at the time of tornadogenesis at alternating environmental points (Figs. 4.8-4.10; Table 4.8). The MLCAPE-based statistical significance calculations are likely not physically significant, due to similar magnitudes of median MLCAPE, median percent change, and lack of strong signals on composite soundings.

This study aimed to identify operationally relevant distinctions within tornadogenic versus non-tornadogenic HSLC environments, both spatially and temporally. Perhaps unsurprisingly, as is also the case for radar signals of HSLC tornadogenesis, many of the observed environmental differences were very subtle. The most useful parameters for mesoanalysis as events unfold appear to be related to surface to mid-level moisture, as instability uniquely decreases preceding tornadogenesis for many cases within the dataset, and kinematic

variables show very marginal changes. While improving on a lack of detailed observational cases investigating such a wide variety of environmental changes, this study is but a stepping stone for the eventual research goals for HSLC environments. More work is needed to understand why the changes that occur are occurring, especially the more perplexing changes (i.e., decreasing instability or increasing SBCIN), and modelling studies may help to fill some of these gaps. The formational mechanisms behind many of the investigated reflectivity signatures (namely those of QLCS vortices) are still being investigated, and nascent research may improve understanding of the relationship between those mechanisms and the environmental changes necessary to produce them.

VI. References

Anderson-Frey, A. K., Y. P. Richardson, A. R. Dean, R. L. Thompson, and B. T. Smith, 2016: Investigation of Near-Storm Environments for Tornado Events and Warnings. *Wea. Forecasting*, **31**, 1771–1790, https://doi.org/10.1175/WAF-D-16-0046.1.

Apsley, M. L., K. J. Mulder, and D. M. Schultz, 2016: Reexamining the United Kingdom's Greatest Tornado Outbreak: Forecasting the Limited Extent of Tornadoes along a Cold Front. *Wea. Forecasting*, **31**, 853–875, https://doi.org/10.1175/WAF-D-15-0131.1.

Ashley, W. S. (2007). Spatial and Temporal Analysis of Tornado Fatalities in the United States: 1880–2005, *Wea. Forecasting*, **22**(6), 1214-1228, https://doi.org/10.1175/2007WAF2007004.1.

—— & S. M. Strader, (2016): Recipe for Disaster: How the Dynamic Ingredients of Risk and Exposure Are Changing the Tornado Disaster Landscape, *Bull. Amer. Meteor. Soc*., **97(5)**, 767-786, https://doi.org/10.1175/BAMS-D-15-00150.1.

Benjamin, S. G., and Coauthors, 2016: A North American Hourly Assimilation and Model Forecast Cycle: The Rapid Refresh. *Mon. Wea. Rev.*, **144**, 1669–1694, https://doi.org/10.1175/MWR-D-15-0242.1.

Blumberg, W. G., K. T. Halbert, T. A. Supinie, P. T. Marsh, R. L. Thompson, and J. A. Hart, 2017: SHARPpy: An Open-Source Sounding Analysis Toolkit for the Atmospheric Sciences. *Bull. Amer. Meteor. Soc.*, **98**, 1625–1636, https://doi.org/10.1175/BAMS-D-15-00309.1.

Brooks, H. E., C. A. Doswell III, and M. P. Kay, 2003: Climatological estimates of local daily tornado probability for the United States. *Wea. Forecasting*, **18**, 626–640, https://doi.org/10.1175/1520-0434(2003)018<0626:CEOLDT>2.0.CO;2.

Coffer, B. E., and M. D. Parker, 2015: Impacts of Increasing Low-Level Shear on Supercells during the Early Evening Transition. *Mon. Wea. Rev.*, **143**, 1945–1969, https://doi.org/10.1175/MWR-D-14-00328.1.

Cohen, A., M.Coniglio, S.Cavallo, and H.Brooks, 2015: A review of planetary boundary layer parameterization schemes and their sensitivity in simulating southeastern U.S. cold season severe weather environments. *Wea. Forecasting*, **30**, 591–612, https://doi.org/10.1175/WAF-D-14-00105.1.

Coniglio, M. C., H. E. Brooks, , S. J. Weiss, , and S. F. Corfidi, 2007: Forecasting the maintenance of quasi-linear mesoscale convective systems. *Wea. Forecasting*, **22**, 556–570, https://doi.org/10.1175/WAF1006.1

Cope, A. M., 2004: An Early Morning Mid-Atlantic Severe Weather Episode: Short-Lived Tornados in a High-Shear Low-Instability Environment. *22nd Conference on Severe Local Storms,* Seattle, WA, Amer. Meteor. Soc., P1.4., https://ams.confex.com/ams/11aram22sls/webprogram/Paper81834.html.

Corfidi, S. F., 2003: Cold pools and MCS propagation: Forecasting the motion of downwind-developing MCSs. *Wea. Forecasting*, **18,** 997–1017., https://doi.org/10.1175/1520-0434(2003)018<0997:CPAMPF>2.0.CO;2

Clark, M. L., 2009: The southern England tornadoes of 30 December 2006: Case study of a tornadic storm in a low CAPE, high shear environment. *J. Atmos. Res.,* **93**, 50-65, https://doi.org/10.1016/j.atmosres.2008.10.008.

Davenport, C. E., and M. D. Parker, 2015: Impact of Environmental Heterogeneity on the Dynamics of a Dissipating Supercell Thunderstorm. *Mon. Wea. Rev.*, **143**, 4244–4277, https://doi.org/10.1175/MWR-D-15-0072.1.

——, C.L. Ziegler, and M.I. Biggerstaff, 2019: Creating a More Realistic Idealized Supercell Thunderstorm Evolution via Incorporation of Base-State Environmental Variability, *Mon. Wea. Rev.*, **147**, 4177–4198, https://doi.org/10.1175/MWR-D-18-0447.1.

Davis, J. M., and M. D. Parker, 2014: Radar climatology of tornadic and non-tornadic vortices in high shear, low CAPE environments in the mid-Atlantic and southeastern U.S. *Wea. Forecasting*, **29**, 828-853, https://doi.org/10.1175/WAF-D-13-00127.1.

Dean, A. R., R. S. Schneider, 2008: Forecast challenges at the NWS Storm Prediction Center relating to the frequency of favorable severe storm environments. *24th Conf. on Severe Local Storms,* Savannah, GA, Amer. Meteor. Soc., P9A.2., https://ams.confex.com/ams/24SLS/techprogram/paper_141743.html.

Evans, M., 2010: an examination of low CAPE/high shear severe convective events in the Binghamton, New York county warning area. *Natl. Wea. Dig.*, **34**, 129–144.

French, A. J., and M. D. Parker, 2010: The response of simulated nocturnal convective systems to a developing low-level jet. *J. Atmos. Sci.*, **67**, 3384–3408, https://doi.org/10.1175/2010JAS3329.1

Gropp, M.E. and C.E. Davenport, 2018: The Impact of the Nocturnal Transition on the Lifetime and Evolution of Supercell Thunderstorms in the Great Plains. *Wea. Forecasting*, **33**, 1045–1061, https://doi.org/10.1175/WAF-D-17-0150.1.

Guyer, J. L., and A. R. Dean, 2010: Tornadoes within weak CAPE environments across the continental United States. Preprints, *25th Conf. on Severe Local Storms*, Denver, CO, Amer. Meteor. Soc., 1.5., https://ams.confex.com/ams/pdfpapers/175725.pdf.

James, R. P., and P. M. Markowski, 2010: A numerical investigation of the effects of dry air aloft on deep convection. *Mon. Wea. Rev.*, **138**, 140–161, doi:10.1175/2009MWR3018.1.

King, J. R., M. D. Parker, K. D. Sherburn, and G. M. Lackmann, 2017: Rapid evolution of cool season, low CAPE severe thunderstorm environments. *Wea. Forecasting*, **32**, 763-779, https://doi.org/10.1175/WAF-D-16-0141.1.

Klees, A. M., Y. P. Richardson, P. M. Markowski, C. Weiss, J. M. Wurman, and K. K. Kosiba, 2016: Comparison of the Tornadic and Nontornadic Supercells Intercepted by VORTEX2 on 10 June 2010. *Mon. Wea. Rev.*, **144**, 3201–3231, https://doi.org/10.1175/MWR-D-15-0345.1.

Magee, K. M., and C. E. Davenport, 2020: An observational analysis quantifying the distance of supercell-boundary interactions in the Great Plains. *J. Operational Meteor.,* **8** (2), 15-38, https://doi.org/10.15191/nwajom.2020.0802

Marion, G. R., and R. J. Trapp. "Controls of Quasi-Linear Convective System Tornado Intensity", *J. Atmos. Sci*, **78**, 4 (2021): 1189-1205, https://doi.org/10.1175/JAS-D-20-0164.1.

Markowski, P. M., Rasmussen E. N., and Straka J. M., 1998: The occurrence of tornadoes in supercells interacting with boundaries during VORTEX-95. *Wea. Forecasting*, **13,** 852–859, https://doi.org/10.1175/1520-0434(1998)013<0852:TOOTIS>2.0.CO;2

——, and J. M. Straka, 2000: Some observations of rotating updrafts in a low-buoyancy, highly sheared environment. *Mon. Wea. Rev.*, **128**, 449–461, https://doi.org/10.1175/1520-0493(2000)128,0449:SOORUI.2.0.CO;2.

May, R. M., Arms, S. C., Marsh, P., Bruning, E., Leeman, J. R., Goebbert, K., Thielen, J. E., and Bruick, Z., 2020: MetPy: A Python Package for Meteorological Data. Version 0.12.2, Unidata, Accessed 06 August 2020. [Available online at https://github.com/Unidata/MetPy.] https://doi.org/10.5065/D6WW7G29.

McCaul E. W. Jr., and Cohen C., 2002: The impact on simulated storm structure and intensity of variations in the mixed layer and moist layer depths. *Mon. Wea. Rev.*, **130**, 1722–1748, https://doi.org/10.1175/1520-0493(2002)130<1722:TIOSSS>2.0.CO;2

Lane, J. D., and P. D. Moore, 2006: Observations of a non-supercell tornadic thunderstorm from terminal Doppler weather radar. Preprints, *23rd Conf. on Severe Local Storms*, St. Louis, MO, Amer. Meteor. Soc., P4.5., https://ams.confex.com/ams/pdfpapers/115102.pdf.

Ledbetter, C., 2018: Analyzing Supercell Intensity Changes in a Heterogeneous Environment in the VORTEX2 Supercell Pair in Southeastern Colorado on 11 June 2009. Thesis, Department of Geography and Earth Sciences, University of North Carolina at Charlotte, 91pp., https://ninercommons.uncc.edu/islandora/object/etd%3A516.

Peters, J. M., C. J. Nowotarski, and G. L. Mullendore, 2020: Are supercells resistant to entrainment because of their rotation? *J. Atmos. Sci.*, **77**, 1475–1495, https://doi.org/10.1175/JAS-D-19-0316.1.

Rasmussen, E. N., Richardson S., Straka J. M., Markowski P. M., and Blanchard D. O., 2000: The association of significant tornadoes with a baroclinic boundary on 2 June 1995. *Mon. Wea. Rev.*, **128,** 174–191, https://doi.org/10.1175/1520-0493(2000)128<0174:TAOSTW>2.0.CO;2

Schneider, R. S., and A. R. Dean, 2008: A comprehensive 5-year severe storm environment climatology for the continental United States. Preprints, *24th Conf. on Severe Local Storms*, Savannah, GA, Amer. Meteor. Soc., 16A.4., https://ams.confex.com/ams/pdfpapers/141748.pdf.

Schneider, R. S., A. R. Dean, S. J. Weiss, and P. D. Bothwell, 2006: Analysis of estimated environments for 2004 and 2005 severe convective storm reports. *23rd Conf. on Severe*

Local Storms, St. Louis, MO, Amer. Meteor. Soc., 3.5, https://ams.confex.com/ams/23SLS/techprogram/paper_115246.htm.

Sherburn, K. D., and M. D. Parker, 2014: Climatology and ingredients of significant severe convection in high-shear, low-CAPE environments. *Wea. Forecasting*, **29**, 854–877, https://doi.org/10.1175/WAF-D-13-00041.1.

—— and ——, 2016: Insights from Composite Environments of High-Shear, Low-CAPE Severe Convection. Preprints, *28th Conf. on Severe Local Storms*, Portland, OR, Amer. Meteor. Soc., 63, https://ams.confex.com/ams/28SLS/webprogram/Paper300645.html

——, ——, 2019: The Development of Severe Vortices within Simulated High-Shear, Low-CAPE Convection. *Mon. Wea. Rev.*, **147**, 2189–2216, https://doi.org/10.1175/MWR-D-18-0246.1.

——, ——, J. R. King, and G. M. Lackmann, 2016: Composite environments of severe and nonsevere high-shear, low-CAPE convective events. *Wea. Forecasting*, **31**, 1899–1927, https://doi.org/10.1175/WAF-D-16-0086.1.

Thompson, R. L., R. Edwards, J. A. Hart, K. L. Elmore, and P. Markowski, 2003: Close proximity soundings within supercell environments obtained from the Rapid Update Cycle. *Wea. Forecasting*, **18**, 1243–1261, https://doi.org/10.1175/1520-0434(2003)018,1243:CPSWSE.2.0.CO;2.

——, ——, and C. M. Mead, 2004: An update to the supercell composite and significant tornado parameters. Preprints, *22nd Conf. on Severe Local Storms*, Hyannis, MA, Amer. Meteor. Soc., P8.1., https://ams.confex.com/ams/pdfpapers/82100.pdf.

——, C.Mead, and R.Edwards, 2007: Effective storm-relative helicity and bulk shear in supercell thunderstorm environments. *Wea. Forecasting*, **22**, 102–115, https://doi.org/10.1175/WAF969.1.

——, B. T. Smith, J. S. Grams, A. R. Dean, and C. Broyles, 2012: Convective modes for significant severe thunderstorms in the contiguous United States. Part II: Supercell and QLCS tornado environments. Wea. Forecasting, 27, 1136–1154, https://doi.org/10.1175/WAF-D-11-00116.1.

Trapp, R. J., S. A. Tessendorf, E. S. Godfrey, and H. E. Brooks, 2005: Tornadoes from squall lines and bow echoes. Part I: Climatological distribution. *Wea. Forecasting*, **20**, 23–34, https://doi.org/10.1175/WAF-835.1.

Wade, A. R., & M. D. Parker, 2021: Dynamics of Simulated High-Shear Low-CAPE Supercells. *J. Atmos. Sci*., https://doi.org/10.1175/JAS-D-20-0117.1.

Weisman, M. L., 1993: The genesis of severe, long-lived bow echoes. *J. Atmos. Sci.*, **50**, 645–670, https://doi.org/10.1175/1520-0469(1993)050<0645:TGOSLL>2.0.CO;2

Ziegler, C. L., E. R.Mansell, J. M.Straka, D. R.MacGorman, and D. W.Burgess, 2010: The impact of spatial variations of low-level stability on the lifecycle of a simulated supercell storm. *Mon. Wea. Rev.*, **138**, 1738–1766, https://doi.org/10.1175/2009MWR3010.1

TABLES

Reflectivity Signature	Total	Count by Month											
		J	**F**	**M**	**A**	**M**	**J**	**J**	**A**	**S**	**O**	**N**	**D**
Bowing Segment	46	17	3	2	3	6	0	0	0	0	9	4	2
Broken S	14	10	0	0	0	3	0	0	0	0	0	1	0
Embedded Supercell	15	8	0	0	2	4	0	0	0	0	0	1	0
Forward Inflow Notch	11	1	1	1	4	0	0	0	0	0	2	2	0
Gust Front Cusp	14	9	4	1	0	0	0	0	0	0	0	0	0
Line End Mesovortex	14	8	0	0	0	0	0	0	0	0	6	0	0
Rear Inflow Notch	28	9	8	1	3	1	0	0	0	0	5	0	1
Supercell	82	35	20	0	11	11	0	0	0	0	1	3	1

Table 4.1: Breakdown of reflectivity signature count by month. Cool season months highlighted in blue.

Date	Total	Signature							
		Bowing Segment	Broken S	Embedded Supercell	Forward Inflow Notch	Gust Front Cusp	Line End Mesovortex	Rear Inflow Notch	Supercell
01/11/2014	4	1	0	0	0	3	0	0	0
02/21/2014	6	2	0	0	0	1	0	3	0
10/07/2014	10	4	0	0	1	0	0	5	0
10/14/2014	3	1	0	0	1	0	1	0	0
11/17/2014	2	1	1	0	0	0	0	0	0
11/23/2014	4	0	0	1	2	0	0	0	1
12/24/2014	3	2	0	0	0	0	0	0	1
01/03/2015	14	1	0	0	1	1	0	2	9
01/04/2015	7	0	0	0	0	1	5	1	0
11/18/2015	5	3	0	0	0	0	0	0	2
02/15/2016	24	0	0	0	0	2	0	3	19
03/01/2016	4	2	0	0	1	0	0	1	0
03/24/2016	1	0	0	0	0	1	0	0	0
04/06/2016	13	3	0	0	1	0	0	2	7
05/17/2016	1	0	0	0	0	0	0	1	0
01/21/2017	56	15	10	4	0	4	3	6	14
01/22/2017	16	0	0	4	0	0	0	0	12
02/25/2017	1	0	0	0	0	0	0	0	1
05/04/2017	20	5	3	4	0	0	0	0	8
05/05/2017	4	1	0	0	0	0	0	0	3
10/23/2017	10	4	0	0	0	0	5	0	1
12/20/2017	1	0	0	0	0	0	0	1	0
02/17/2018	5	1	0	0	1	1	0	2	0
04/03/2018	6	0	0	2	3	0	0	1	0
04/22/2018	4	0	0	0	0	0	0	0	4

Table 4.2: Breakdown of reflectivity signature count by severe weather day. Severe weather days defined as 12Z-12Z per SPC standards. Highlights correspond to grouped synoptic setups: yellow, as in Fig. 2.8; green, as in Fig. 4.3; magenta, as in Fig. 4.4; and cyan, as in Fig. 4.5.

Reflectivity Signature	Count	Frequency
Supercell	82	36.6%
Bowing segment	46	20.5%
Rear inflow notch	28	12.5%
Embedded supercell	15	6.7%
Gust front cusp	14	6.25%
Line end mesovortex	14	6.25%
Broken S	14	6.25%
Forward inflow notch	11	4.9%

Table 4.3: Detailed breakdown of reflectivity signature count and frequency (%) within the dataset.

Signature	EF Rating			
	U	0	1	2
Bowing Segment	5	17	19	5
Broken S	0	5	9	0
Embedded Supercell	0	5	7	3
Forward Inflow Notch	1	4	6	0
Gust Front Cusp	0	9	5	0
Line End Mesovortex	1	4	8	1
Rear Inflow Notch	1	7	17	3
Supercell	6	25	31	20

Table 4.4: EF rating of HSLC tornado reports within the dataset aggregated by reflectivity signature.

Reflectivity Signature	Environmental Location	2-Sided KS Test	
		Value	P-value
MUCAPE			
Line End Mesovortex	South	0.64286	0.00490
Supercell	North	0.23171	0.02418
SBCAPE			
Supercell	North	0.24390	0.01494
Surface T (C)			
Embedded Supercell	Inflow	0.53333	0.02625
0-3 km SRH			
Bowing Segment	North	0.30435	0.02765
Effective Layer Shear			
Rear Inflow Notch	North	0.46429	0.00425
Effective Layer SRH			
Rear Inflow Notch	North	0.46429	0.00425
	Inflow	0.39286	0.02562
SHERBE			
Rear Inflow Notch	North	0.39286	0.02562

Table 4.5: Results of 2-sided Kolmogorov-Smirnov statistic tests performed to compare the raw pre-tornadic (T-1) and tornadic (T=0) environmental data at a single sounding analysis point. Included are differences statistically significant at the alpha (α) = 0.05 level.

Reflectivity Signature	Environmental Location	2-Sided KS Test	
		Value	P-value
MUCAPE			
Bowing Segment	South	0.30435	0.02766
Broken S	South	0.57143	0.01878
Embedded Supercell	South	0.53333	0.02625
Mesovortex	South	0.71429	0.00102
Rear Inflow Notch	South	0.46429	0.00425
Supercell	South	0.21951	0.03816
SBCAPE			
Bowing Segment	North	0.32609	0.01451
	South	0.32609	0.01451
Broken S	South	0.57143	0.01878
Mesovortex	South	0.57413	0.01878
Rear Inflow Notch	South	0.42857	0.01089
Supercell	South	0.25610	0.00899
MLCAPE			
Bowing Segment	South	0.32609	0.01451
Embedded Supercell	South	0.53333	0.02625

Table 4.6a: Results of 2-sided Kolmogorov-Smirnov statistic tests performed to compare raw tornadic (T=0) thermodynamic environmental data at the northern and southern sounding analysis points to the inflow point. Included are differences statistically significant at the alpha (α) = 0.05 level.

Reflectivity Signature	Environmental Location	2-Sided KS Test	
		Value	P-value
Surface T (C)			
Bowing Segment	North	0.30435	0.02766
	South	0.34783	0.00725
Broken S	North	0.57143	0.01878
Embedded Supercell	South	0.6	0.00766
Mesovortex	South	0.57143	0.01878
Rear Inflow Notch	South	0.39286	0.02562
Supercell	South	0.28049	0.00301
Surface Td (C)			
Broken S	South	0.57143	0.01878
Mesovortex	South	0.71423	0.00102
Dewpoint Depression			
Broken S	North	0.64286	0.00490

Table 4.6b: Results of 2-sided Kolmogorov-Smirnov statistic tests performed to compare raw tornadic (T=0) thermodynamic environmental data at the northern and southern sounding analysis points to the inflow point. Included are differences statistically significant at the alpha (α) = 0.05 level.

Reflectivity Signature	Environmental Location	2-Sided KS Test	
		Value	P-value
0-1 km Shear			
Mesovortex	South	0.57143	0.01878
Supercell	South	0.28049	0.00301
0-3 km Shear			
Supercell	South	0.23171	0.02418
0-1 km SRH			
Mesovortex	North	0.57143	0.01878
Supercell	South	0.26829	0.00527
0-3 km SRH			
Broken S	North	0.57143	0.01878
Supercell	South	0.24390	0.01494

Table 4.7: Results of 2-sided Kolmogorov-Smirnov statistic tests performed to compare raw tornadic (T=0) kinematic environmental data at the northern and southern sounding analysis points to the inflow point. Included are differences statistically significant at the alpha (α) = 0.05 level.

Reflectivity Signature	Environmental Location	2-Sided KS Test	
		Value	P-value
MUCIN			
Embedded Supercell	North	0.60317	0.02136
SBCIN			
Forward Inflow Notch	North	0.60227	0.04681
MLCAPE			
Bowing Segment	South	0.27826	0.04130
Broken S	South	0.27826	0.04130
MLCIN			
Bowing Segment	North	0.35598	0.02779

Table 4.8: Results of 2-sided Kolmogorov-Smirnov statistic tests performed to compare percent change of environmental data in the hour preceding to tornadogenesis at the northern and southern sounding analysis points to the inflow point. Included are differences statistically significant at the alpha (α) = 0.05 level.

FIGURES

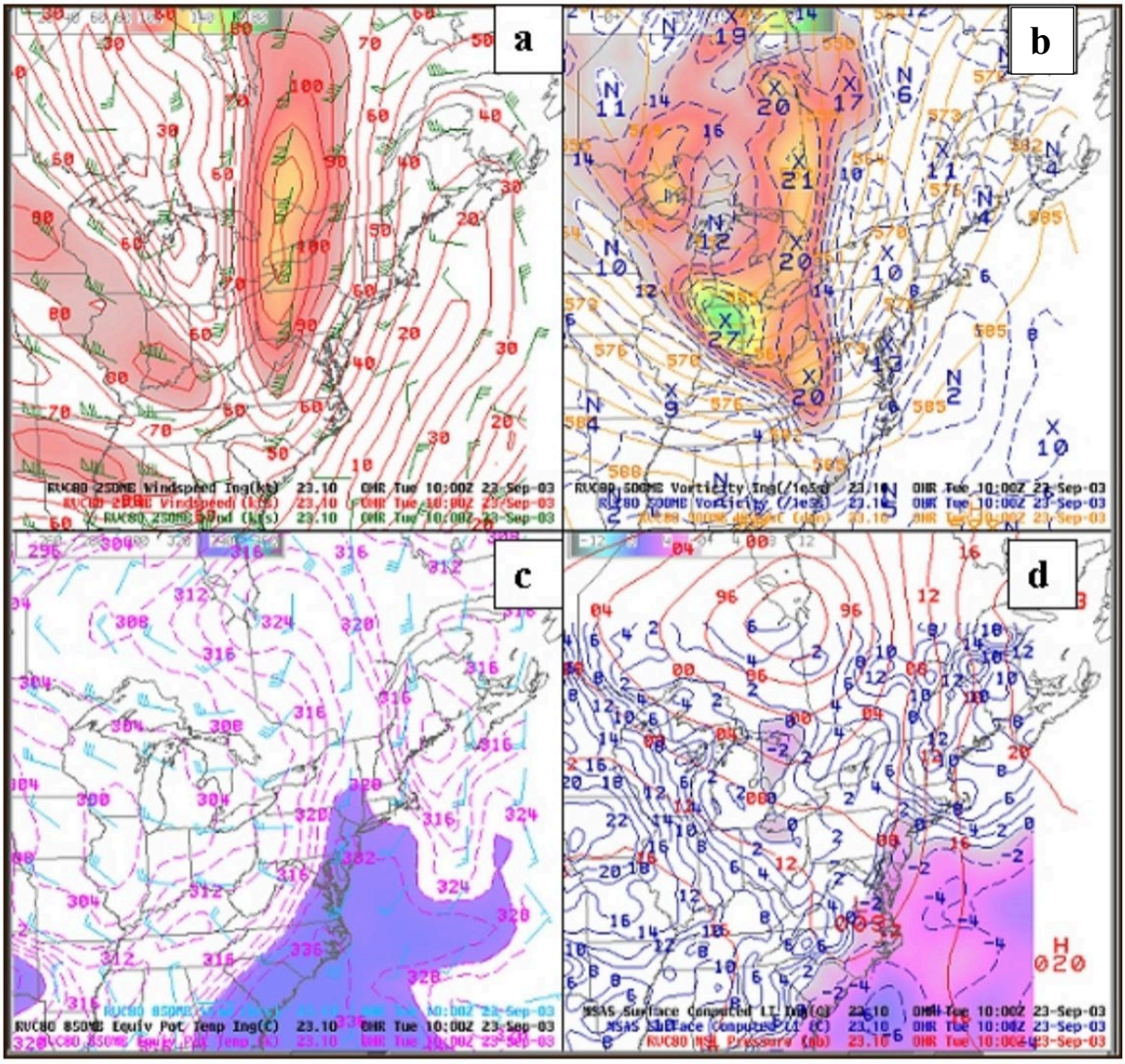

Figure 2.1, Model analyses illustrating a digging mid-level trough at 500 hPa with its axis roughly over the study area (upper right panel). Reproduced from Cope (2004).

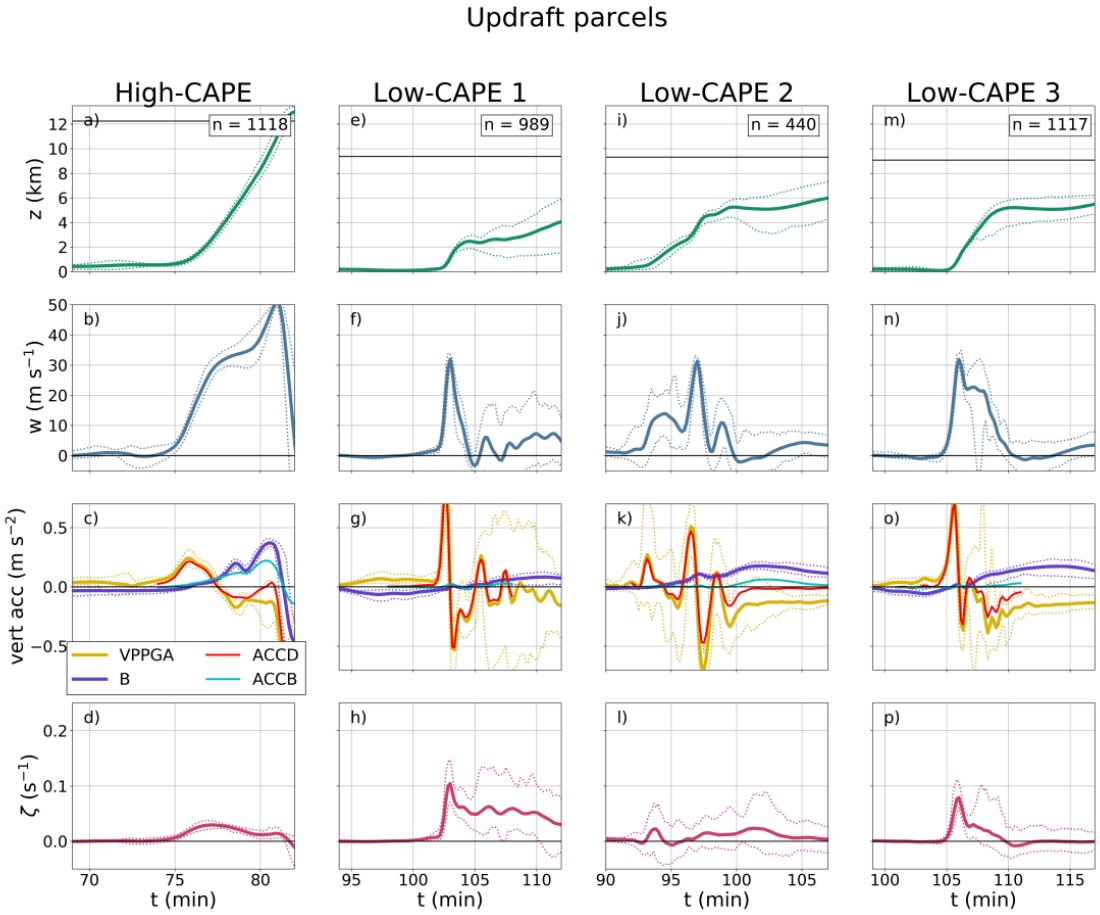

Figure 2.2, Time series of various simulated parcel quantities, including dynamic acceleration (ACCD; red), buoyancy (B; purple), buoyant accelerations (ACCB; cyan), and total vertical perturbation pressure gradient accelerations (VPPGA; yellow). Larger magnitudes of ACCD in reduced buoyancy environments lead to shallow mesovortices. Reproduced from Wade and Parker (2021).

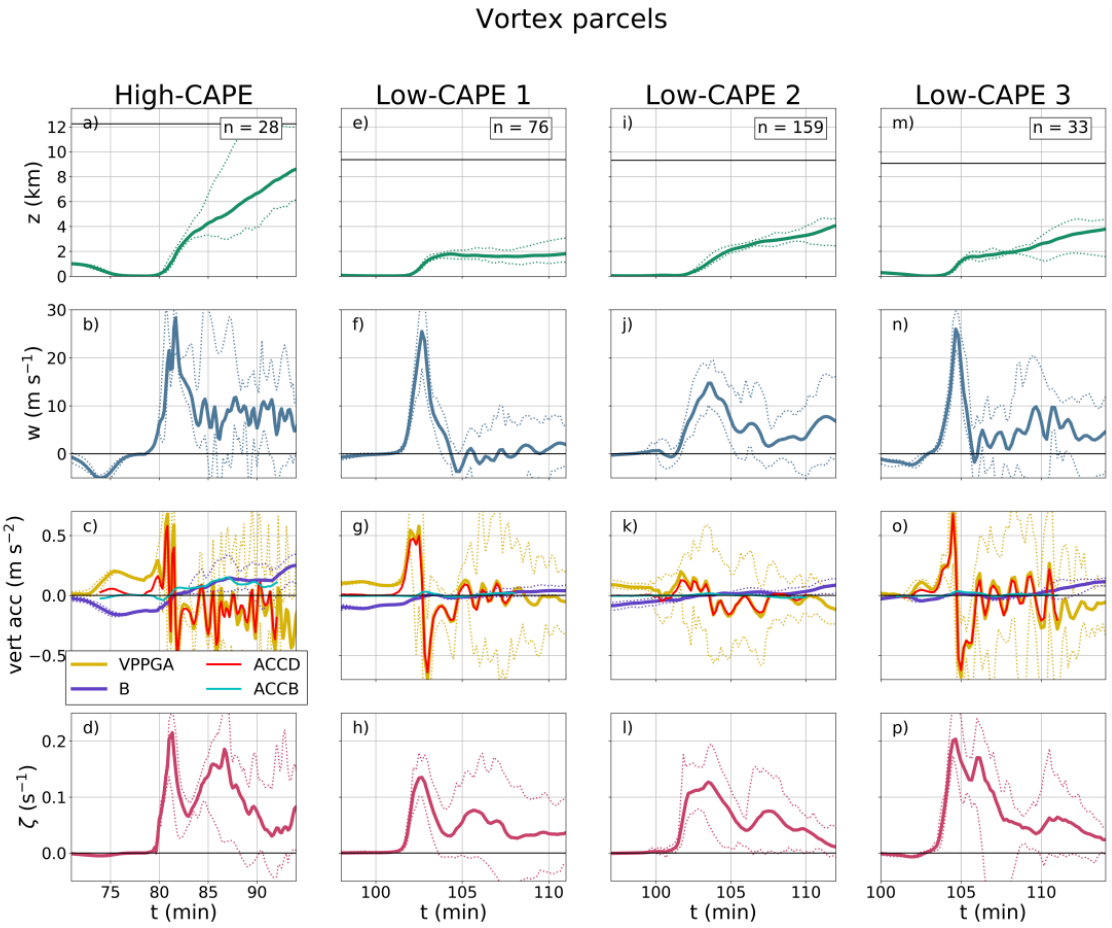

Figure 2.3: As in Figure 2.b, except in regard to parameters near the tornado-like vortex. Reproduced from Wade and Parker (2021).

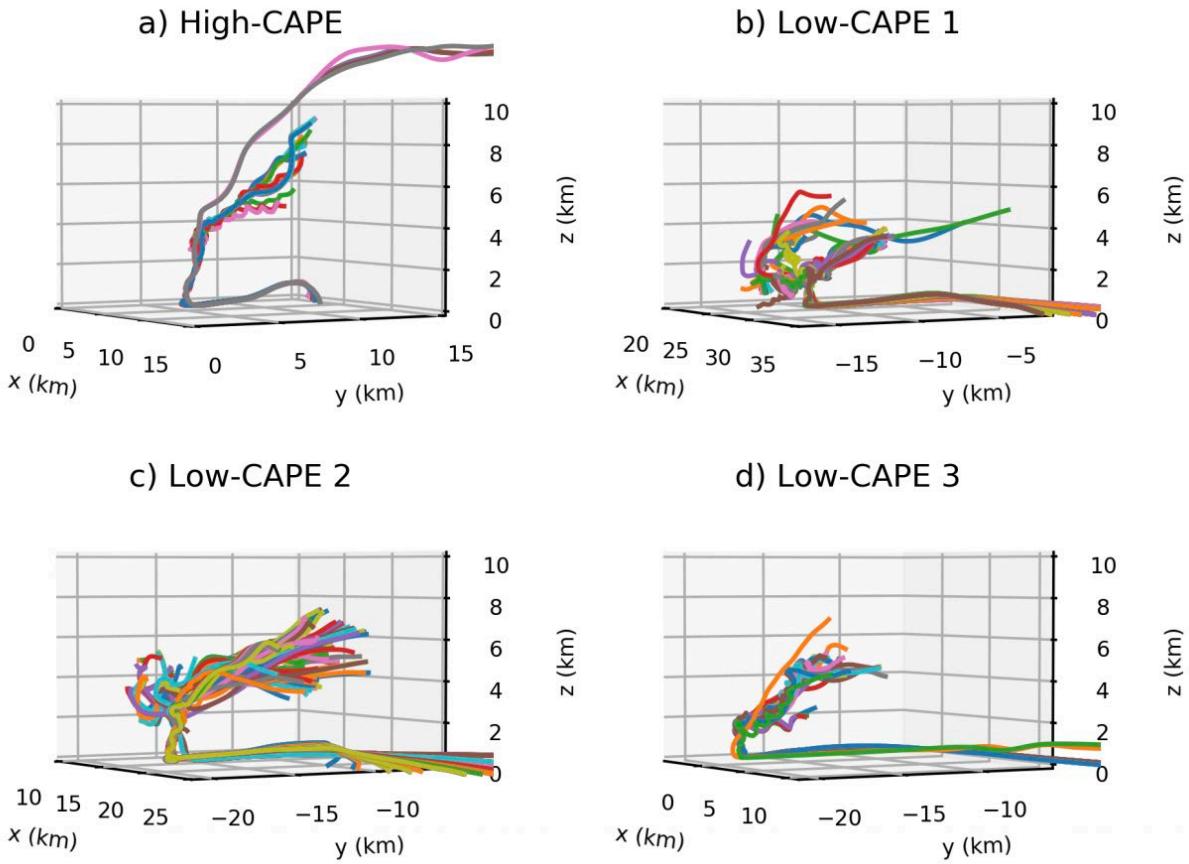

Figure 2.4: Trajectories of storm-ingested vortex parcels within environments with varying levels of instability. Reproduced from Wade and Parker (2021).

Reflectivity signatures	Criteria
Supercell vortices	
Hook echo	Appendage in 40-dBZ reflectivity contour on right-rear flank of supercell
(Bounded) Weak echo region-(B)WER	Notch (hole) of <40-dBZ reflectivity on right-rear flank of supercell with >50-dBZ reflectivity above
Nonsupercell vortices	
Gust-front cusp	Inflection point in a gust front in radial velocity field
Forward-inflow notch	Indentation in a 40-dBZ contour in the front of the convective line, with vertical continuity
Rear-inflow notch	Indentation in a 40-dBZ contour in the rear of the convective line, with vertical continuity
Bowing segment	Noticeable bow-shaped curvature in the 40-dBZ convective line
Broken S	Break or near break in the 40-dBZ convective line with vertical continuity, where the southern segment of the line surges ahead of the northern segment

Figure 2.5: Table with defined criteria for each of the radar reflectivity signatures associated with HSLC convection, both supercellular and non-supercellular. Reproduced from Davis and Parker (2014).

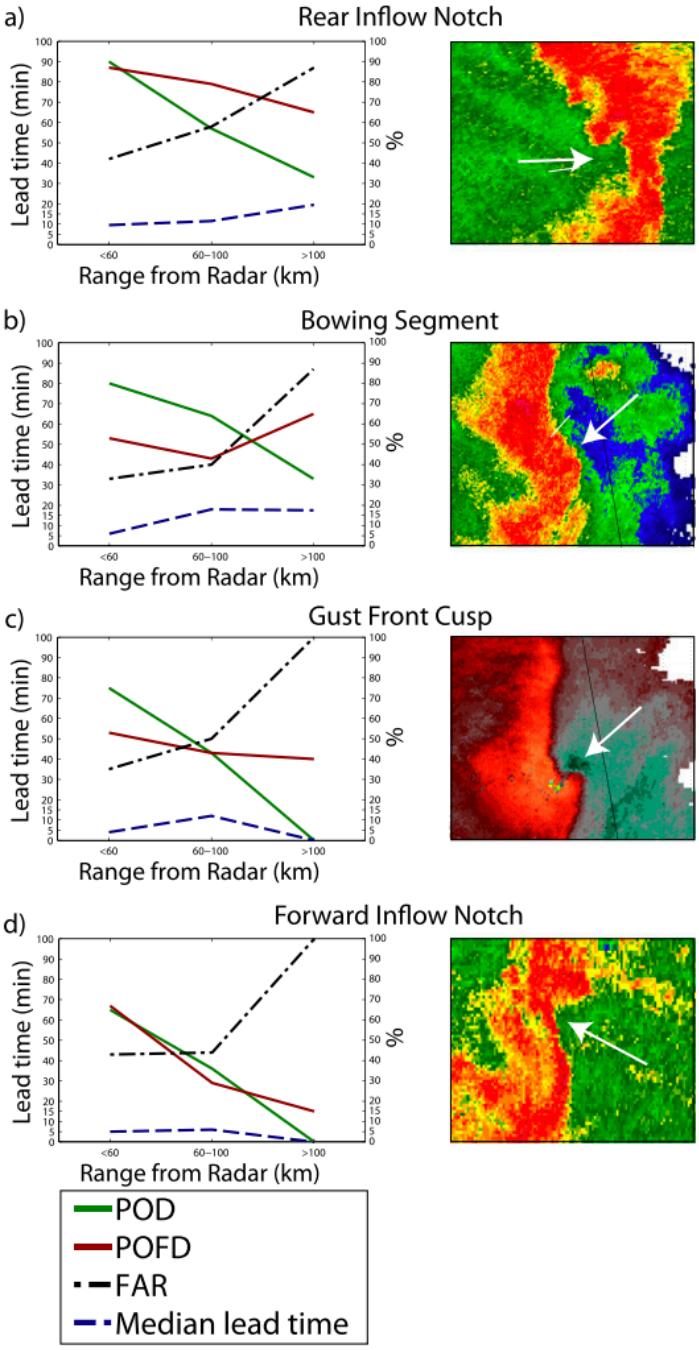

Figure 2.6: Sample HSLC radar reflectivity and velocity signatures (as labeled, right column), along with associated false alarm rate (FAR), probability of detection (POD), probability of false detection (POFD), and median lead time as a function of range from the radar and signature type. Reproduced from Davis and Parker (2014).

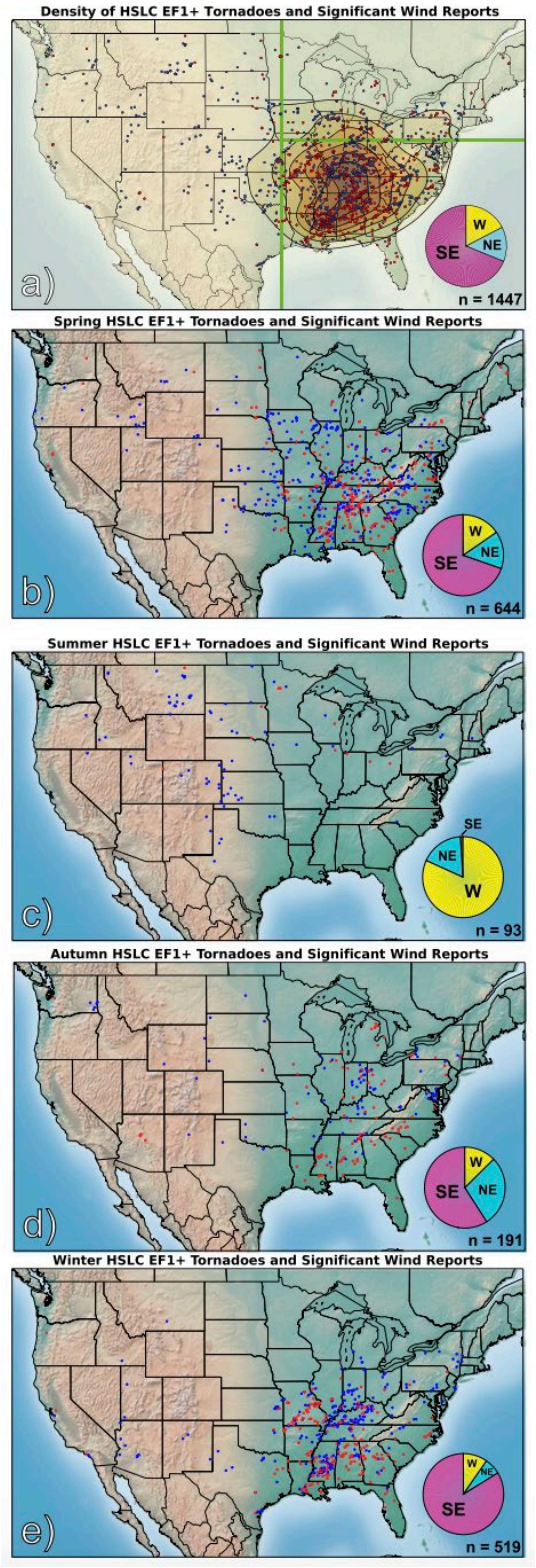

Figure 2.7: Map of EF1+ HSLC tornadoes (red dots) and significant wind reports (blue dots) across the US through varying seasons. The top panel includes an overlay with an approximated kernel density estimate. Reproduced from Sherburn et al. (2016).

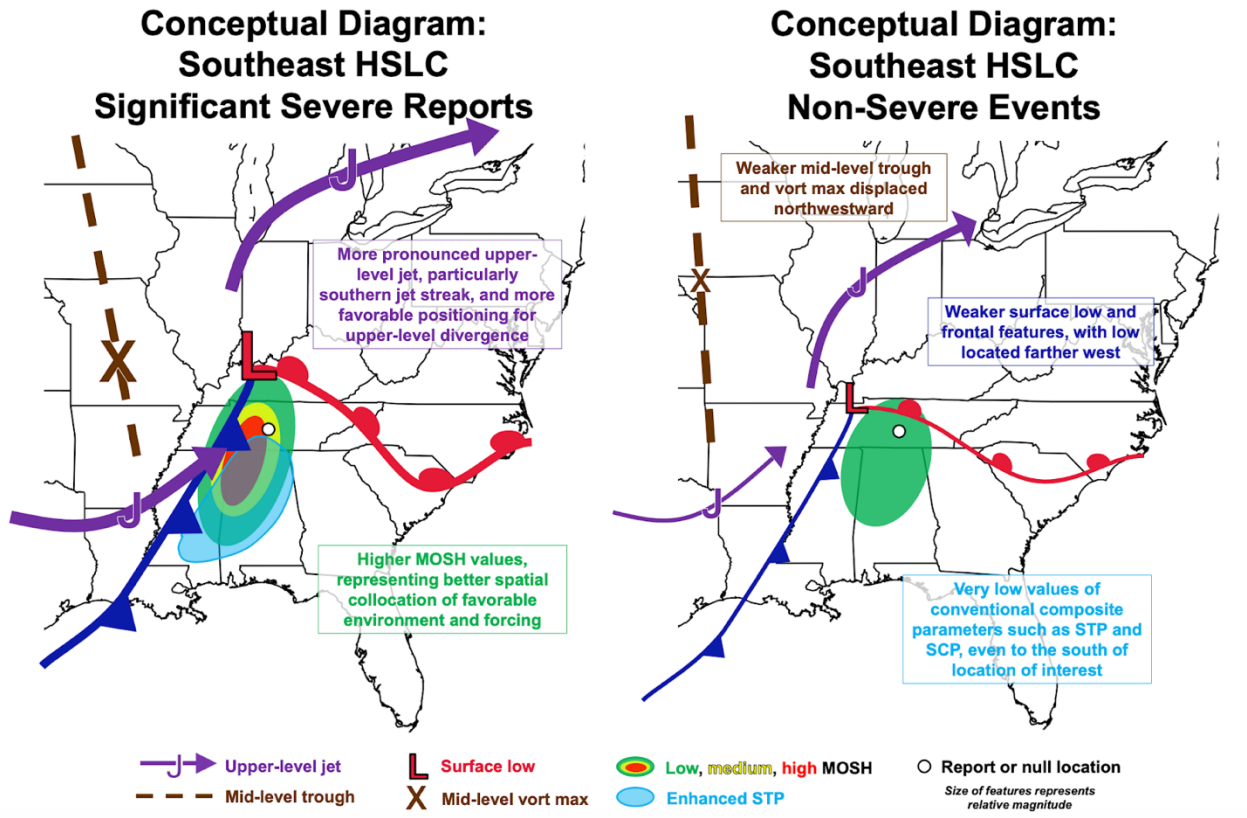

Figure 2.8, Conceptual diagrams showing differences in synoptic setups of significant severe and non-severe HSLC events in the Southeast US. Reproduced from Sherburn and Parker (2016).

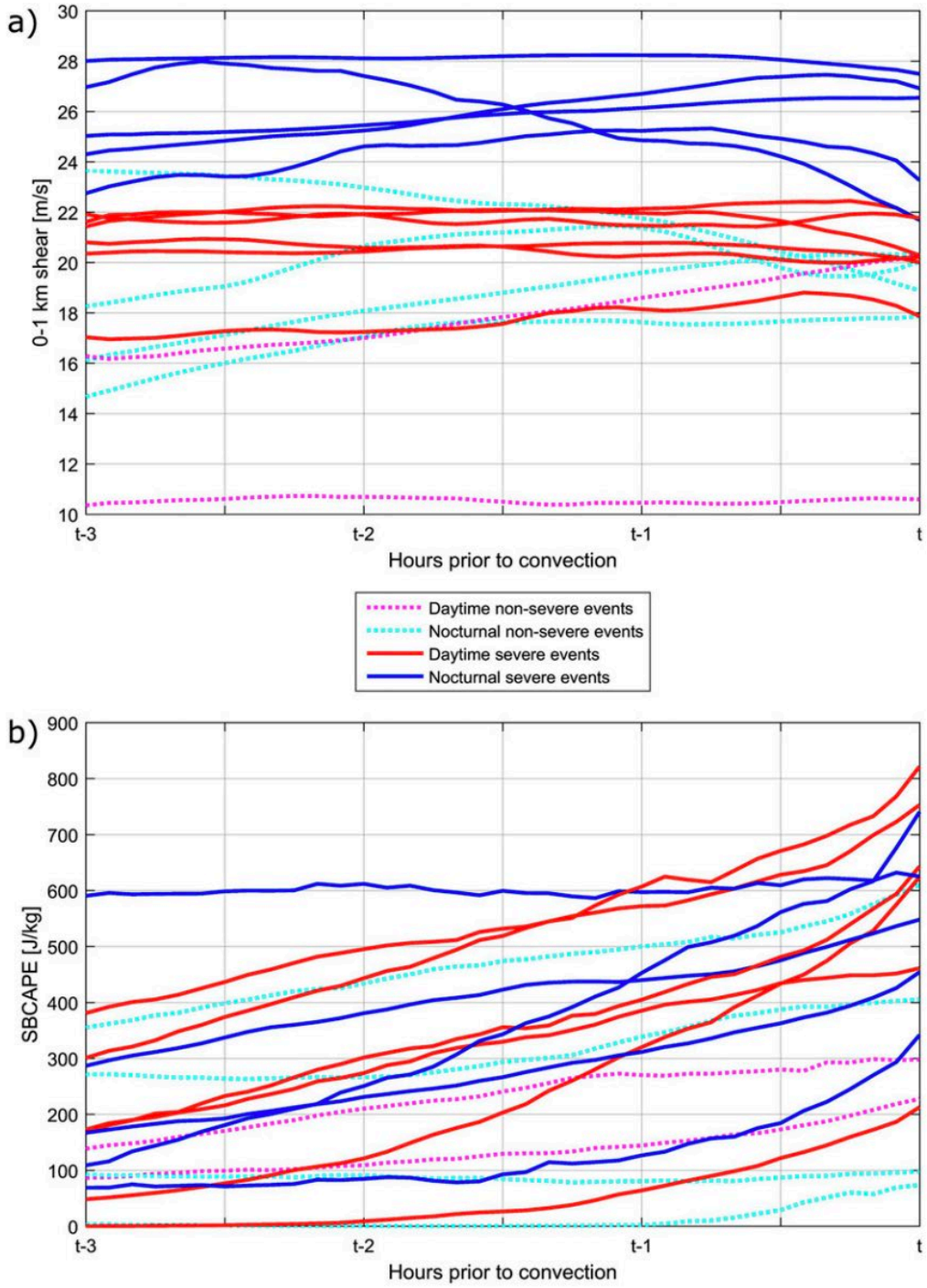

Figure 2.9: Time series of average a) 0-1 km shear and b) SBCAPE values, separated out by severe versus non-severe and daytime versus nocturnal events. Reproduced from King et al. (2017).

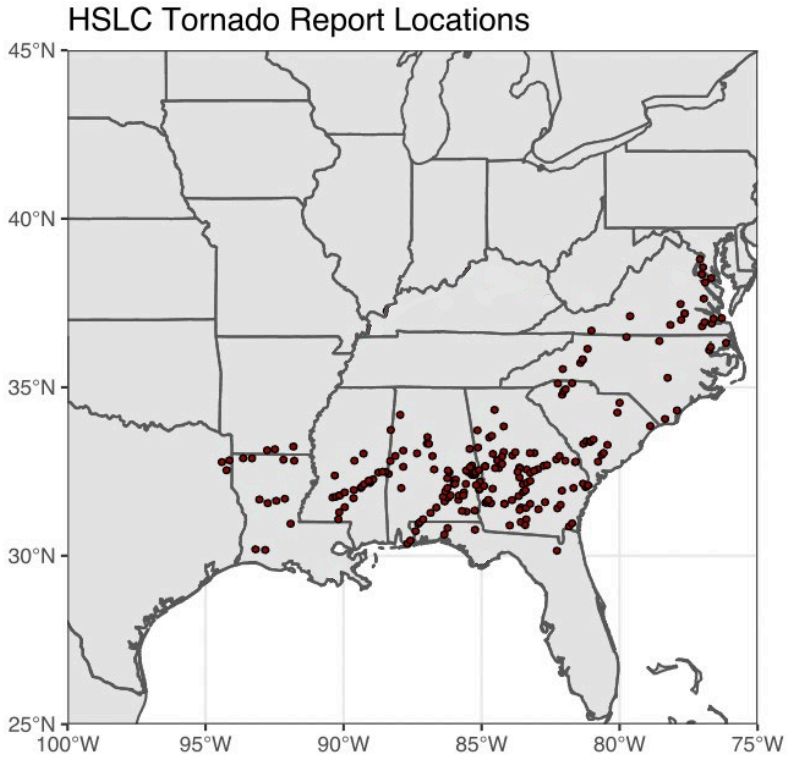

Figure 3.1: Image showing spatial distribution of dataset of HSLC tornado reports.

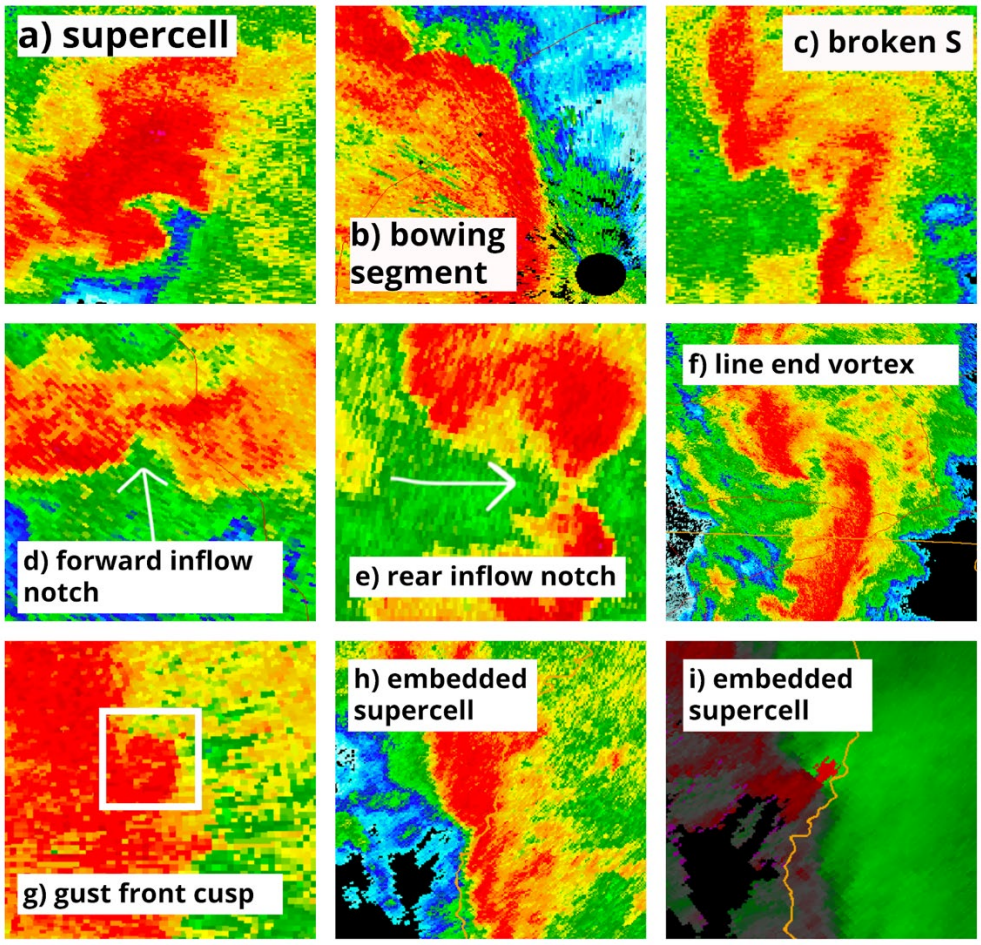

Figure 3.2: a) HSLC supercell, as documented using archived KDGX radar reflectivity data valid 1836 UTC 15 February 2016; b) Bowing segment as documented using archived KFFC radar reflectivity data valid 2150 UTC 18 November 2015; c) Broken S as documented using archived KFFC radar reflectivity data valid 1612 UTC 21 January 2017; d) Forward inflow notch as documented using archived KMXX radar reflectivity data valid 0406 UTC 7 April 2016; e) Rear inflow notch as documented using archived KCLX radar reflectivity data valid 1954 UTC 1 January 2017; f) Line end vortex as documented using archived KGSP radar reflectivity data valid 2001Z 23 October 2017; g) Gust front cusp as documented using archived KGWX reflectivity data valid 2307 UTC 3 January 2015; Embedded supercell as documented using archived KMXX radar reflectivity (h) and radial velocity (i) data valid 2002 23 November 2014.

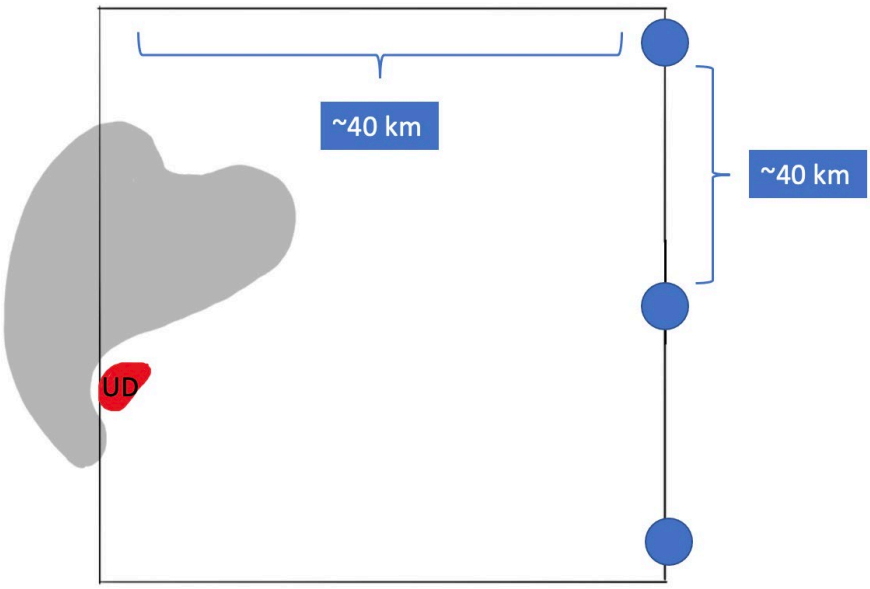

Figure 3.3: Schematic showing an idealized, supercell-based example of the grid set-up used for obtaining environmental soundings for each tornado report in the dataset. Red color represents location of updraft.

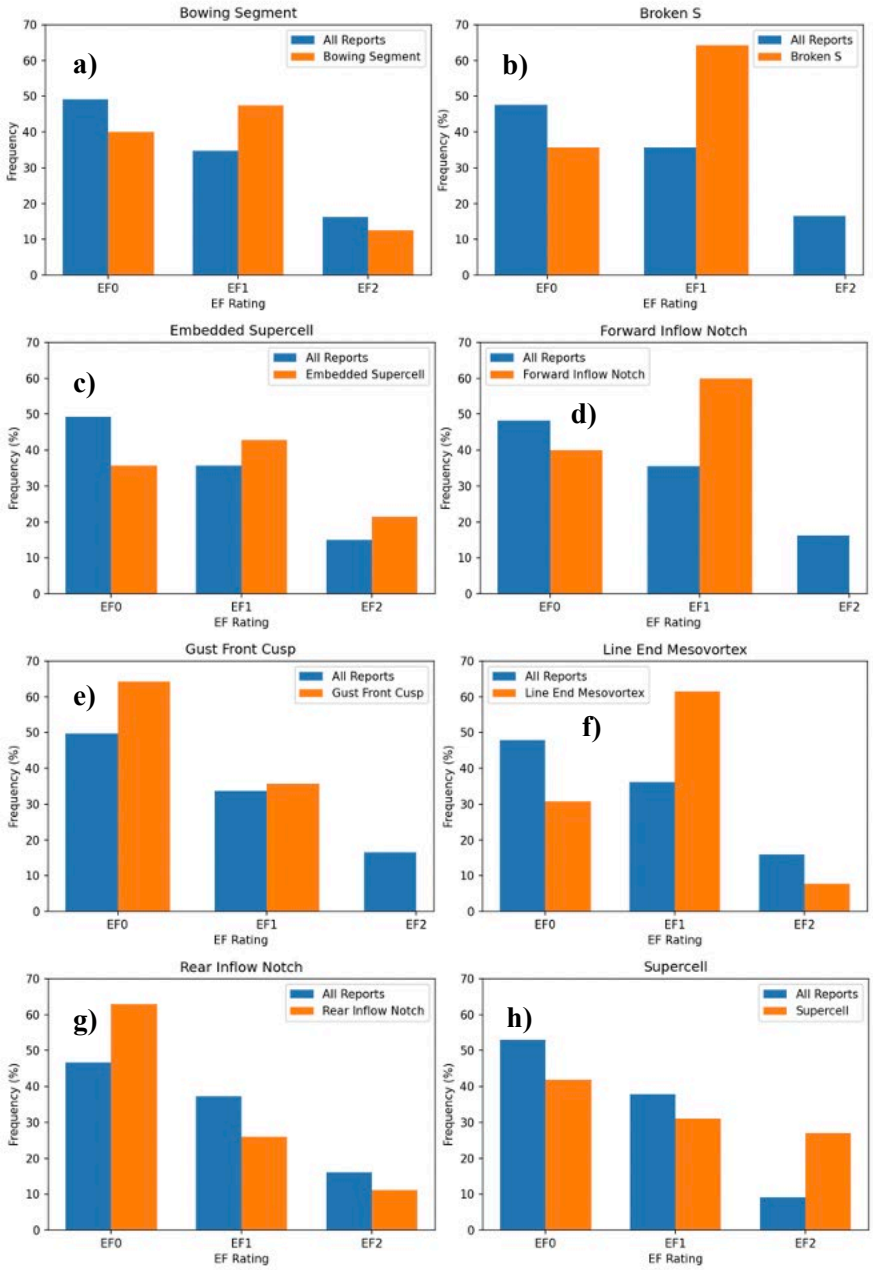

Figure 4.1: EF rating of HSLC tornado reports within the dataset aggregated by reflectivity signature.

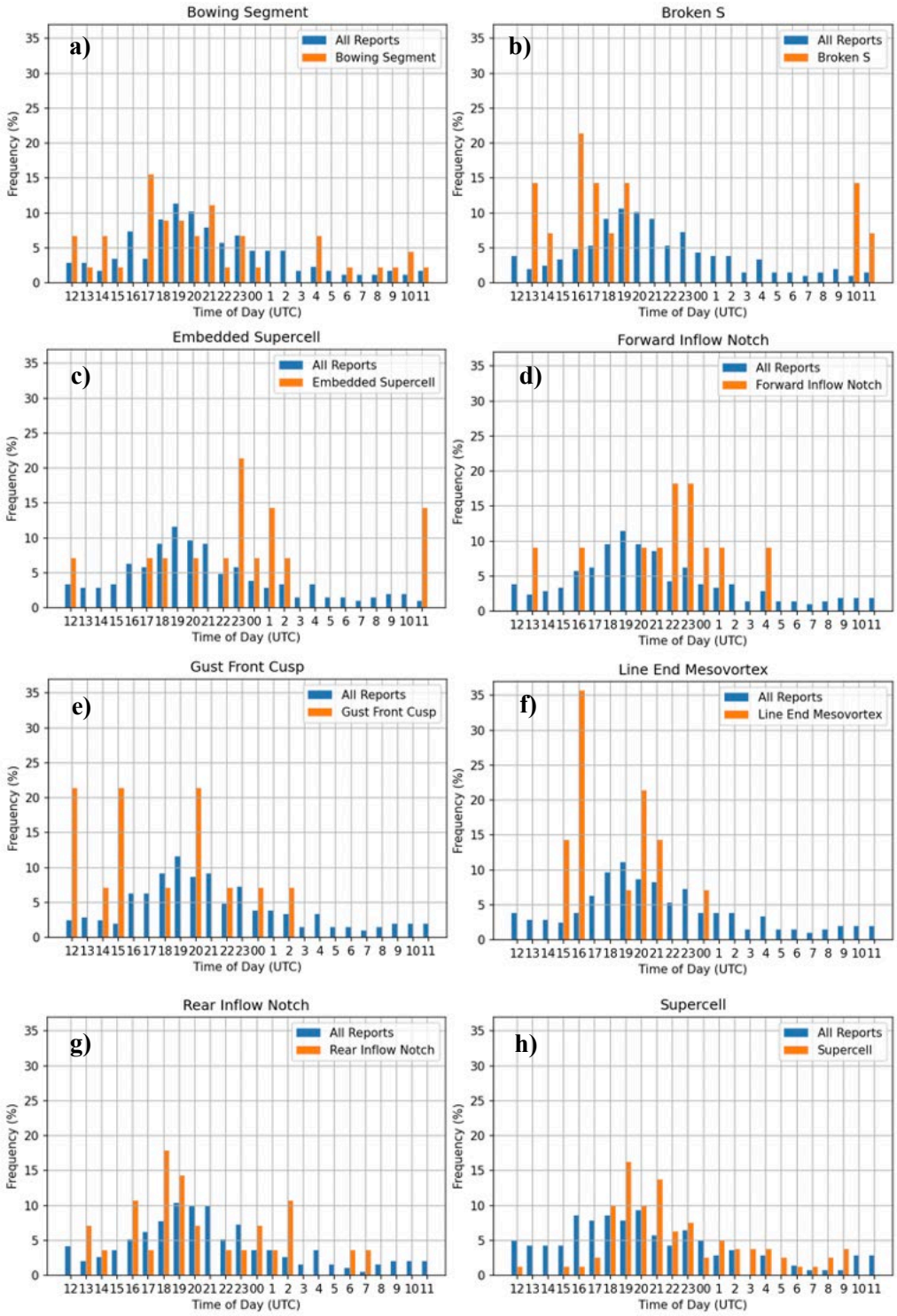

Figure 4.2: Diurnal pattern of HSLC tornado report occurrence within the dataset aggregated by reflectivity signature.

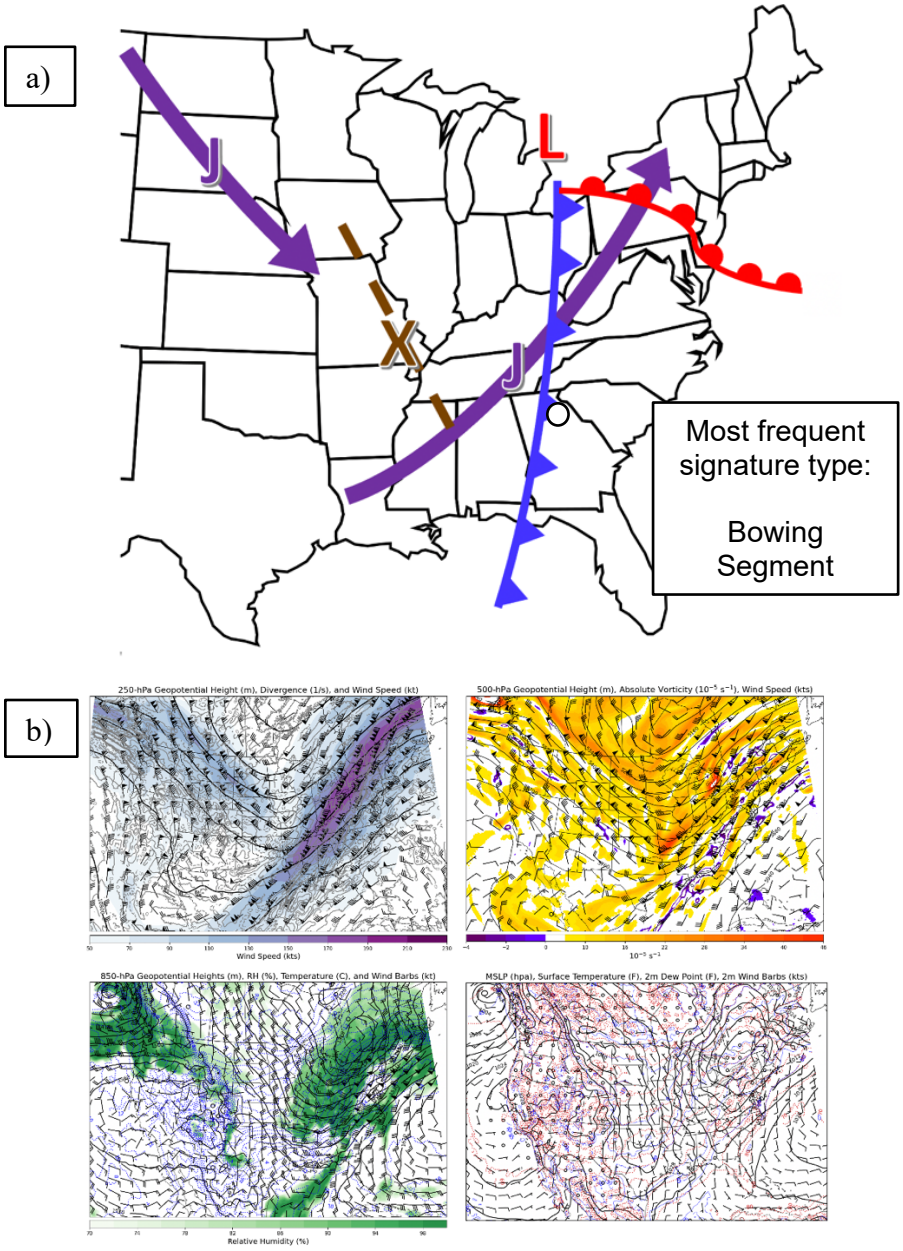

Figure 4.3: a) Schematic representing composite synoptic setup for 7/25 severe weather event days within the dataset, characterized by a broad surface cyclone near the Great Lakes. Purple arrows indicate jet location, brown dashed line indicates mid-level trough axis, brown "X" indicates location of mid-level vorticity maxima, white circle represent approximate centroid of tornado reports; b) 4-panel synoptic map valid 4 January 2015 at 1600 UTC with RAP-13km 250-hPa geopotential height, divergence, and wind speed (top left), 500-hPa geopotential height, absolute vorticity, and wind speed (top right), 850-hPa geopotential height, relative humidity, and wind barbs (bottom left), and MSLP, surface temperature, 2-m dew point temperature, and wind barbs (bottom right).

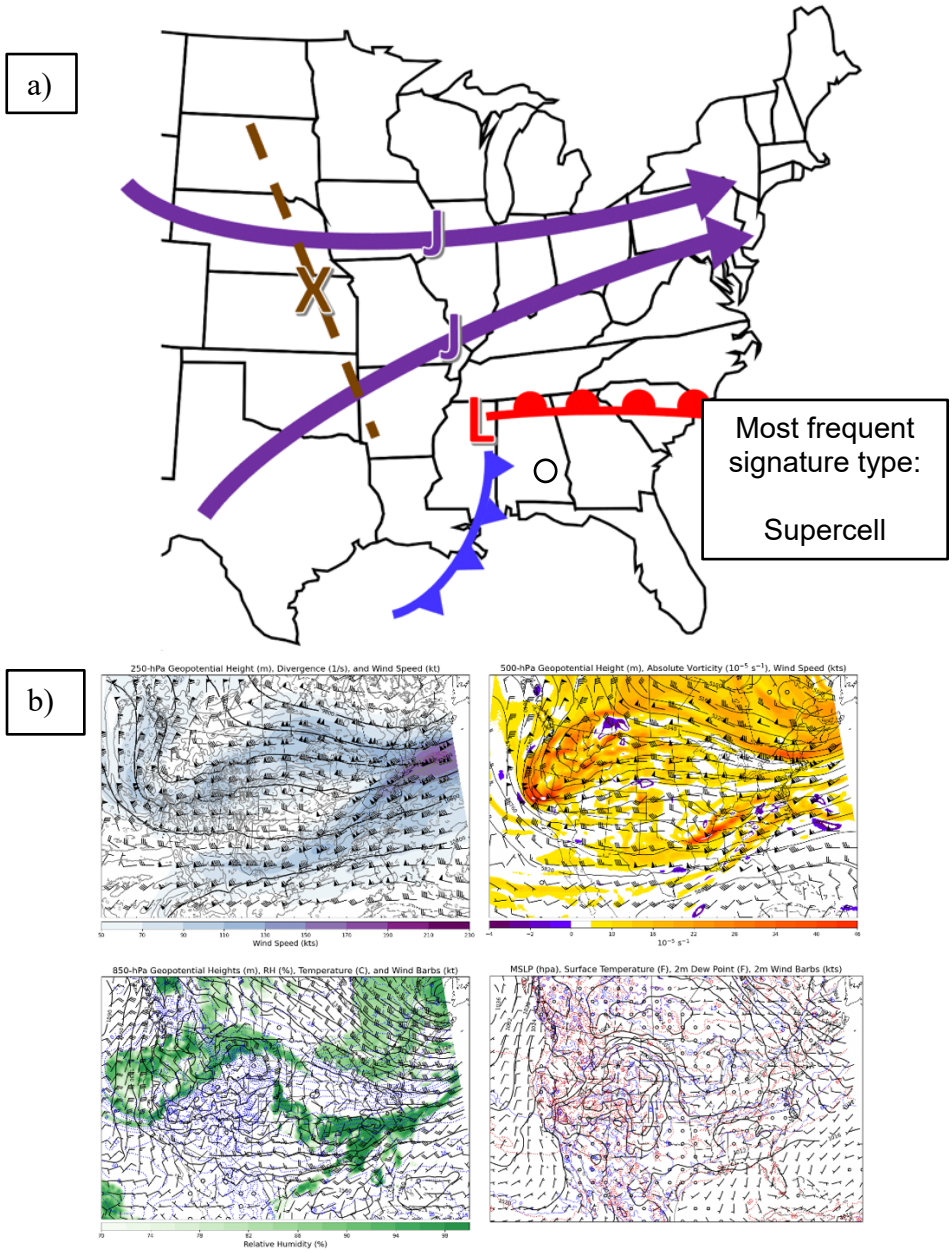

Figure 4.4: a) Schematic representing composite synoptic setup for 3/25 severe weather event days within the dataset, characterized by broad confluent flow in the eastern CONUS. Purple arrows indicate jet location, brown dashed line indicates mid-level trough axis, brown "X" indicates location of mid-level vorticity maxima, white circle represent approximate centroid of tornado reports; b) 4-panel synoptic map valid 20 December 2017 at 1800 UTC with RAP-13km 250-hPa geopotential height, divergence, and wind speed (top left), 500-hPa geopotential height, absolute vorticity, and wind speed (top right), 850-hPa geopotential height, relative humidity, and wind barbs (bottom left), and MSLP, surface temperature, 2-m dew point temperature, and wind barbs (bottom right).

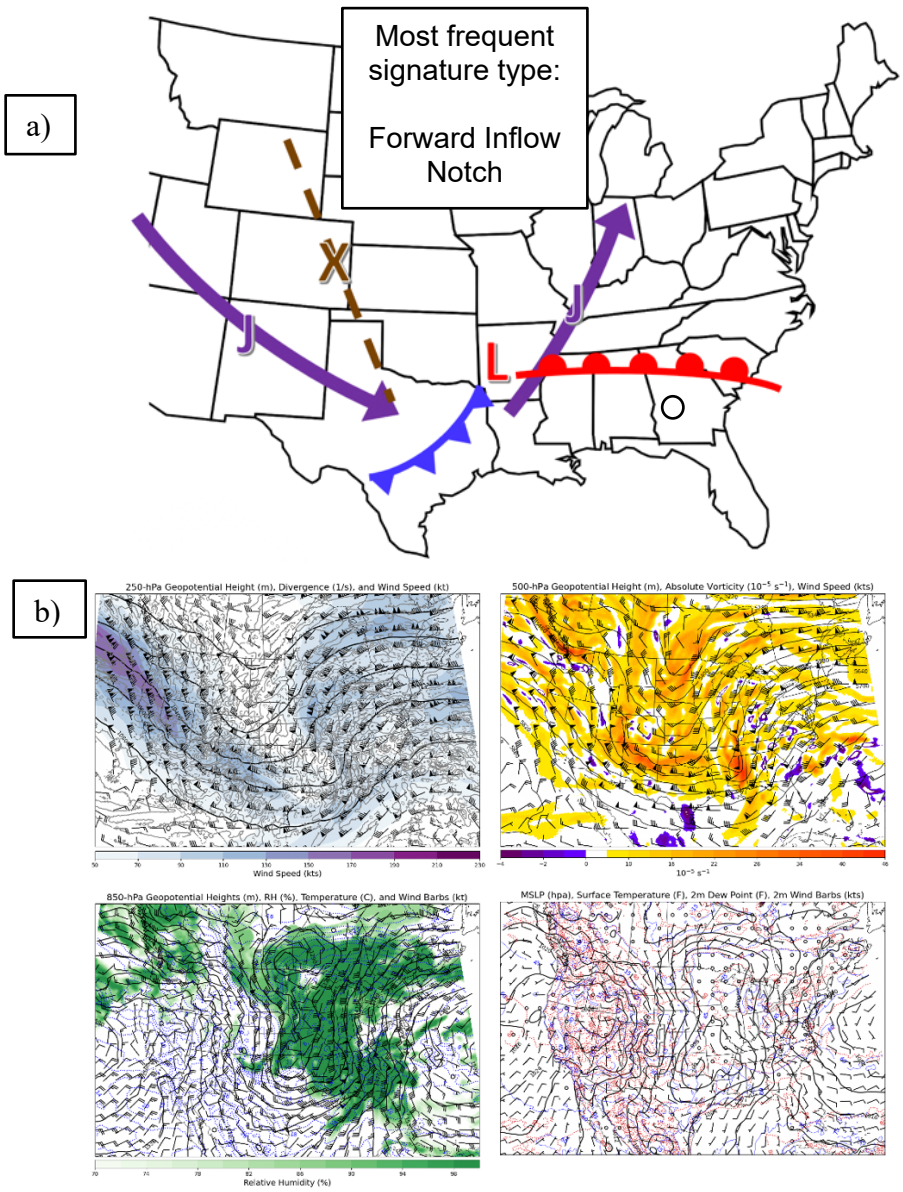

Figure 4.5: a) Schematic representing composite synoptic setup for 2/25 severe weather event days within the dataset, characterized by a western-displaced mid-level trough. Purple arrows indicate jet location, brown dashed line indicates mid-level trough axis, brown "X" indicates location of mid-level vorticity maxima, white circle represent approximate centroid of tornado reports; b) 4-panel synoptic map valid 23 November 2014 at 2000 UTC with RAP-13km 250-hPa geopotential height, divergence, and wind speed (top left), 500-hPa geopotential height, absolute vorticity, and wind speed (top right), 850-hPa geopotential height, relative humidity, and wind barbs (bottom left), and MSLP, surface temperature, 2-m dew point temperature, and wind barbs (bottom right).

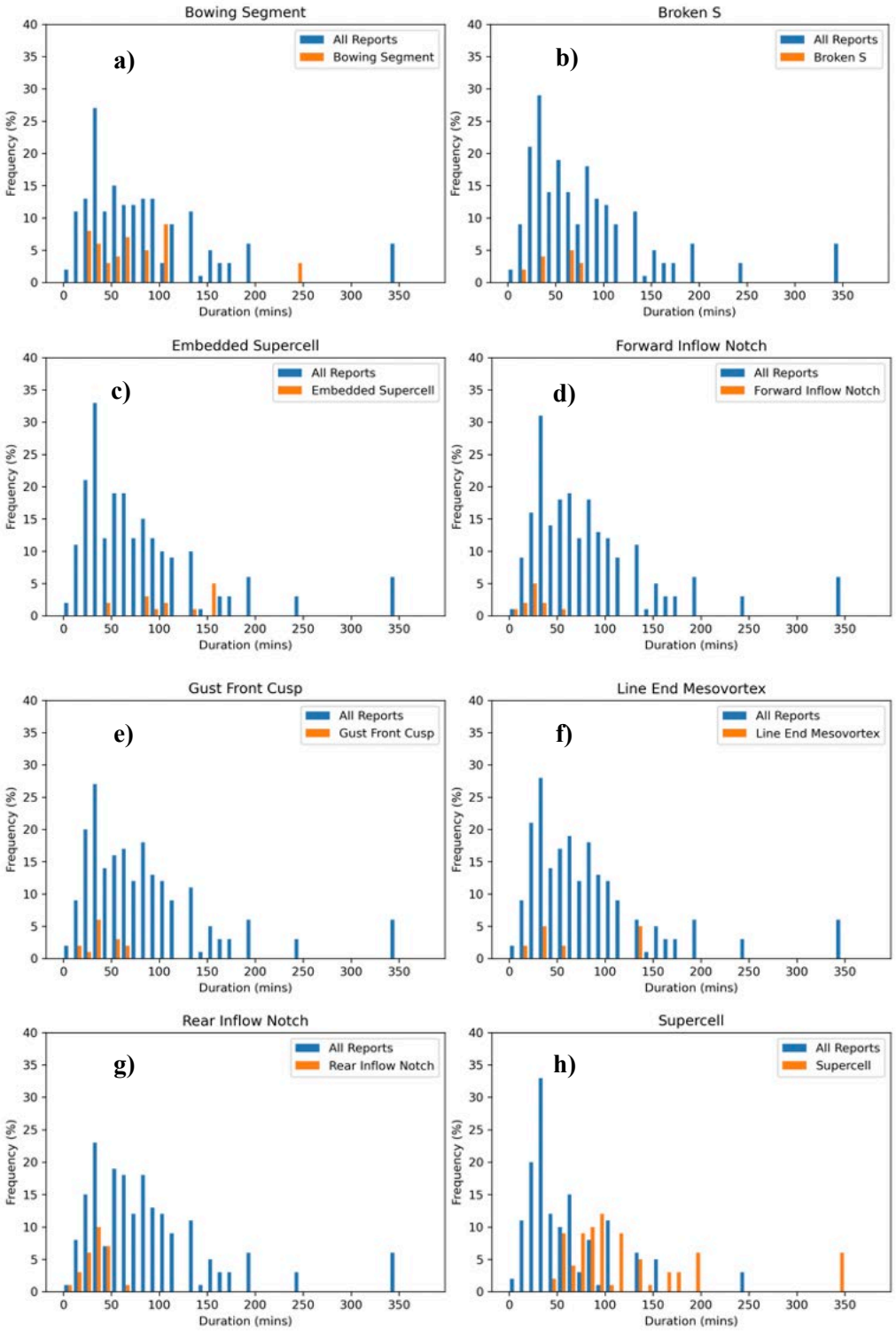

Figure 4.6: Breakdown of duration of reflectivity signatures associated with the HSLC tornado dataset.

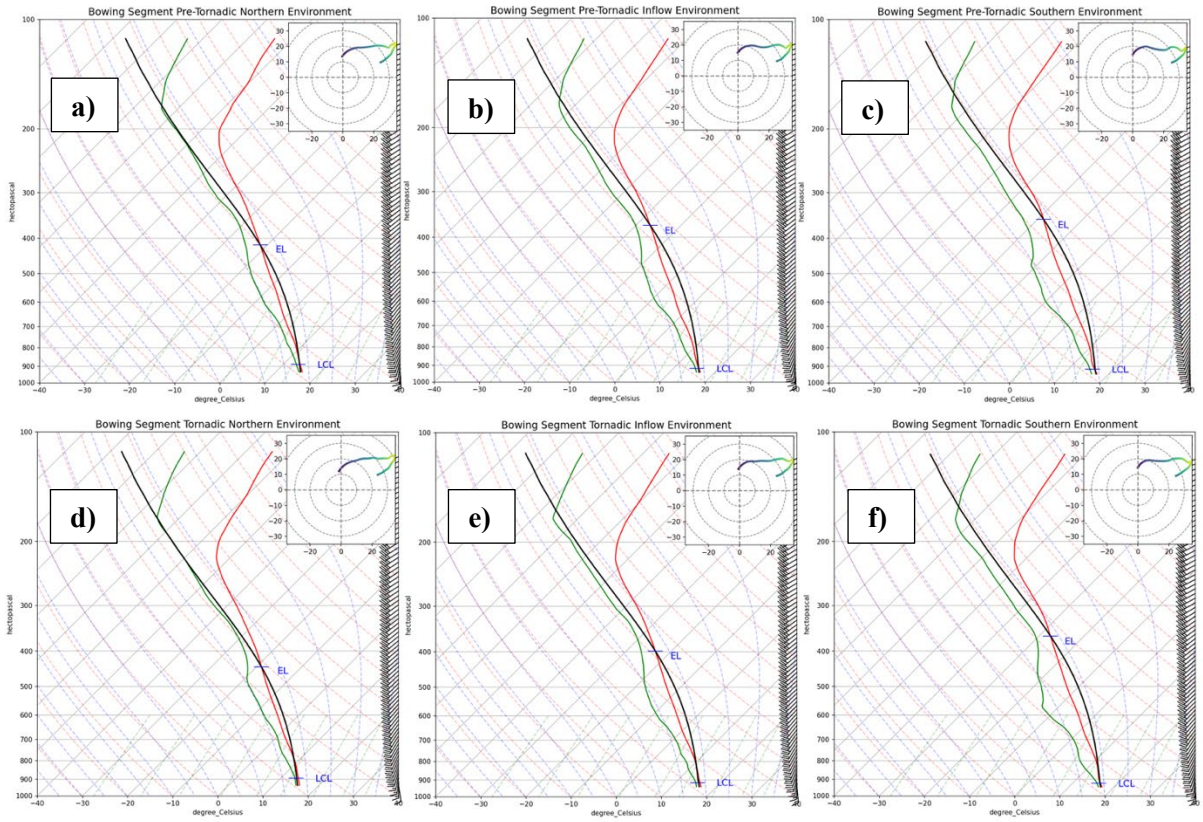

Figure 4.7: Composite soundings representing the pre-tornadic northern (a), pre-tornadic inflow (b), pre-tornadic southern (c), tornadic northern (d), tornadic inflow (e), and tornadic northern (f) environments for HSLC tornadoes associated with bowing segments. Pre-tornadic soundings are valid the hour before the tornado report (T-1); tornadic soundings are valid the hour of the tornado report (T=0).

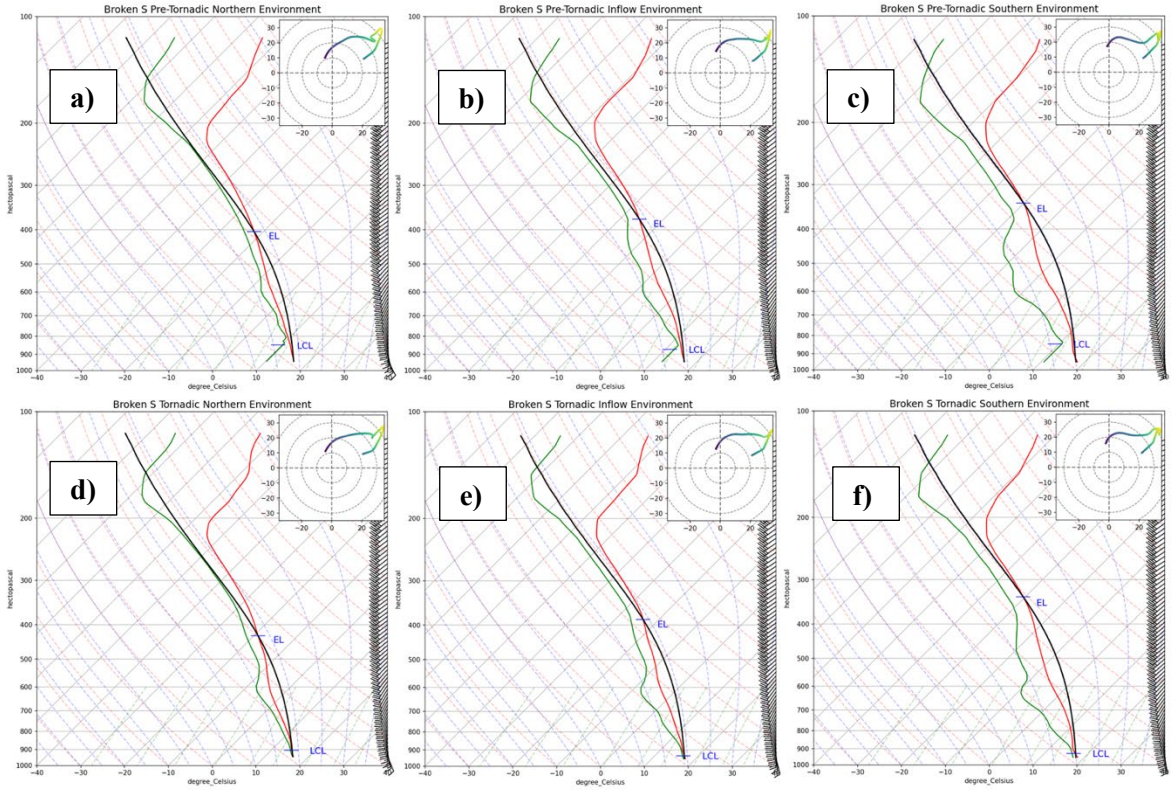

Figure 4.8: Composite soundings representing the pre-tornadic northern (a), pre-tornadic inflow (b), pre-tornadic southern (c), tornadic northern (d), tornadic inflow (e), and tornadic northern (f) environments for HSLC tornadoes associated with broken S reflectivity signatures. Pre-tornadic soundings are valid the hour before the tornado report (T-1); tornadic soundings are valid the hour of the tornado report (T=0).

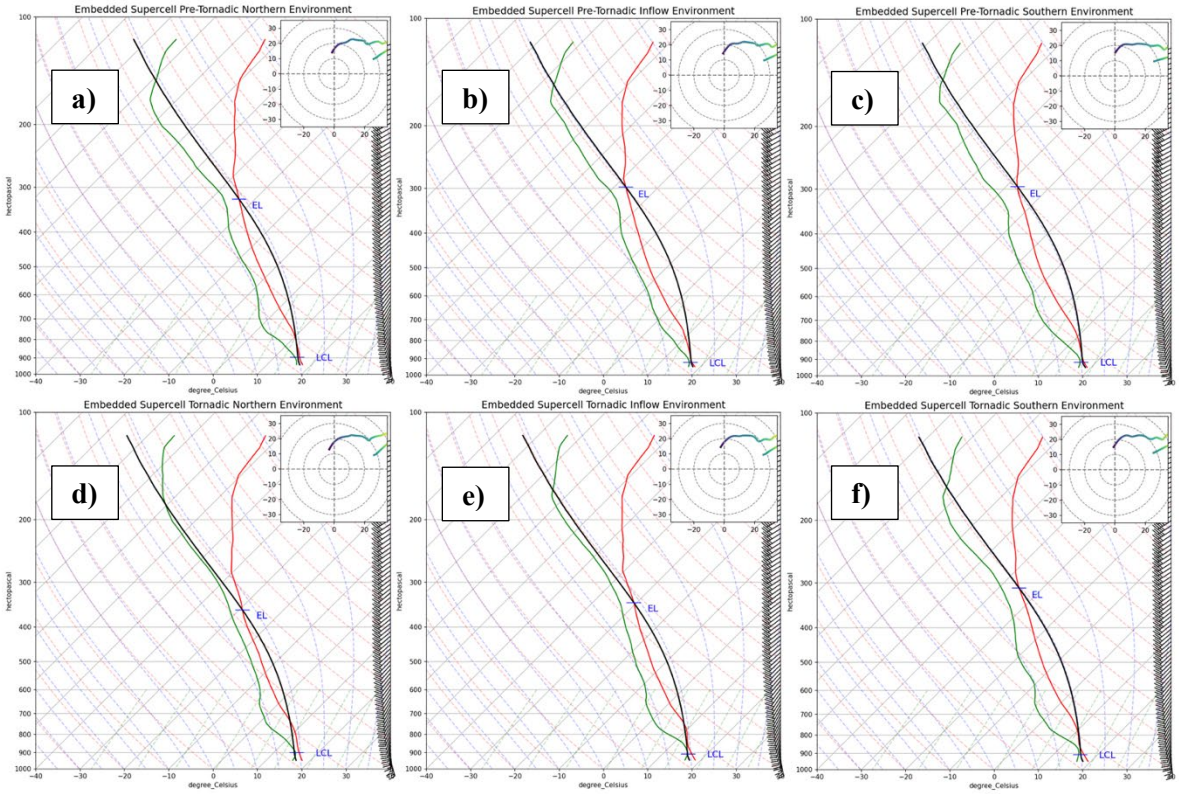

Figure 4.9: Composite soundings representing the pre-tornadic northern (a), pre-tornadic inflow (b), pre-tornadic southern (c), tornadic northern (d), tornadic inflow (e), and tornadic northern (f) environments for HSLC tornadoes associated with embedded supercells. Pre-tornadic soundings are valid the hour before the tornado report (T-1); tornadic soundings are valid the hour of the tornado report (T=0).

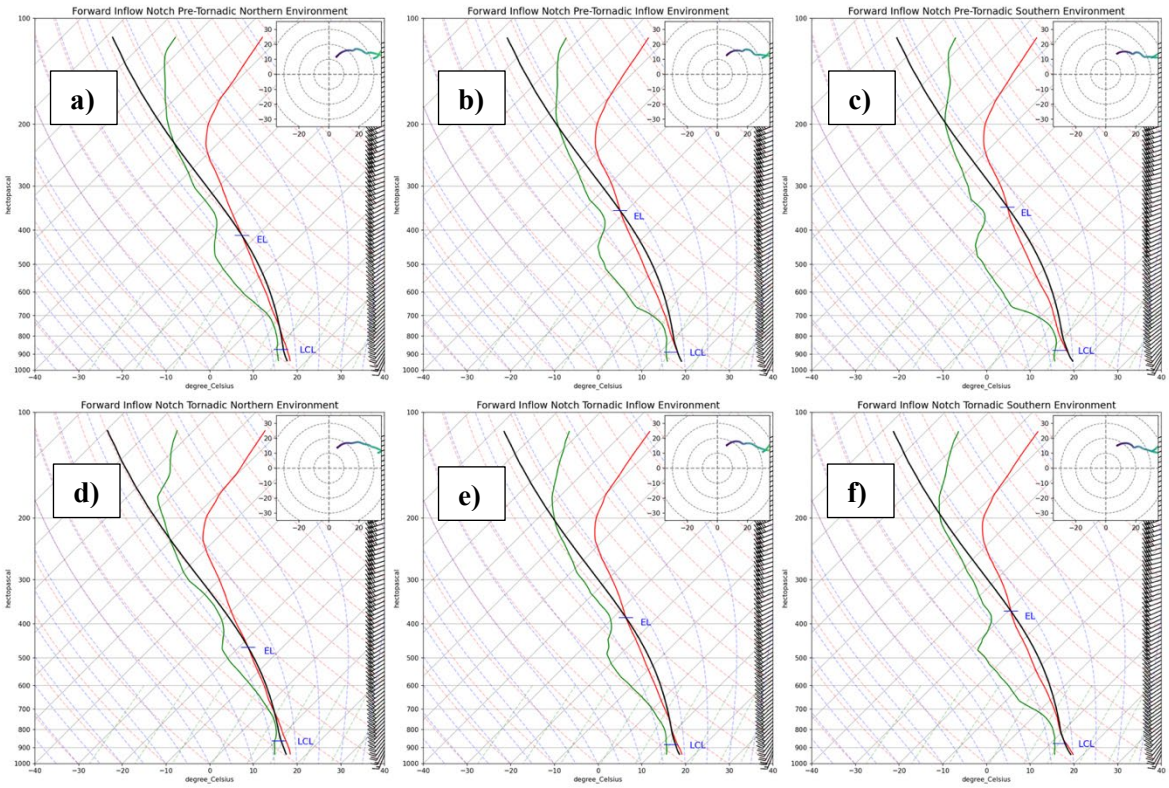

Figure 4.10: Composite soundings representing the pre-tornadic northern (a), pre-tornadic inflow (b), pre-tornadic southern (c), tornadic northern (d), tornadic inflow (e), and tornadic northern (f) environments for HSLC tornadoes associated with forward inflow notches. Pre-tornadic soundings are valid the hour before the tornado report (T-1); tornadic soundings are valid the hour of the tornado report (T=0).

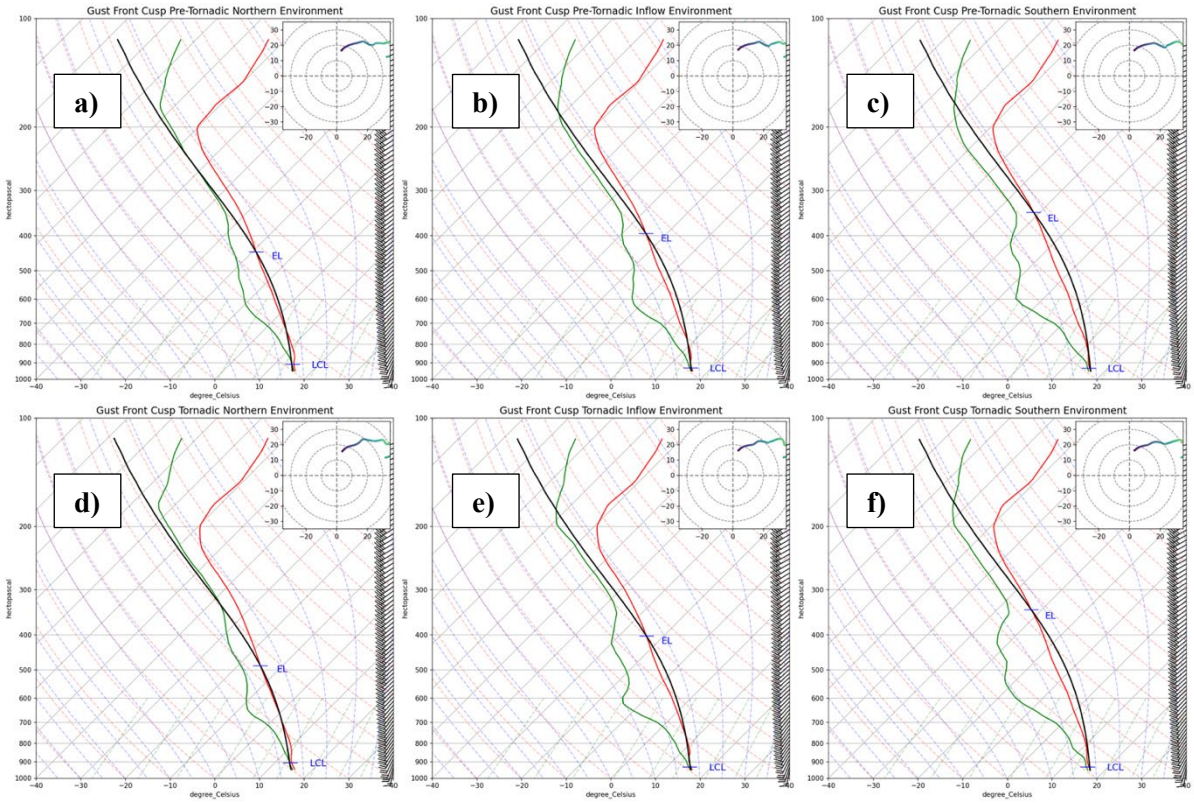

Figure 4.11: Composite soundings representing the pre-tornadic northern (a), pre-tornadic inflow (b), pre-tornadic southern (c), tornadic northern (d), tornadic inflow (e), and tornadic northern (f) environments for HSLC tornadoes associated with gust front cusp reflectivity signatures. Pre-tornadic soundings are valid the hour before the tornado report (T-1); tornadic soundings are valid the hour of the tornado report (T=0).

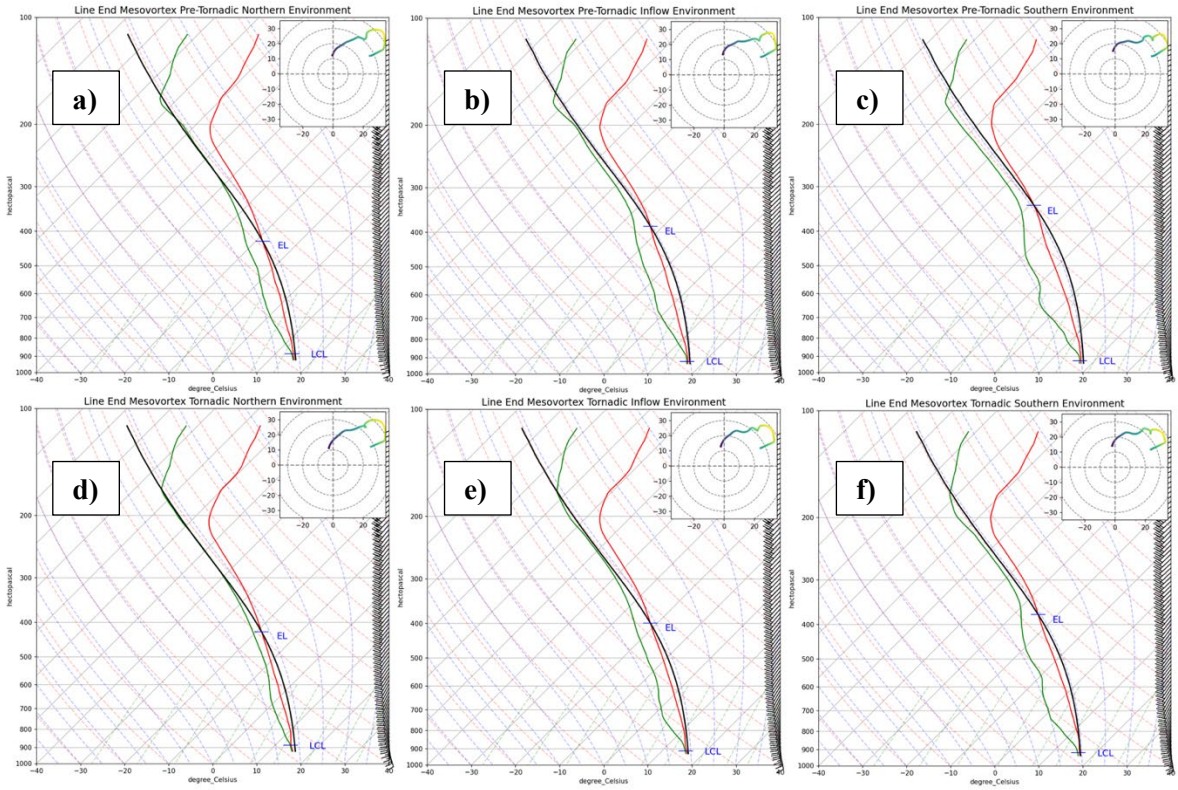

Figure 4.12: Composite soundings representing the pre-tornadic northern (a), pre-tornadic inflow (b), pre-tornadic southern (c), tornadic northern (d), tornadic inflow (e), and tornadic northern (f) environments for HSLC tornadoes associated with line end mesovortices. Pre-tornadic soundings are valid the hour before the tornado report (T-1); tornadic soundings are valid the hour of the tornado report (T=0).

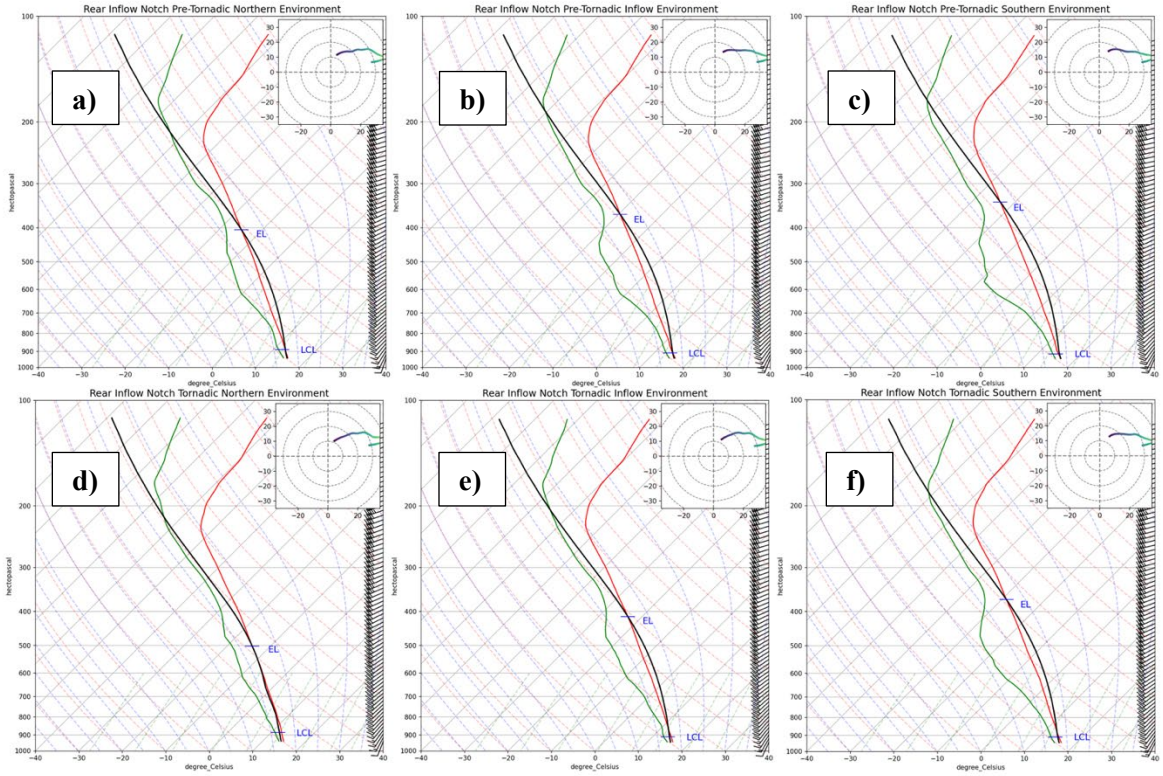

Figure 4.13: Composite soundings representing the pre-tornadic northern (a), pre-tornadic inflow (b), pre-tornadic southern (c), tornadic northern (d), tornadic inflow (e), and tornadic northern (f) environments for HSLC tornadoes associated with rear inflow notch reflectivity signatures. Pre-tornadic soundings are valid the hour before the tornado report (T-1); tornadic soundings are valid the hour of the tornado report (T=0).

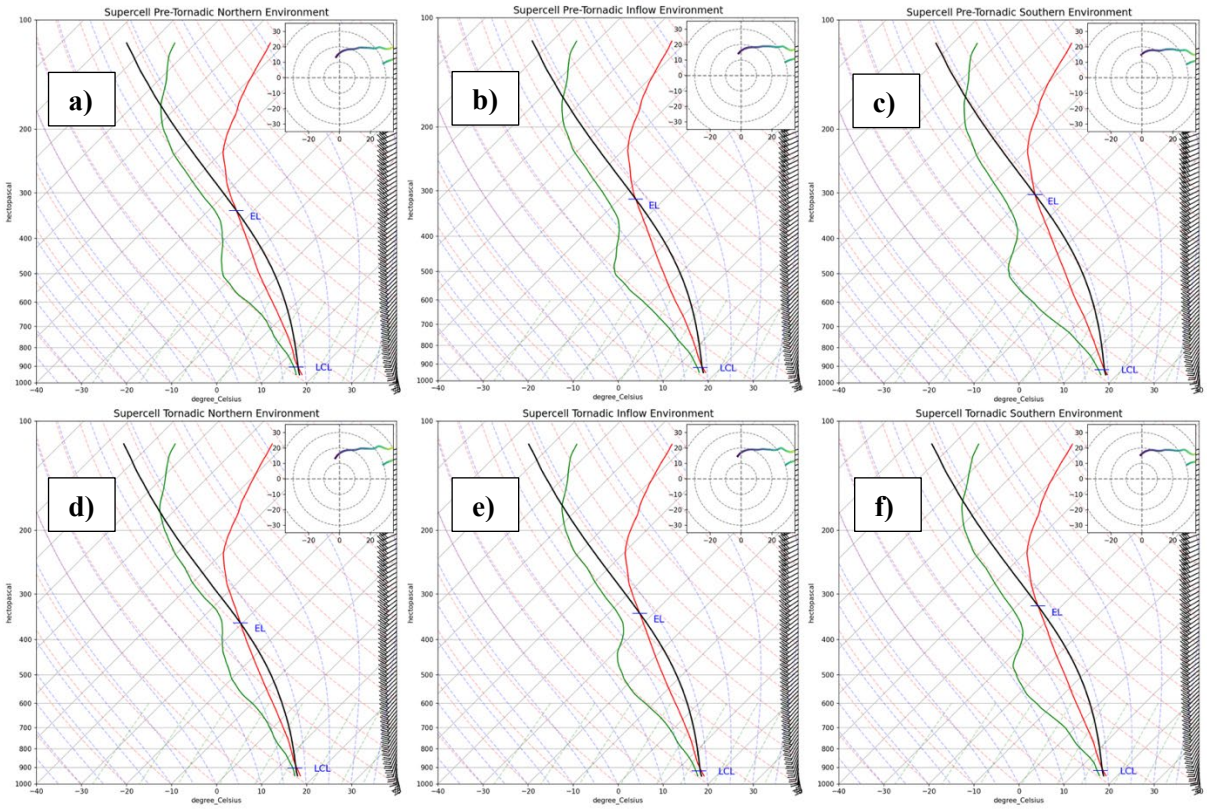

Figure 4.14: Composite soundings representing the pre-tornadic northern (a), pre-tornadic inflow (b), pre-tornadic southern (c), tornadic northern (d), tornadic inflow (e), and tornadic northern (f) environments for HSLC tornadoes associated with supercells. Pre-tornadic soundings are valid the hour before the tornado report (T-1); tornadic soundings are valid the hour of the tornado report (T=0).

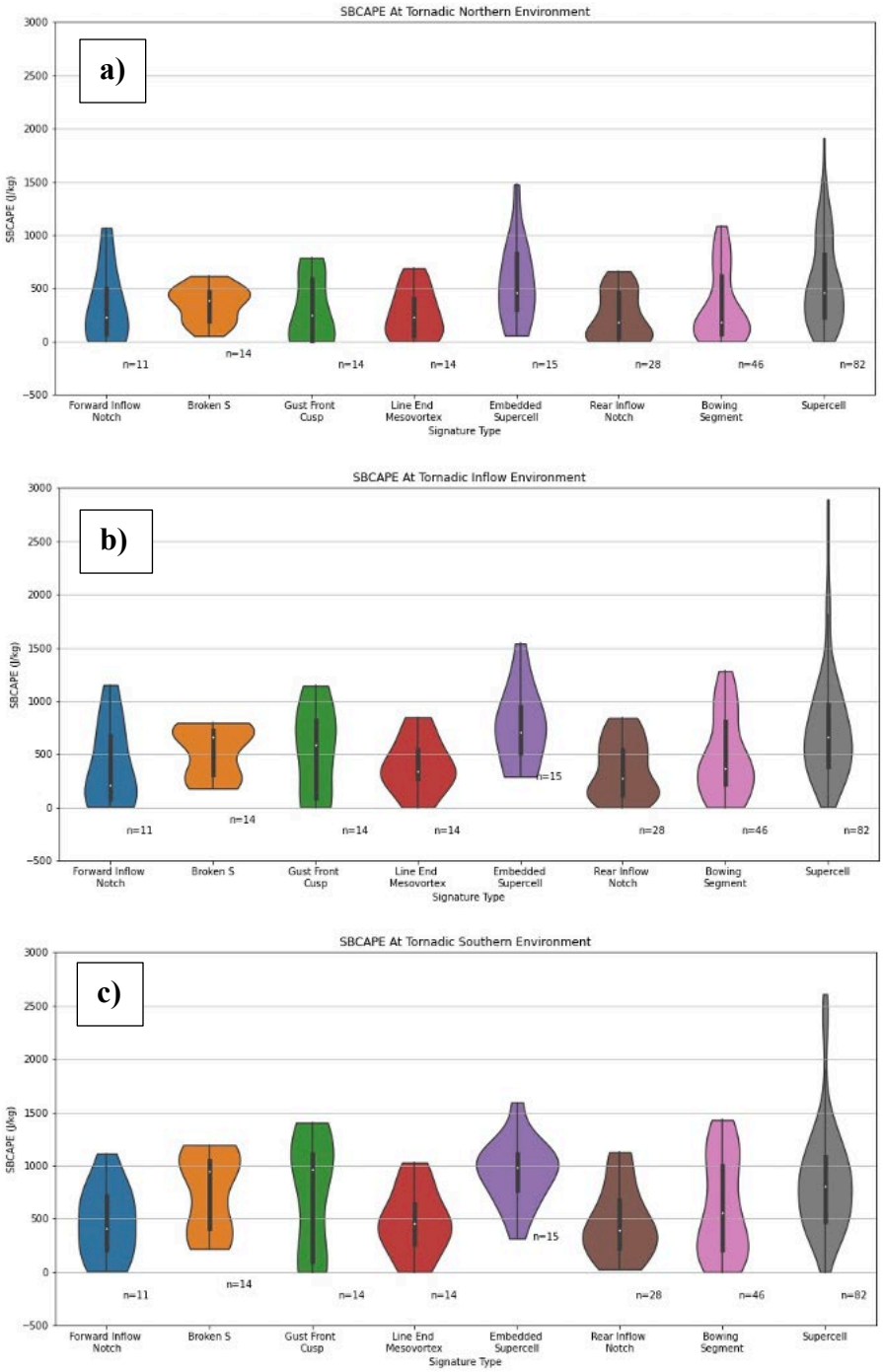

Figure 4.15: SBCAPE at a) northern, b) inflow, and c) southern environmental analysis points at the time of tornadogenesis.

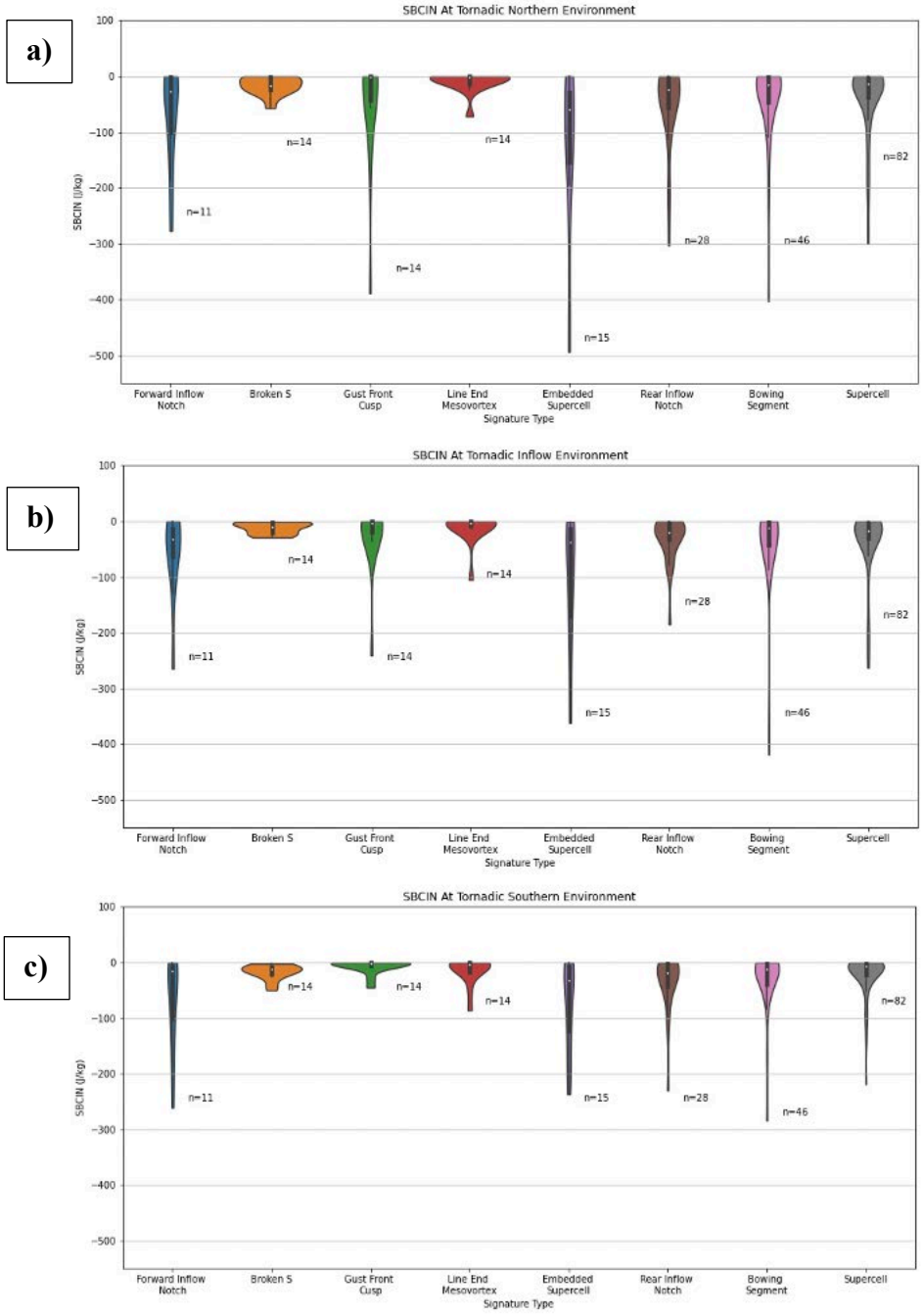

Figure 4.16: SBCIN at a) northern, b) inflow, and c) southern environmental analysis points at the time of tornadogenesis.

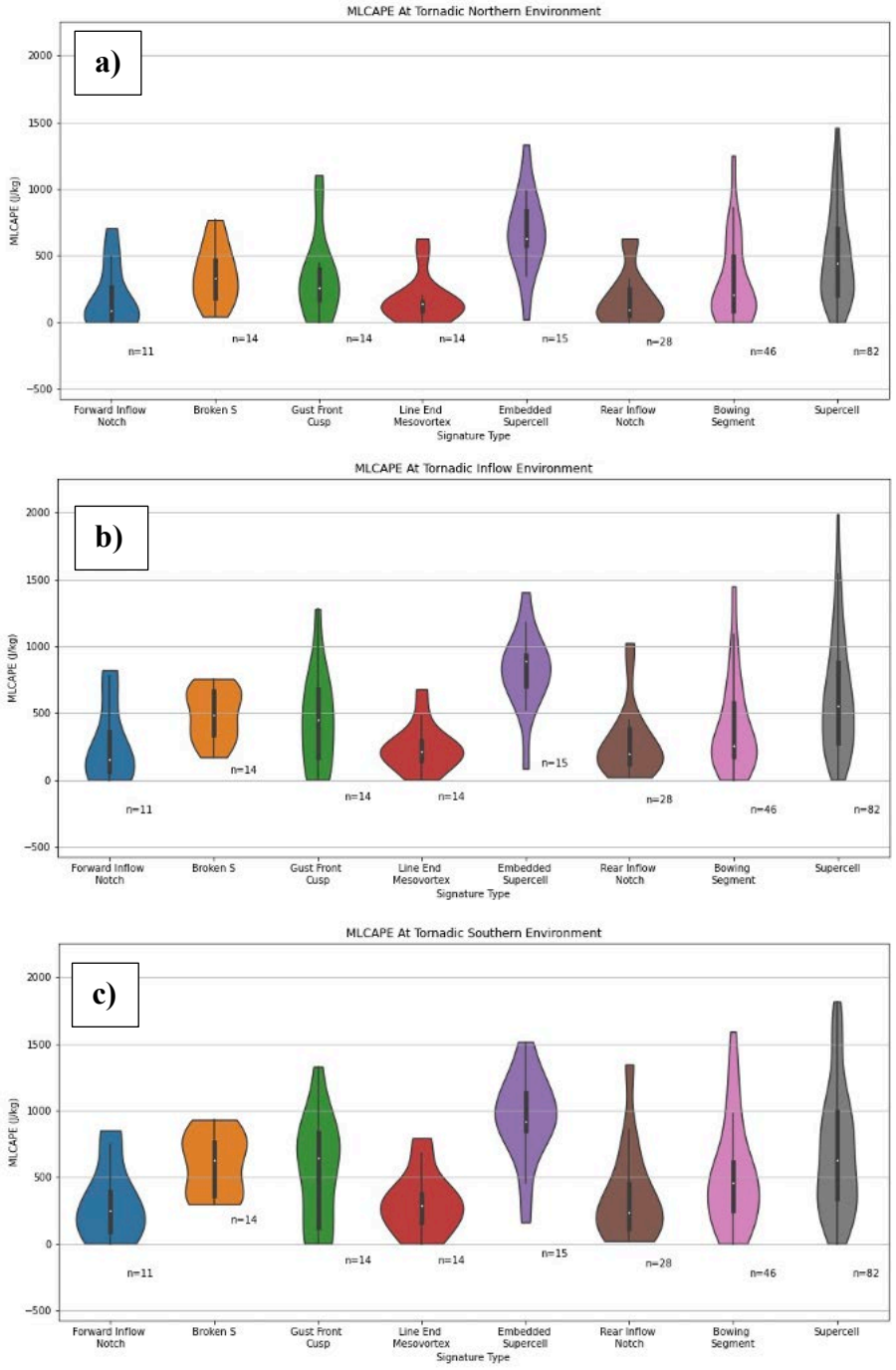

Figure 4.17: MLCAPE at a) northern, b) inflow, and c) southern environmental analysis points at the time of tornadogenesis.

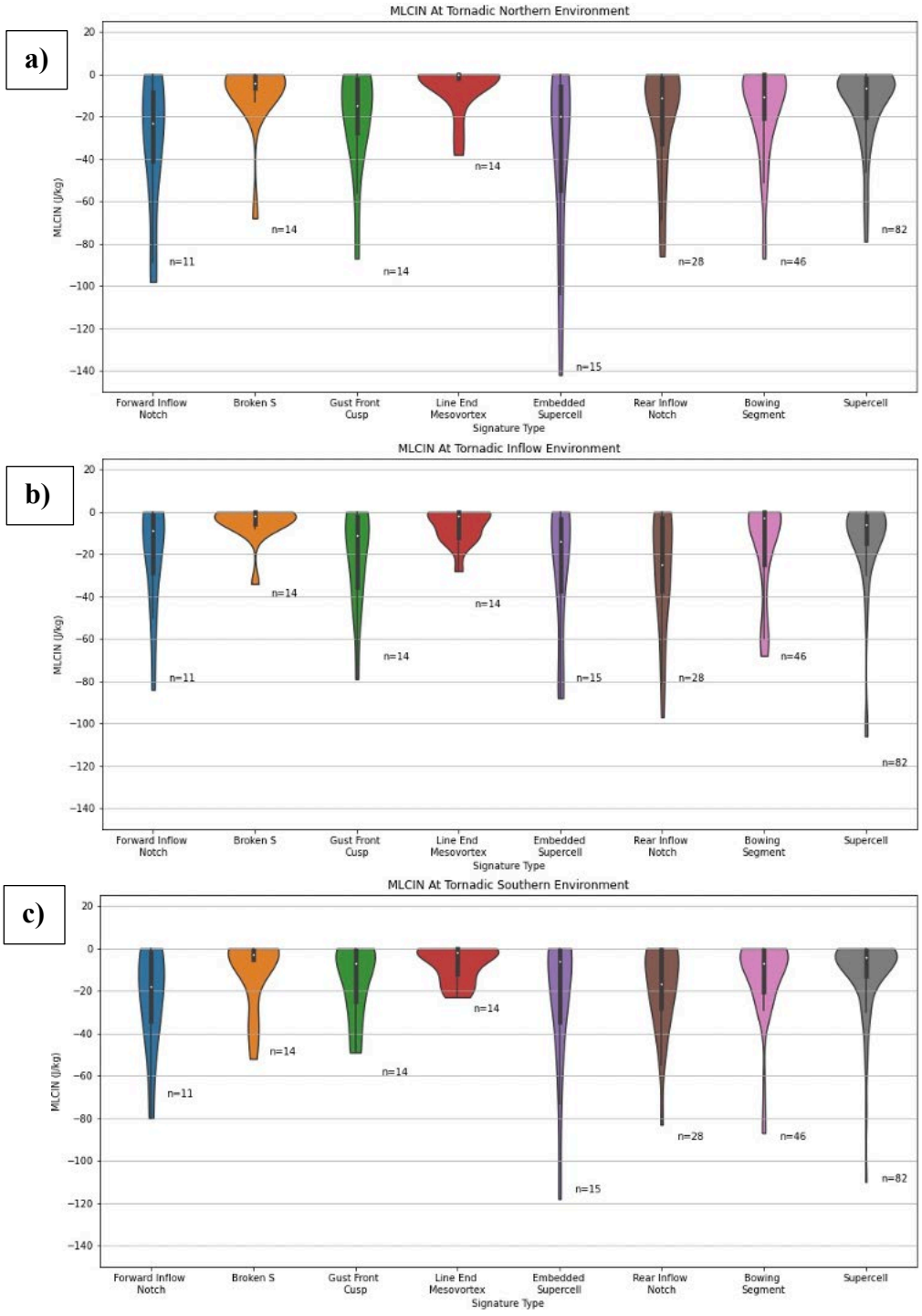

Figure 4.18: MLCIN at a) northern, b) inflow, and c) southern environmental analysis points at the time of tornadogenesis.

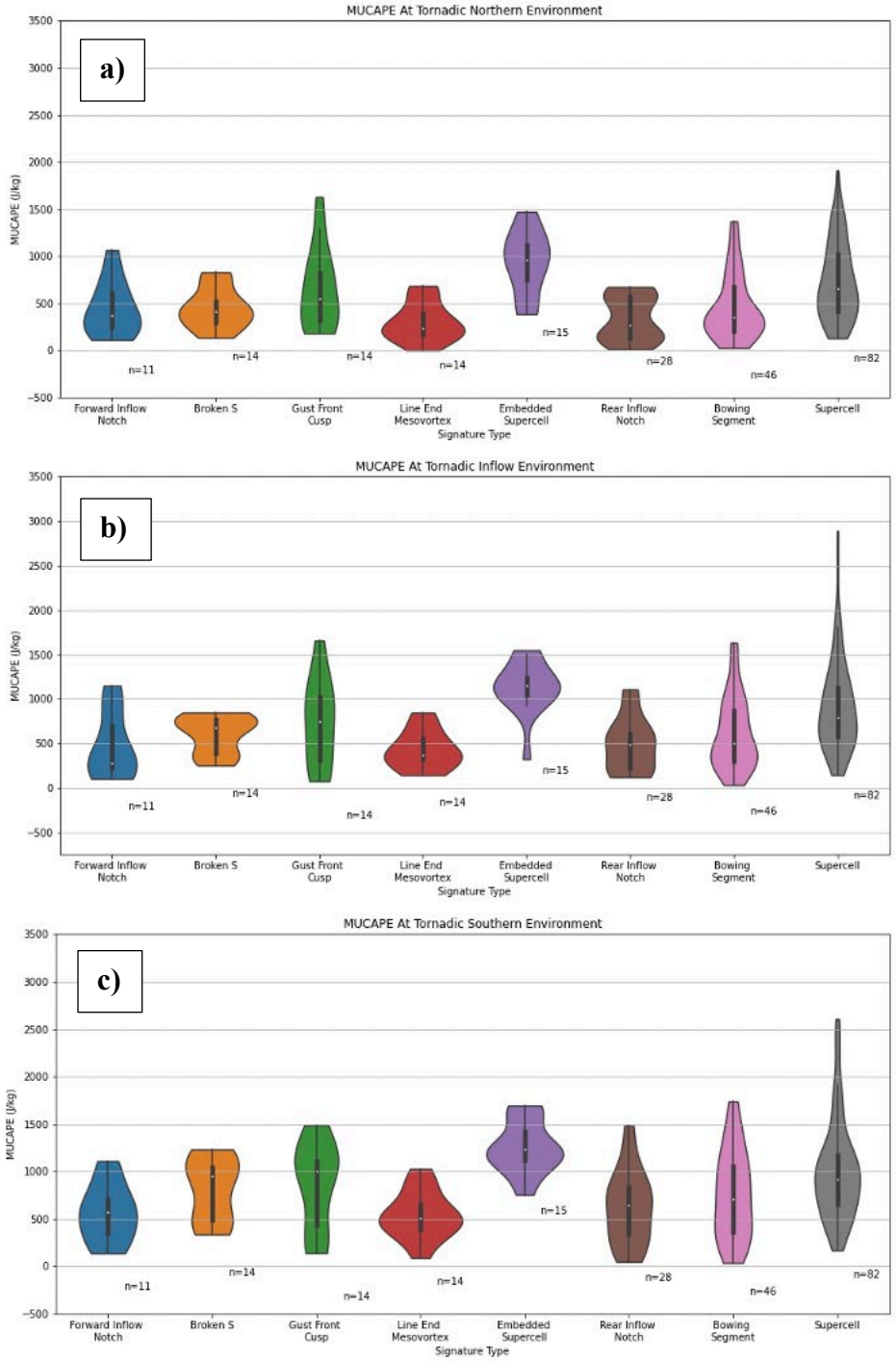

Figure 4.19: MUCAPE at a) northern, b) inflow, and c) southern environmental analysis points at the time of tornadogenesis.

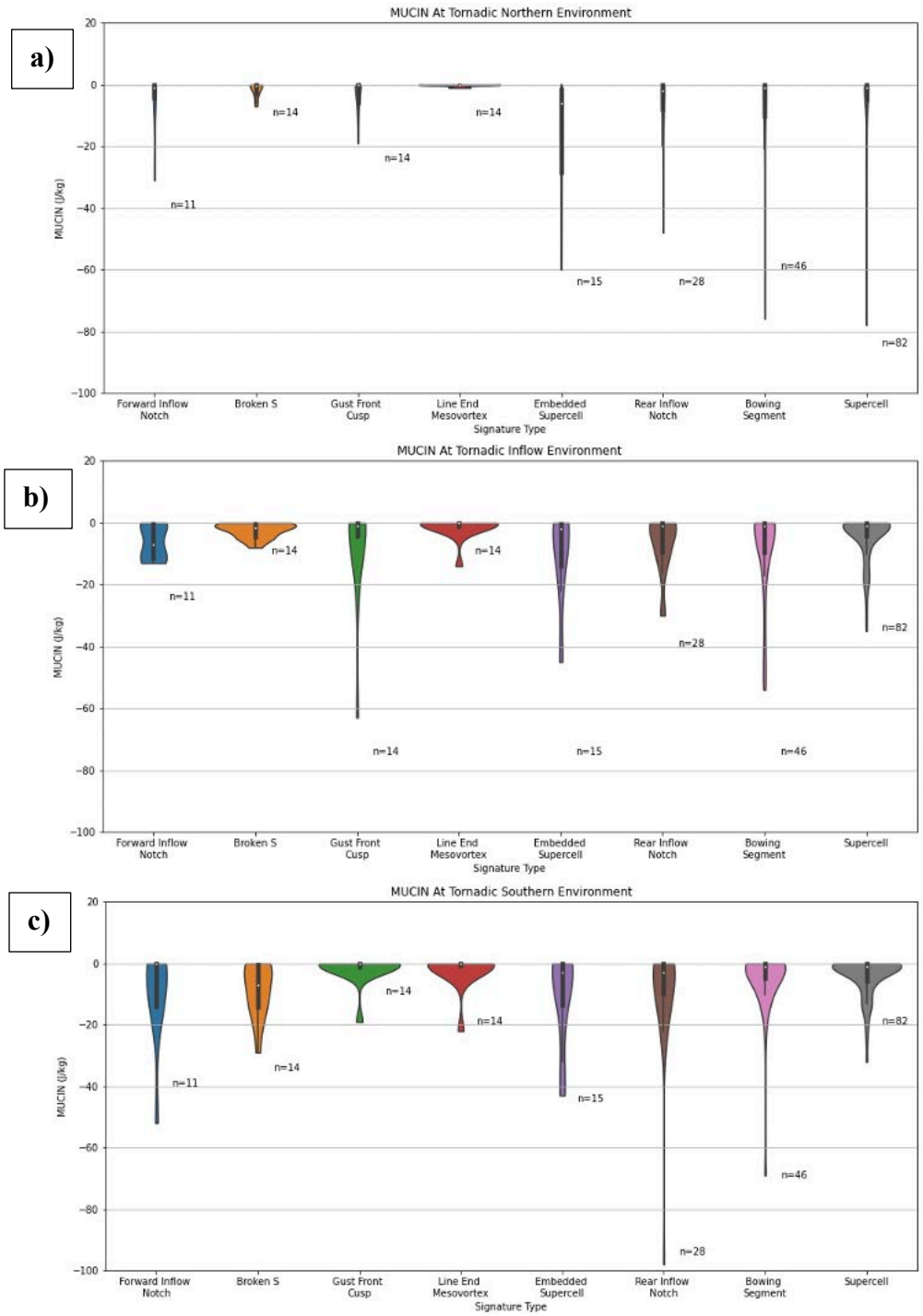

Figure 4.20: MUCIN at a) northern, b) inflow, and c) southern environmental analysis points at the time of tornadogenesis.

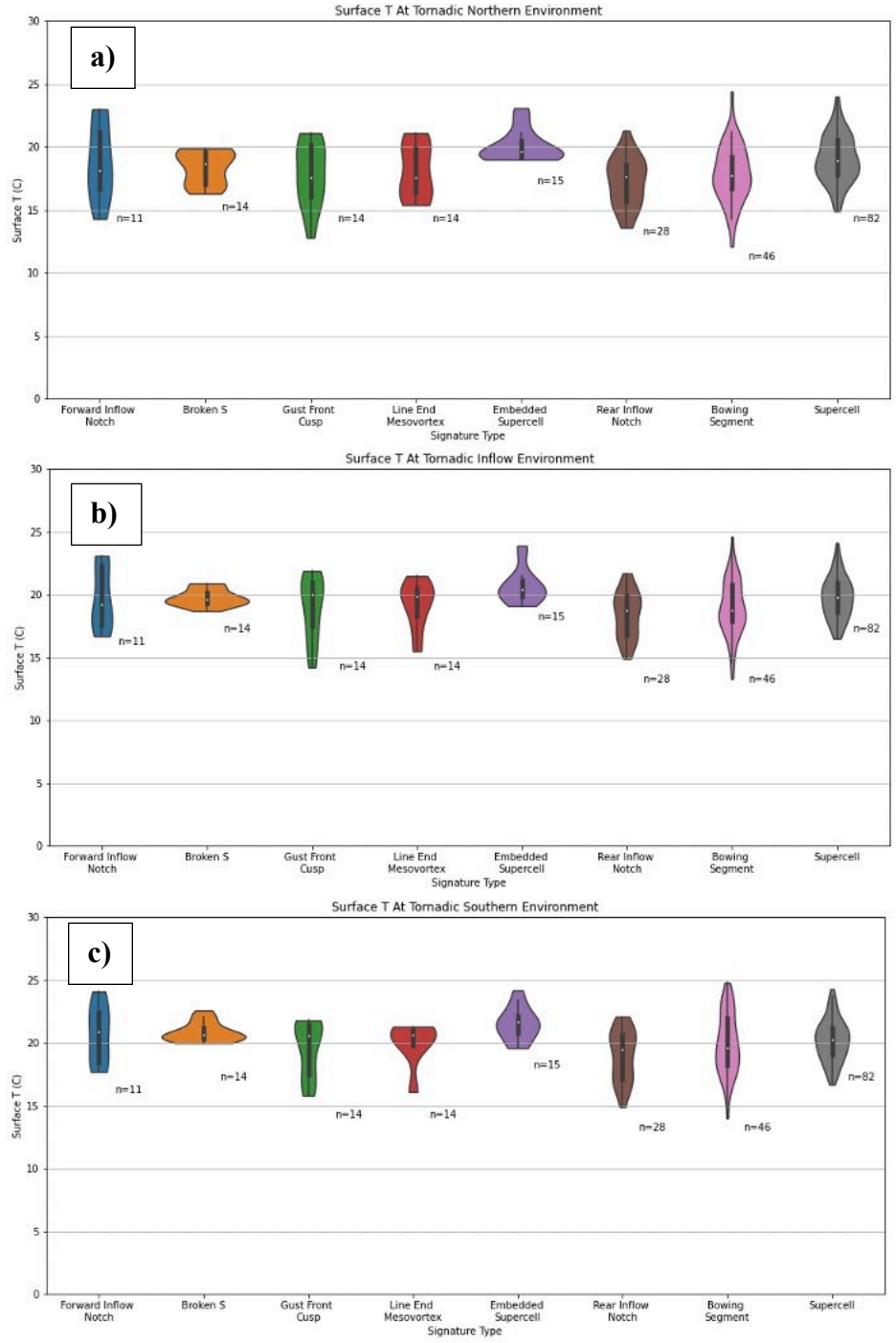

Figure 4.21: Surface temperature (in degrees Celsius) at a) northern, b) inflow, and c) southern environmental analysis points at the time of tornadogenesis.

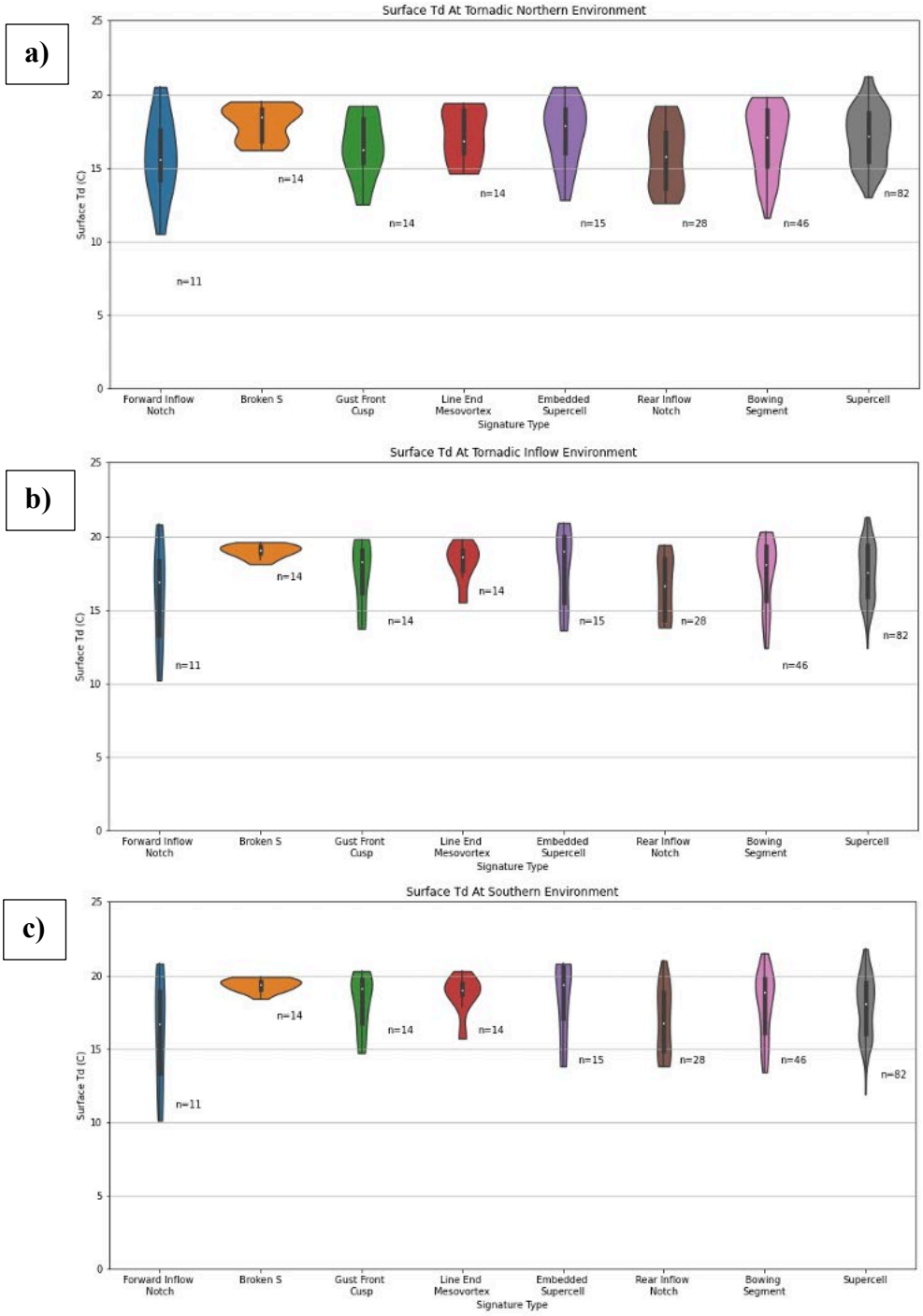

Figure 4.22: Surface dewpoint temperature (in degrees Celsius) at a) northern, b) inflow, and c) southern environmental analysis points at the time of tornadogenesis.

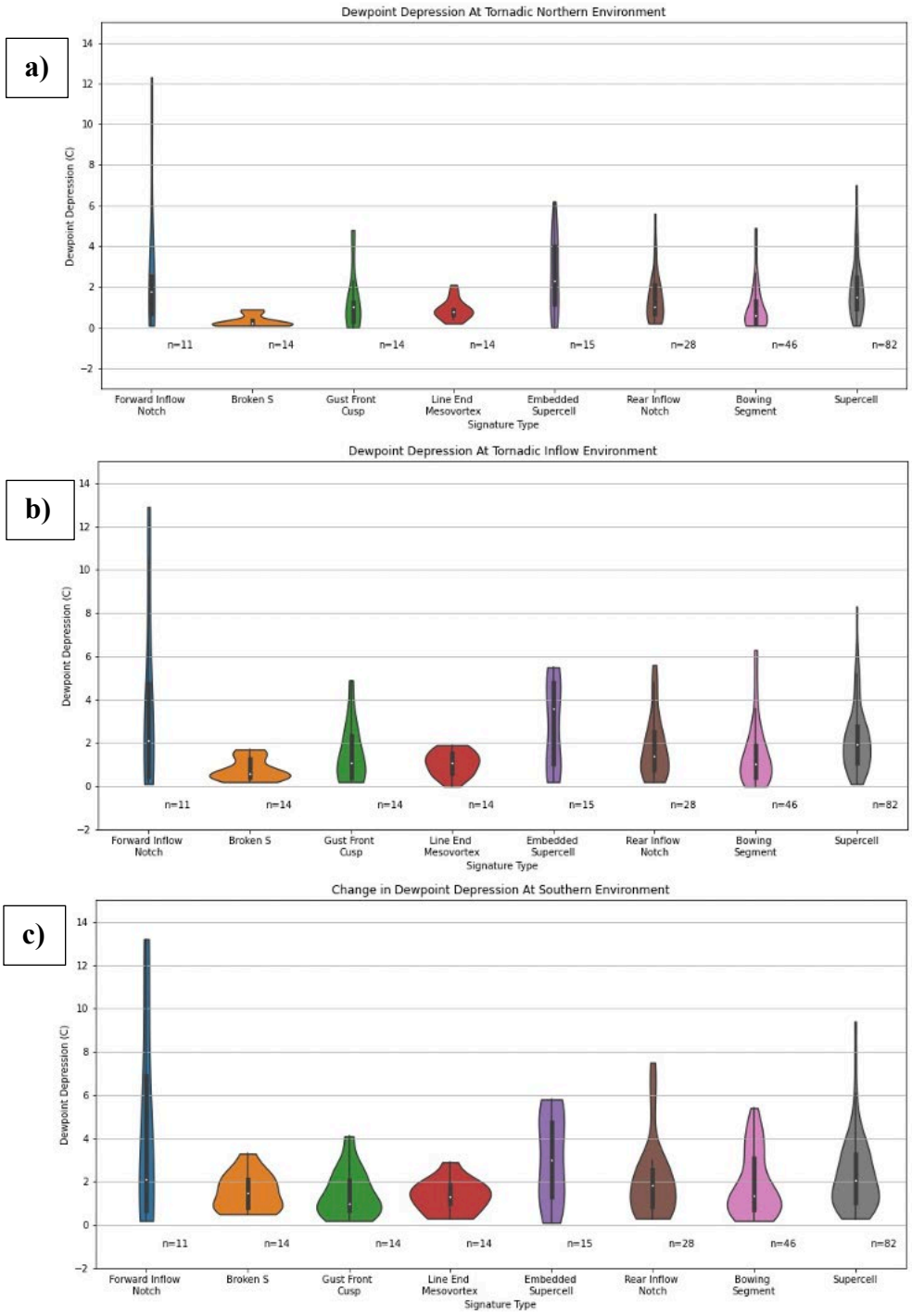

Figure 4.23: Dewpoint depression (in degrees Celsius) at a) northern, b) inflow, and c) southern environmental analysis points at the time of tornadogenesis.

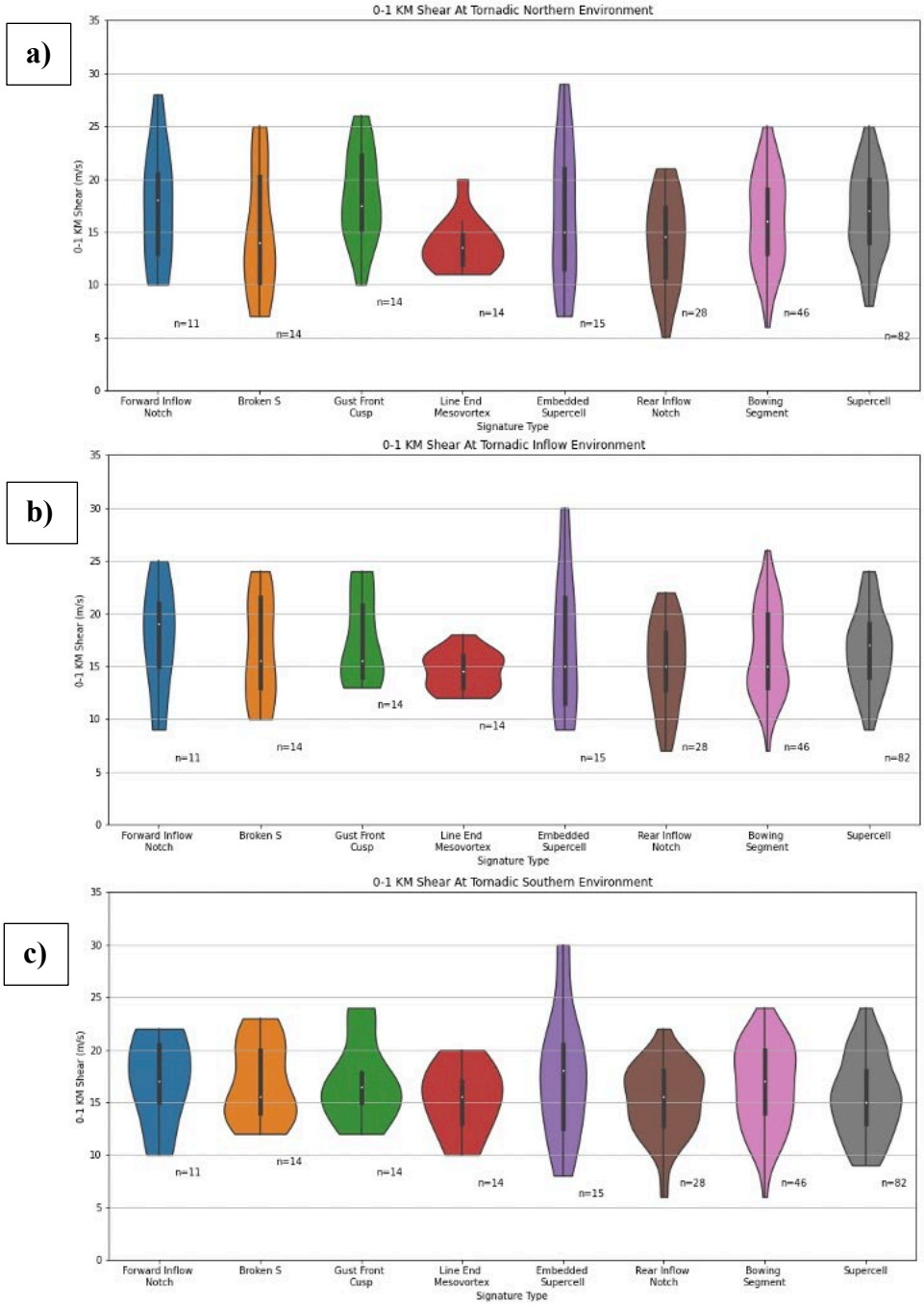

Figure 4.24: 0-1 km wind shear at a) northern, b) inflow, and c) southern environmental analysis points at the time of tornadogenesis.

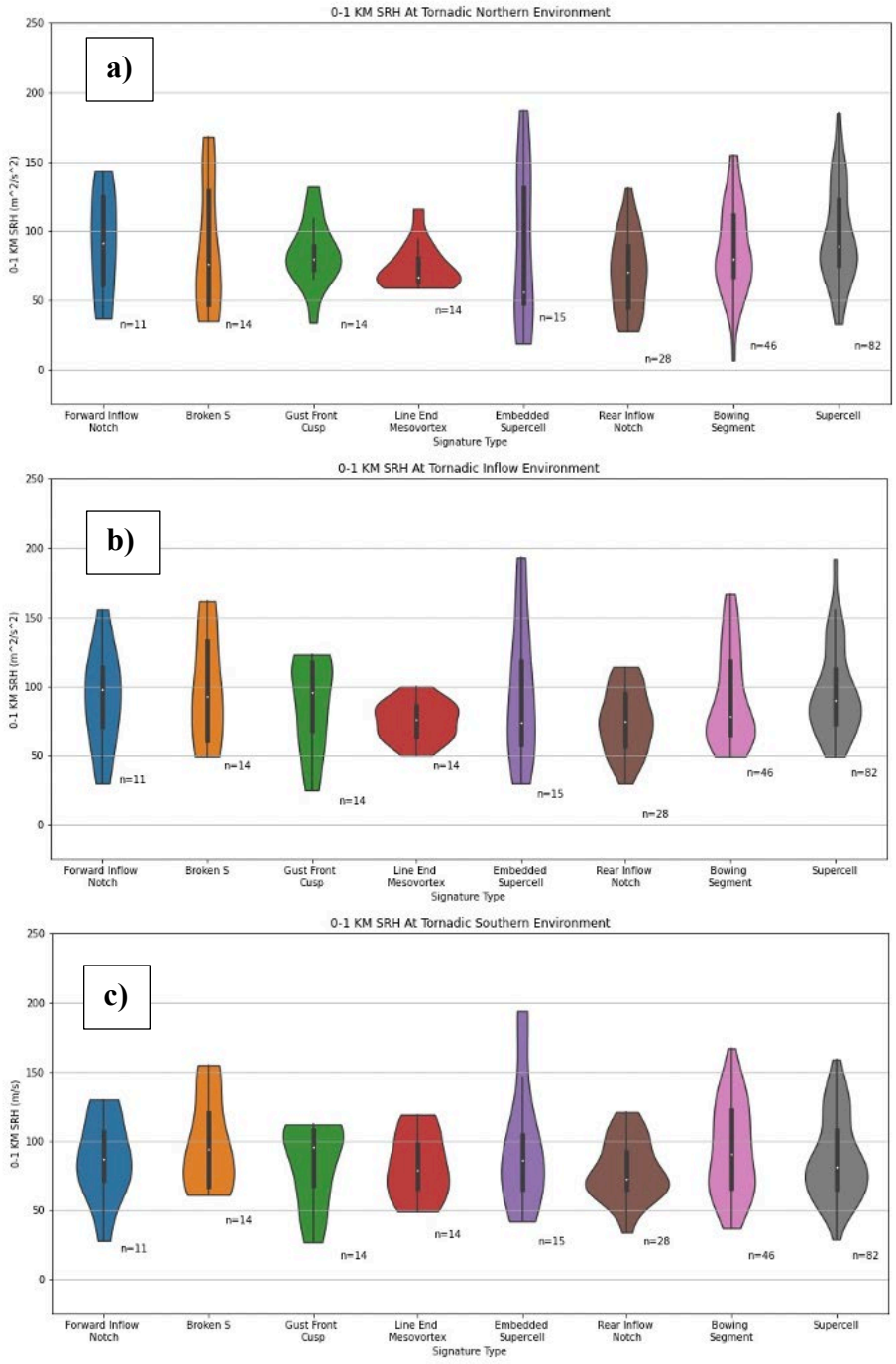

Figure 4.25: 0-1 km storm relative helicity (SRH) at a) northern, b) inflow, and c) southern environmental analysis points at the time of tornadogenesis.

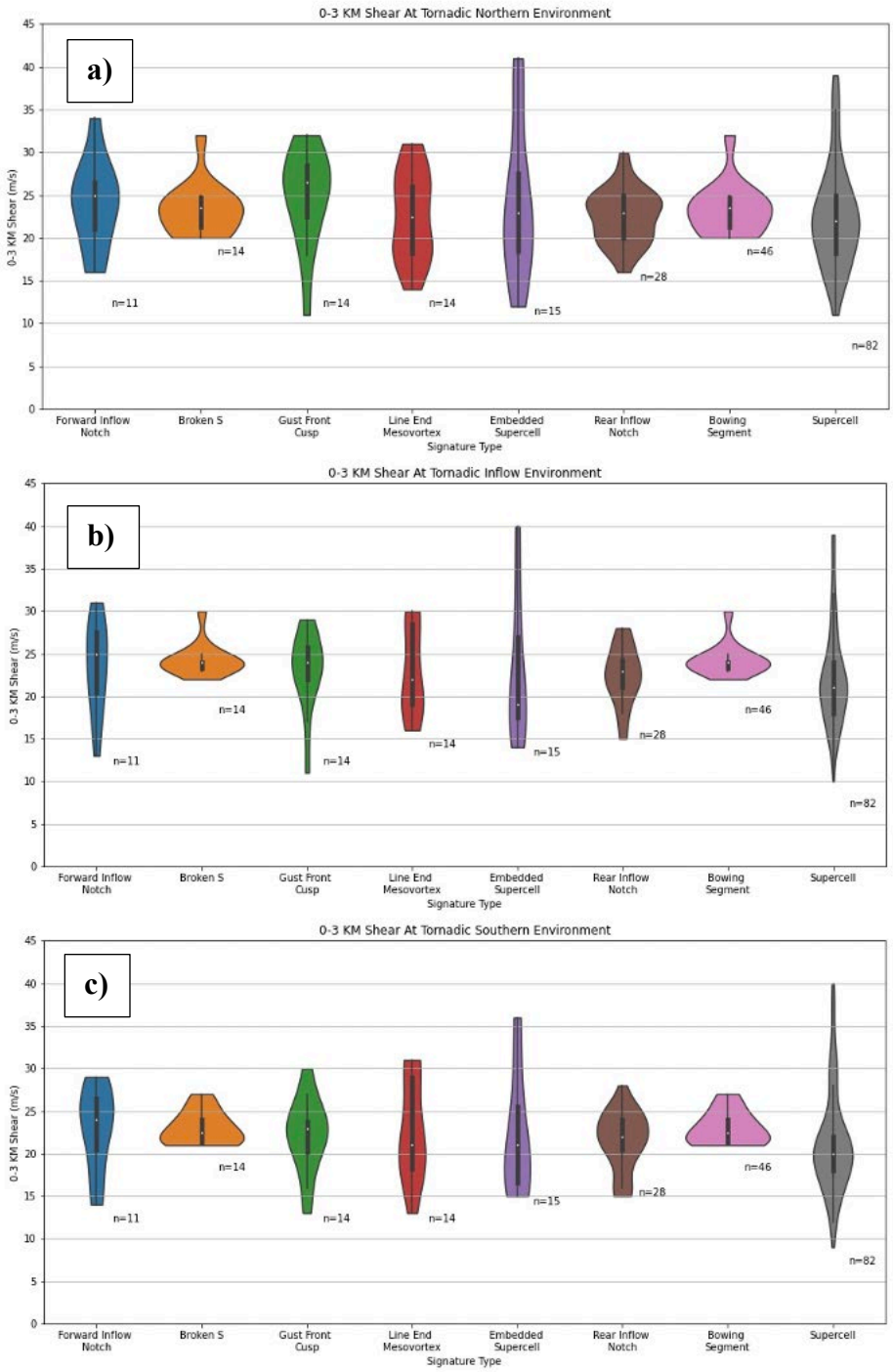

Figure 4.26: 0-3 km wind shear at a) northern, b) inflow, and c) southern environmental analysis points at the time of tornadogenesis.

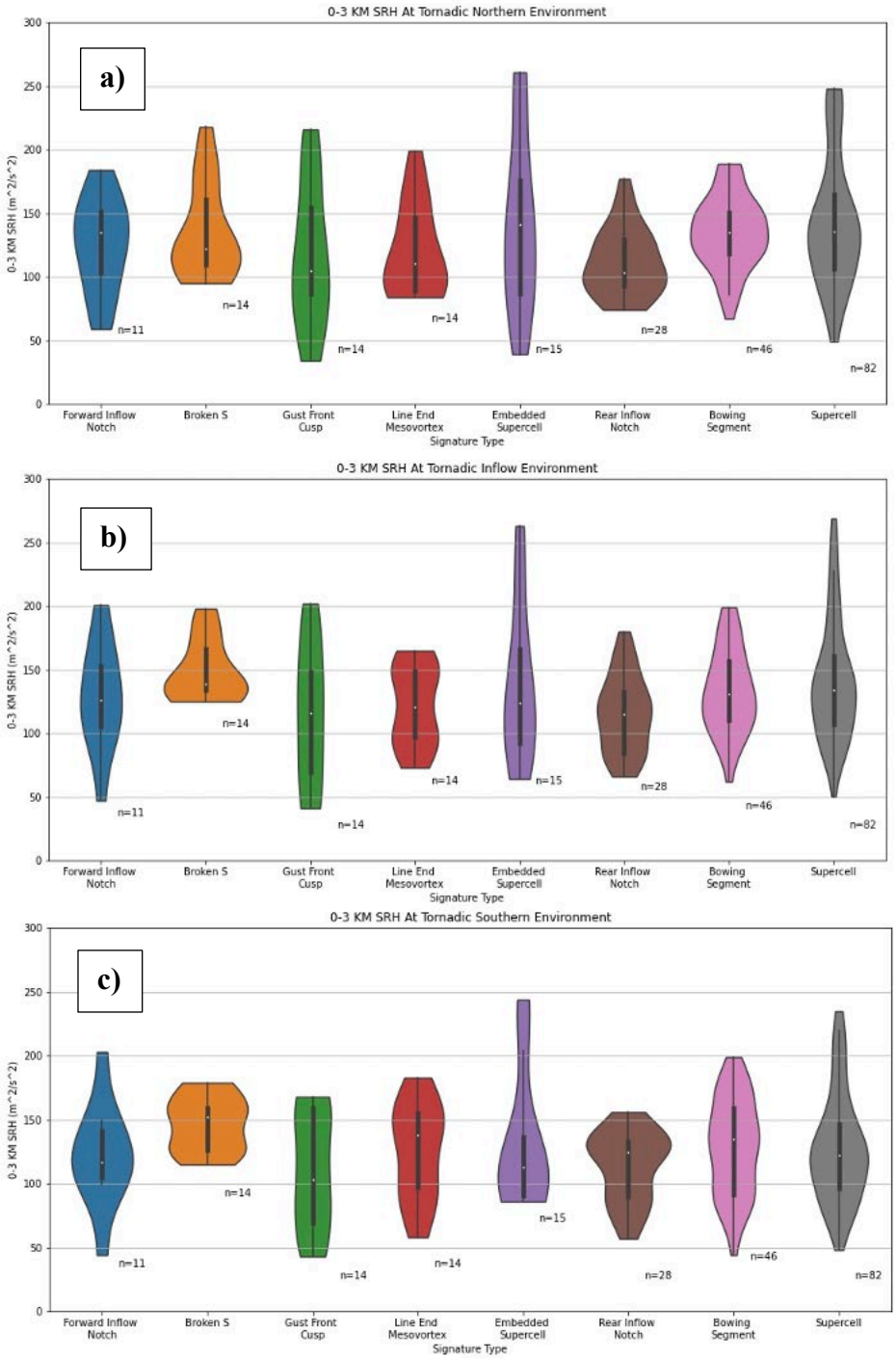

Figure 4.27: 0-3 km storm relative helicity (SRH) at a) northern, b) inflow, and c) southern environmental analysis points at the time of tornadogenesis.

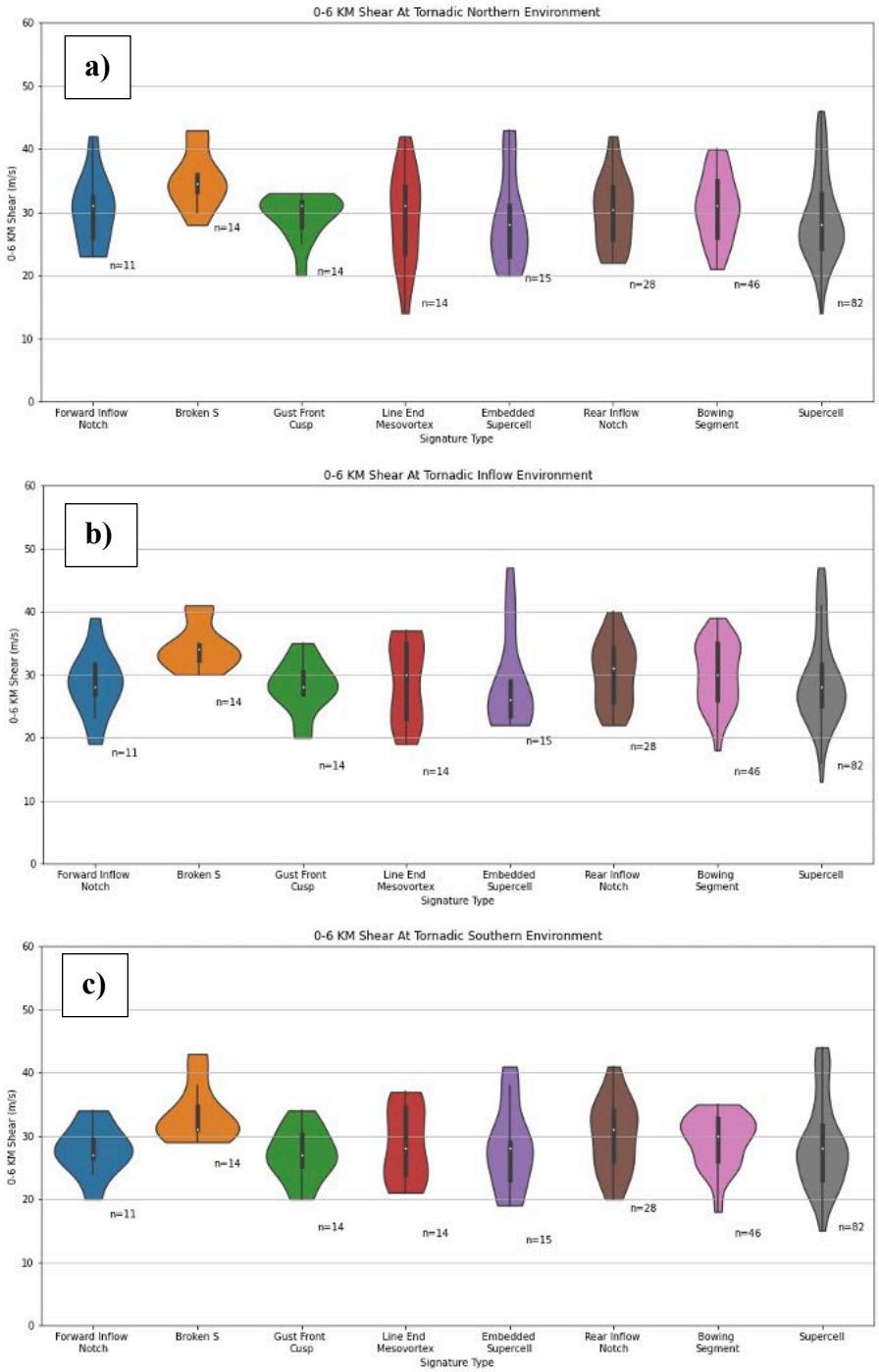

Figure 4.28: 0-6 km wind shear at a) northern, b) inflow, and c) southern environmental analysis points at the time of tornadogenesis.

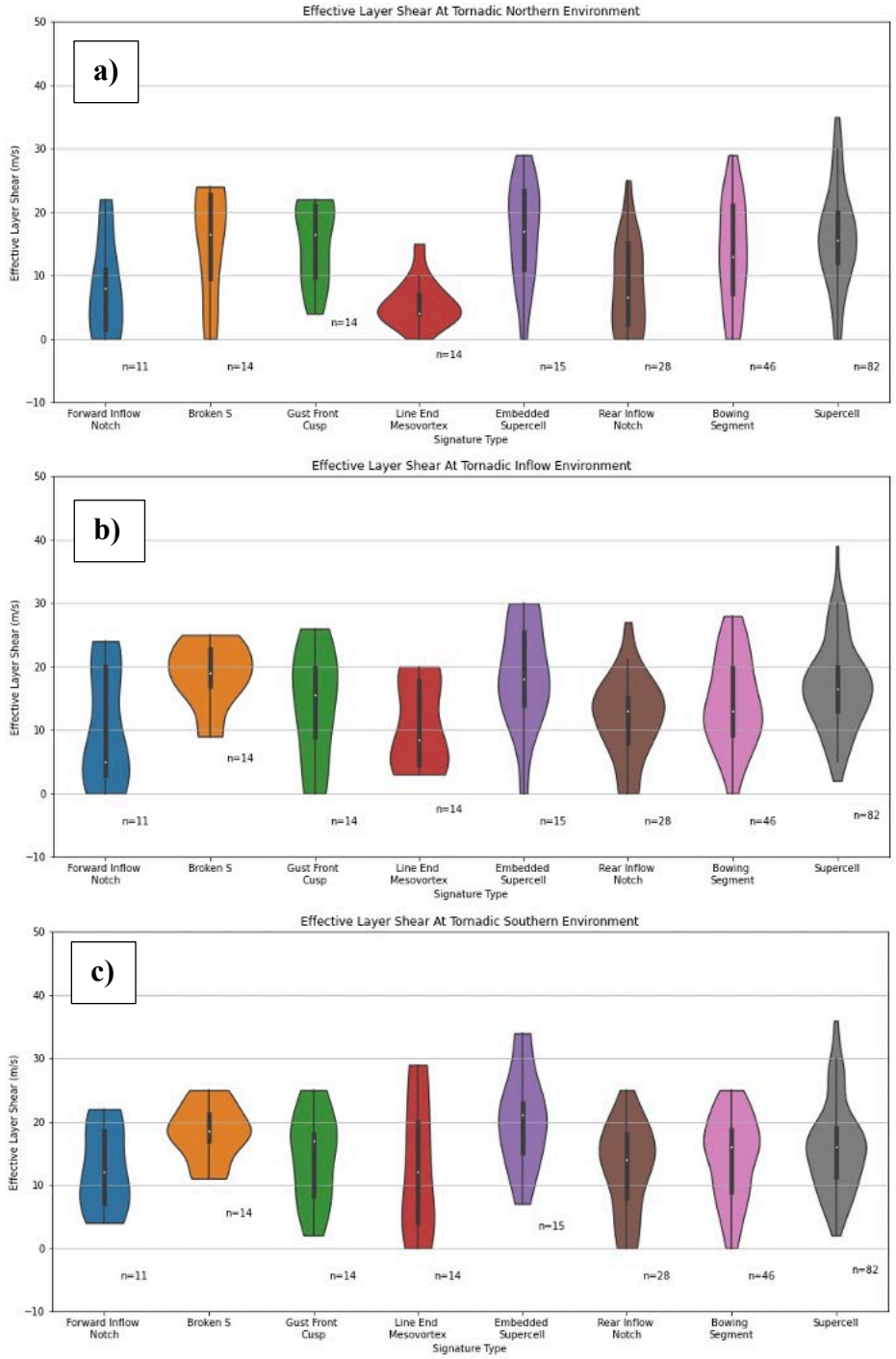

Figure 4.29: Effective layer wind shear at a) northern, b) inflow, and c) southern environmental analysis points at the time of tornadogenesis.

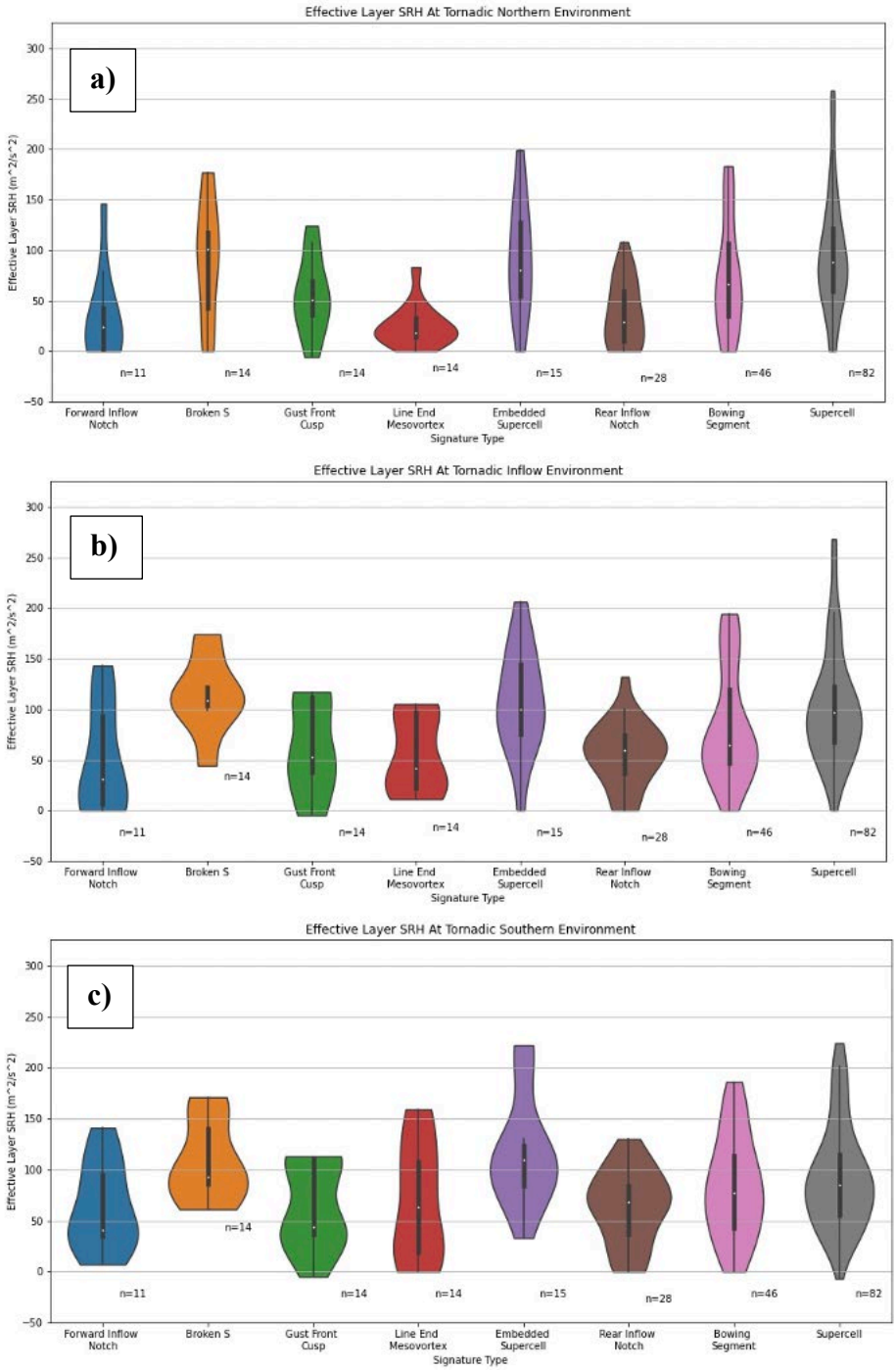

Figure 4.30: Effective layer storm relative helicity (SRH) at a) northern, b) inflow, and c) southern environmental analysis points at the time of tornadogenesis.

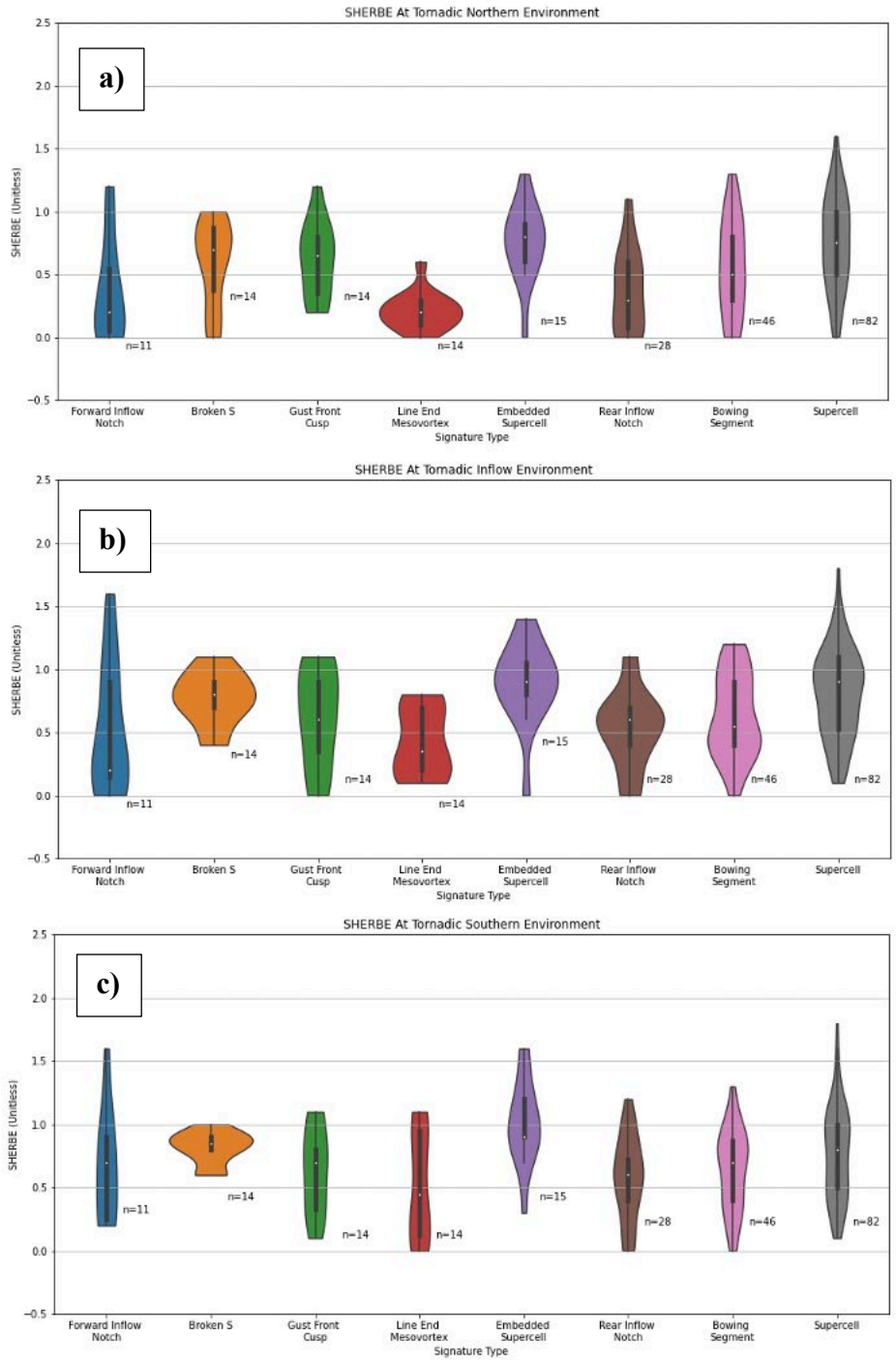

Figure 4.31: Severe hazards in environments with reduced buoyancy, effective shear variant (SHERBE) at a) northern, b) inflow, and c) southern environmental analysis points at the time of tornadogenesis.

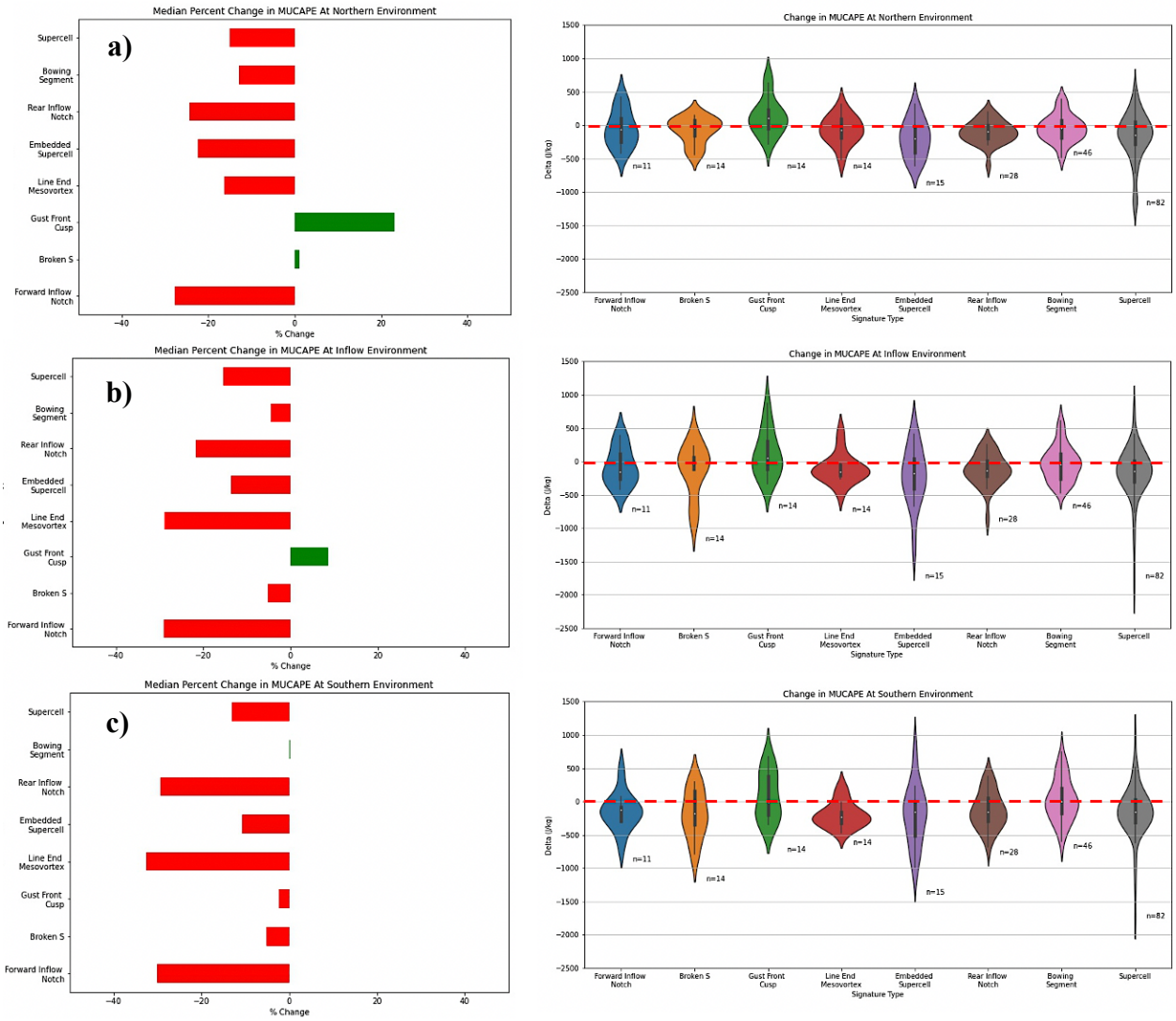

Figure 4.32: Median percent change (left) and raw deltas [(T-0)-(T-1)] (right) of MUCAPE at a) northern, b) inflow, and c) southern environmental analysis points. On percent change plot: red bars represent negative percent changes; green bars represent positive percent changes. On deltas plot: dotted red line denotes "0" line with sample sizes annotated for each reflectivity signature.

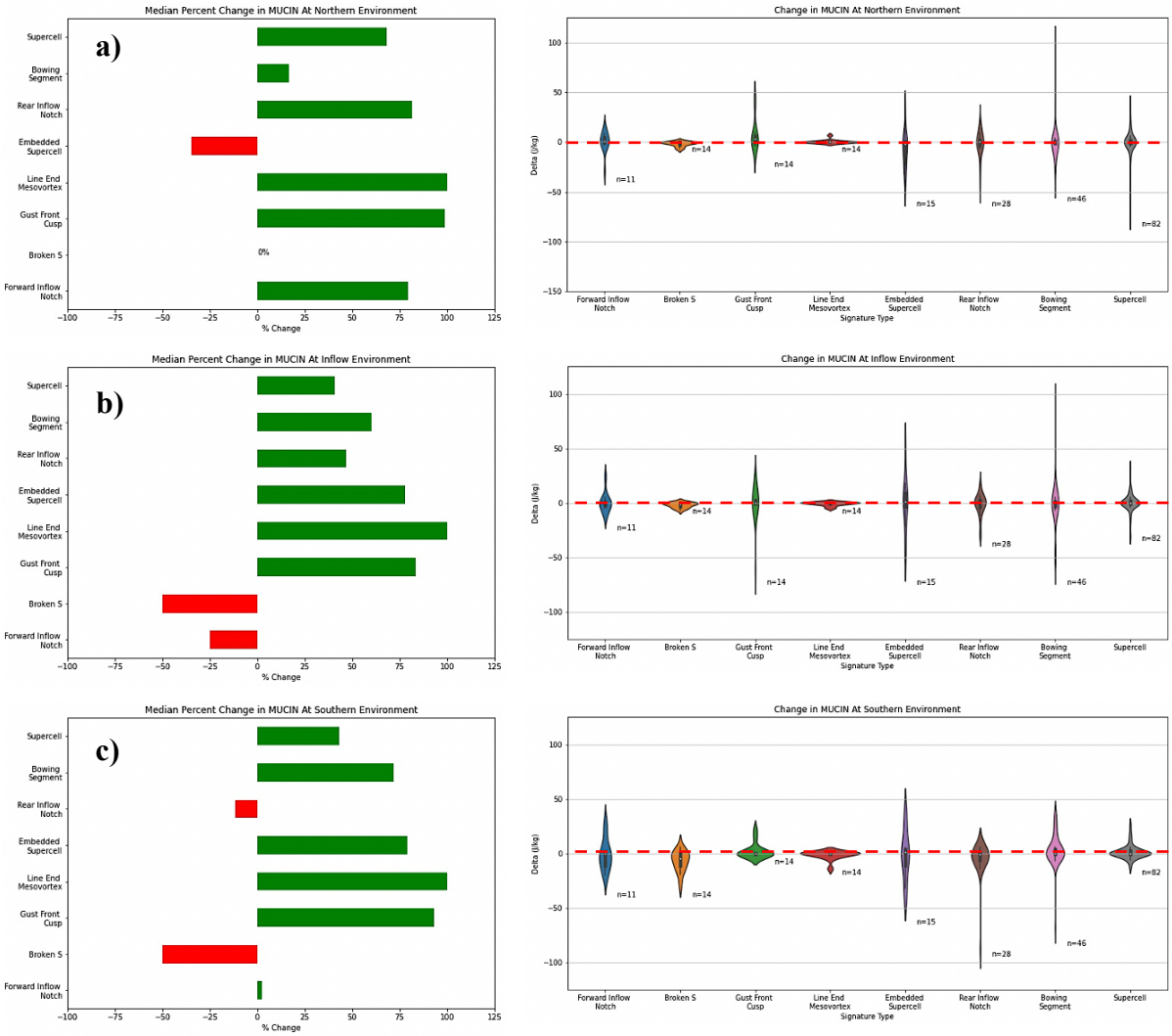

Figure 4.33: Median percent change (left) and raw deltas [(T-0)-(T-1)] (right) of MUCIN at a) northern, b) inflow, and c) southern environmental analysis points. On percent change plot: red bars represent negative percent changes; green bars represent positive percent changes. On deltas plot: dotted red line denotes "0" line with sample sizes annotated for each reflectivity signature.

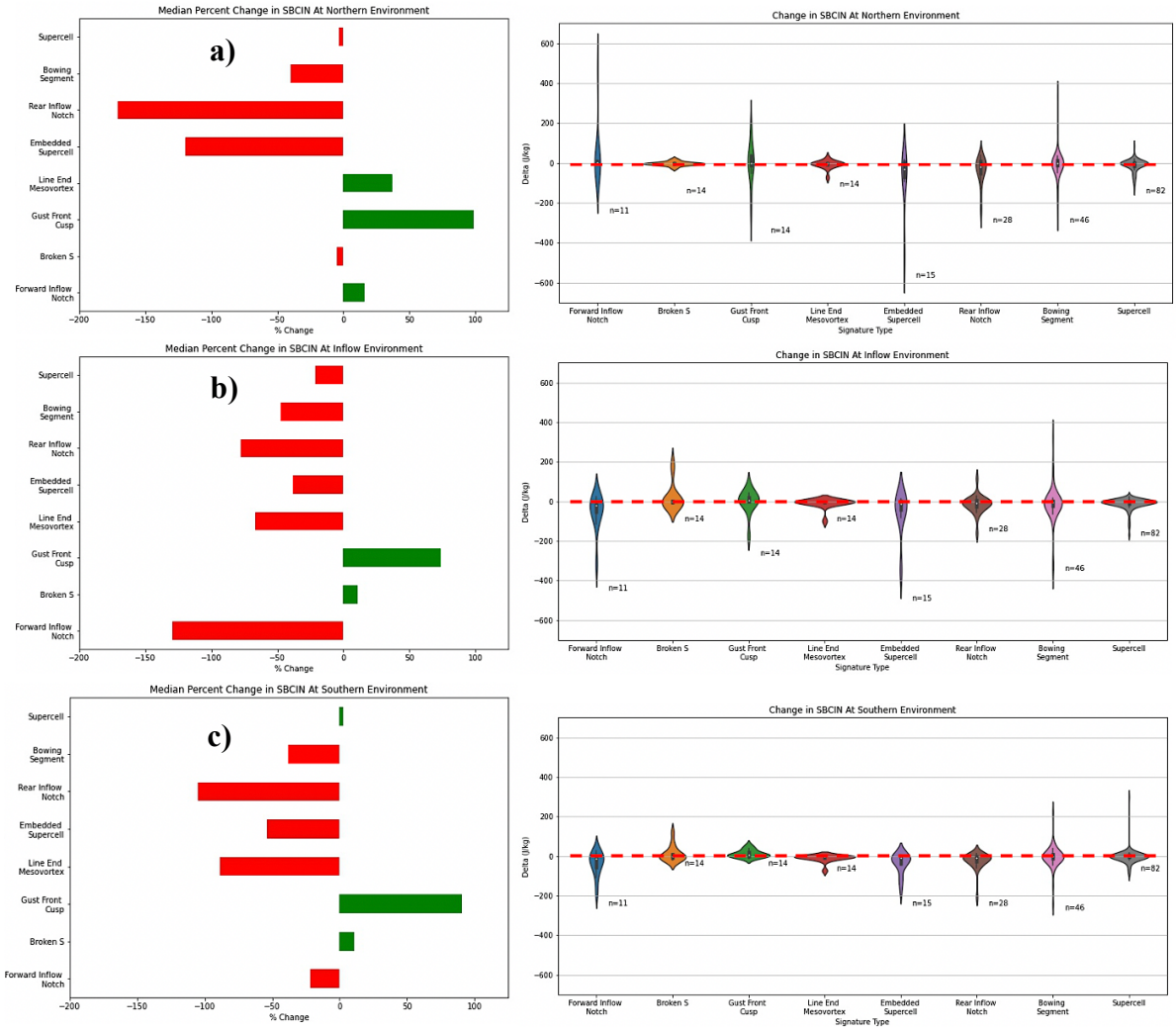

Figure 4.34: Median percent change (left) and raw deltas [(T-0)-(T-1)] (right) of SBCIN at a) northern, b) inflow, and c) southern environmental analysis points. On percent change plot: red bars represent negative percent changes; green bars represent positive percent changes. On deltas plot: dotted red line denotes "0" line with sample sizes annotated for each reflectivity signature.

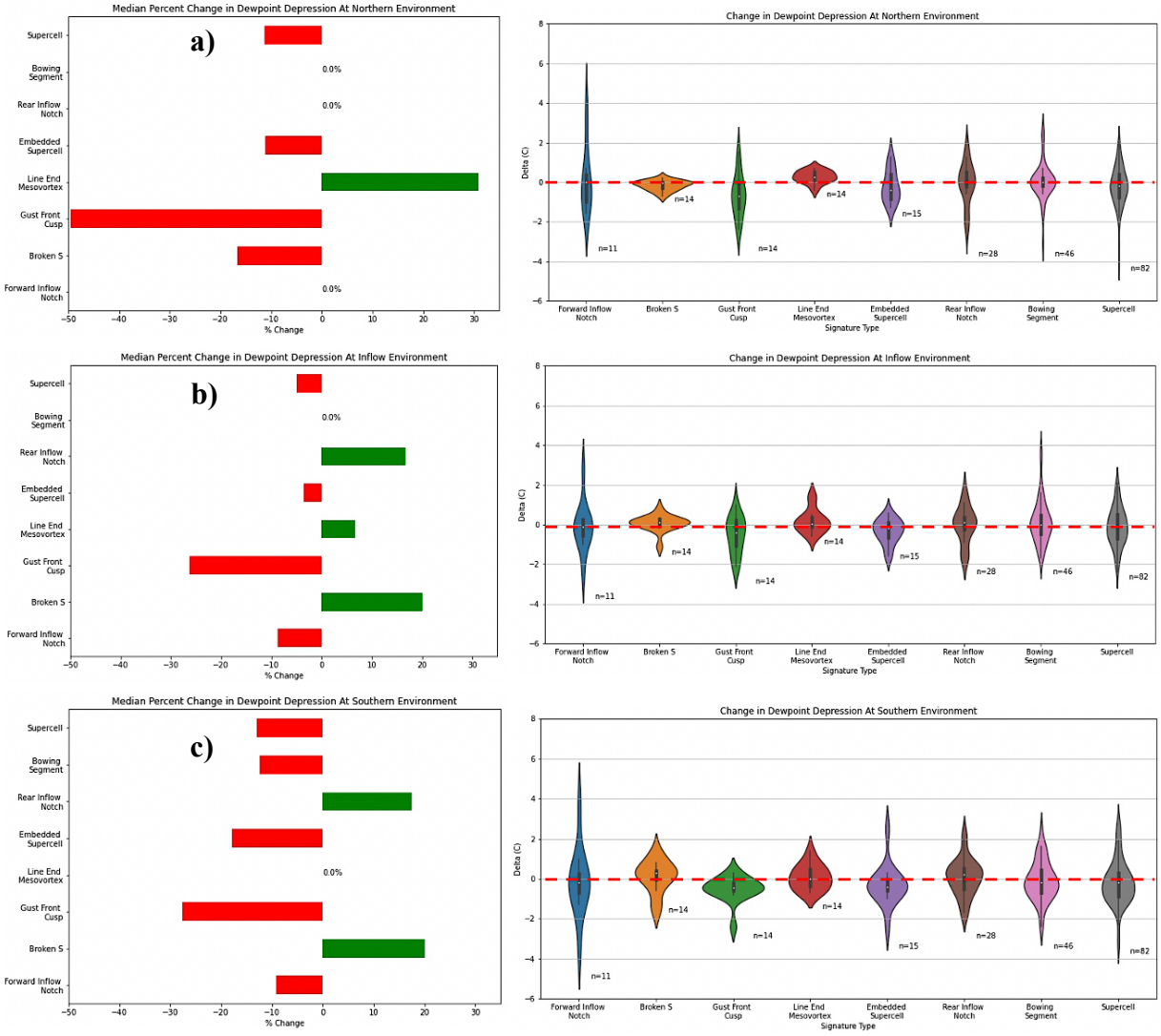

Figure 4.35: Median percent change (left) and raw deltas [(T-0)-(T-1)] (right) of dewpoint depression at a) northern, b) inflow, and c) southern environmental analysis points. On percent change plot: red bars represent negative percent changes; green bars represent positive percent changes. On deltas plot: dotted red line denotes "0" line with sample sizes annotated for each reflectivity signature.

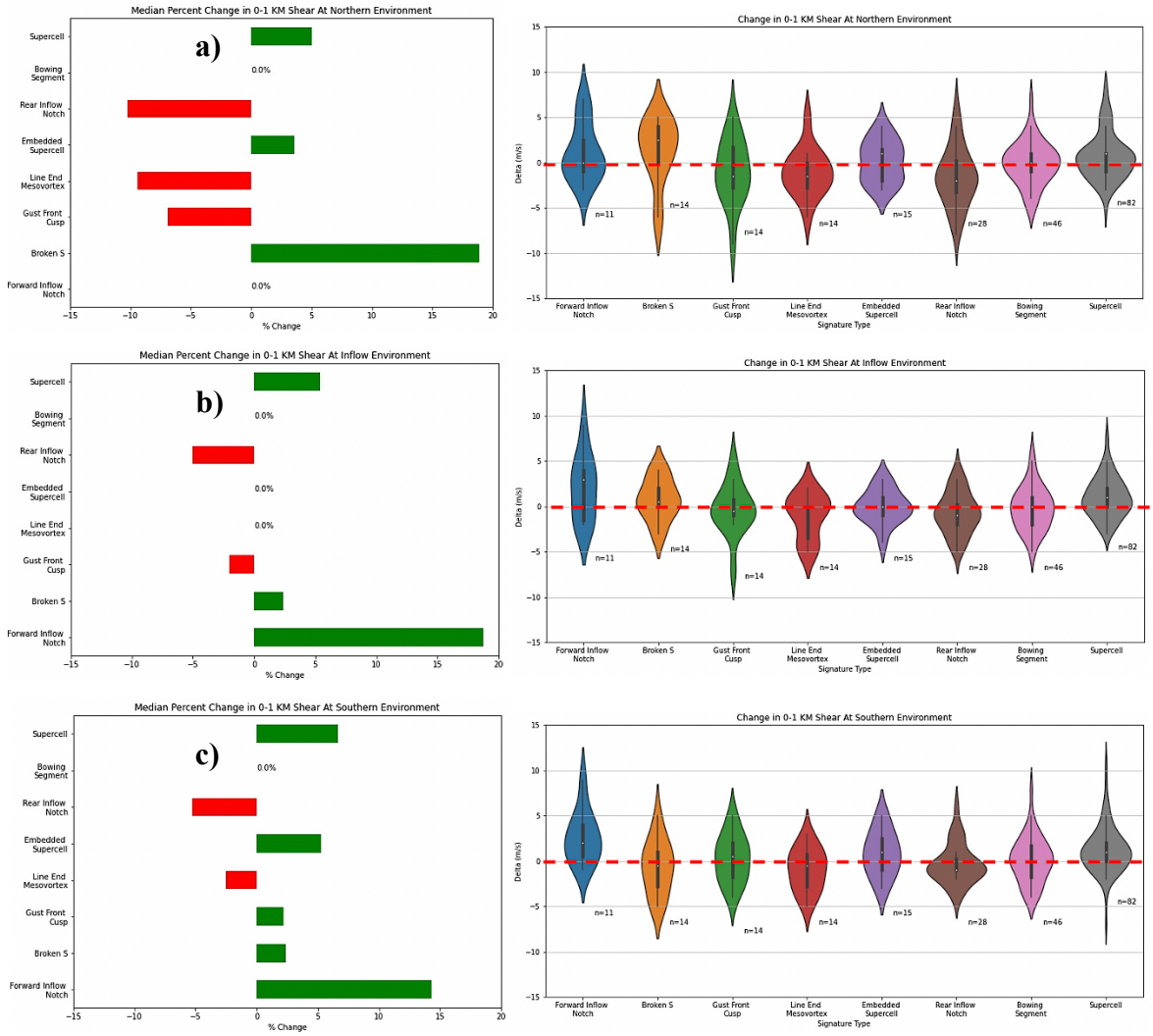

Figure 4.36: Median percent change (left) and raw deltas [(T-0)-(T-1)] (right) of 0-1 km wind shear at a) northern, b) inflow, and c) southern environmental analysis points. On percent change plot: red bars represent negative percent changes; green bars represent positive percent changes. On deltas plot: dotted red line denotes "0" line with sample sizes annotated for each reflectivity signature.

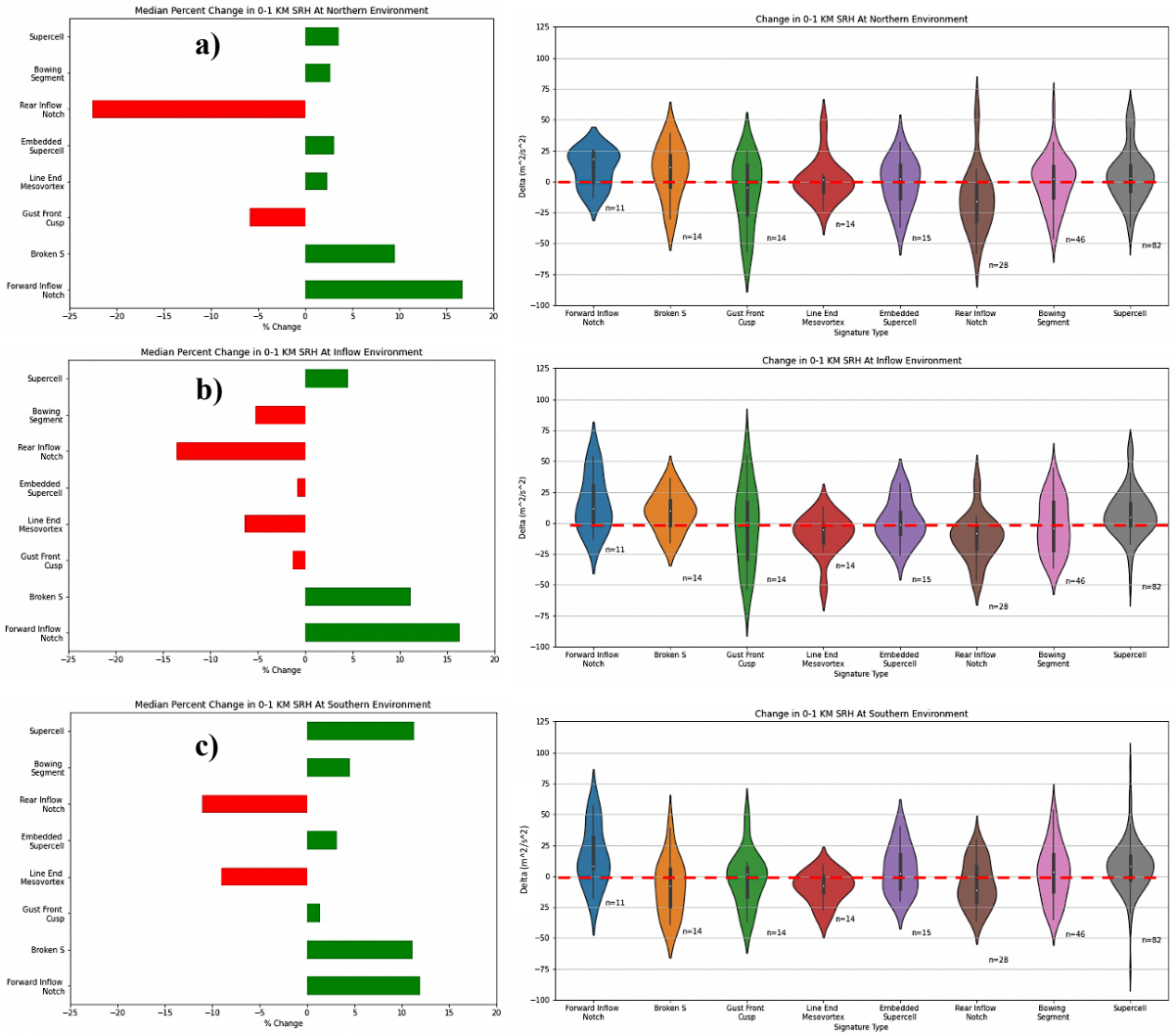

Figure 4.37: Median percent change (left) and raw deltas [(T-0)-(T-1)] (right) of 0-1 km storm relative helicity (SRH) at a) northern, b) inflow, and c) southern environmental analysis points. On percent change plot: red bars represent negative percent changes; green bars represent positive percent changes. On deltas plot: dotted red line denotes "0" line with sample sizes annotated for each reflectivity signature.

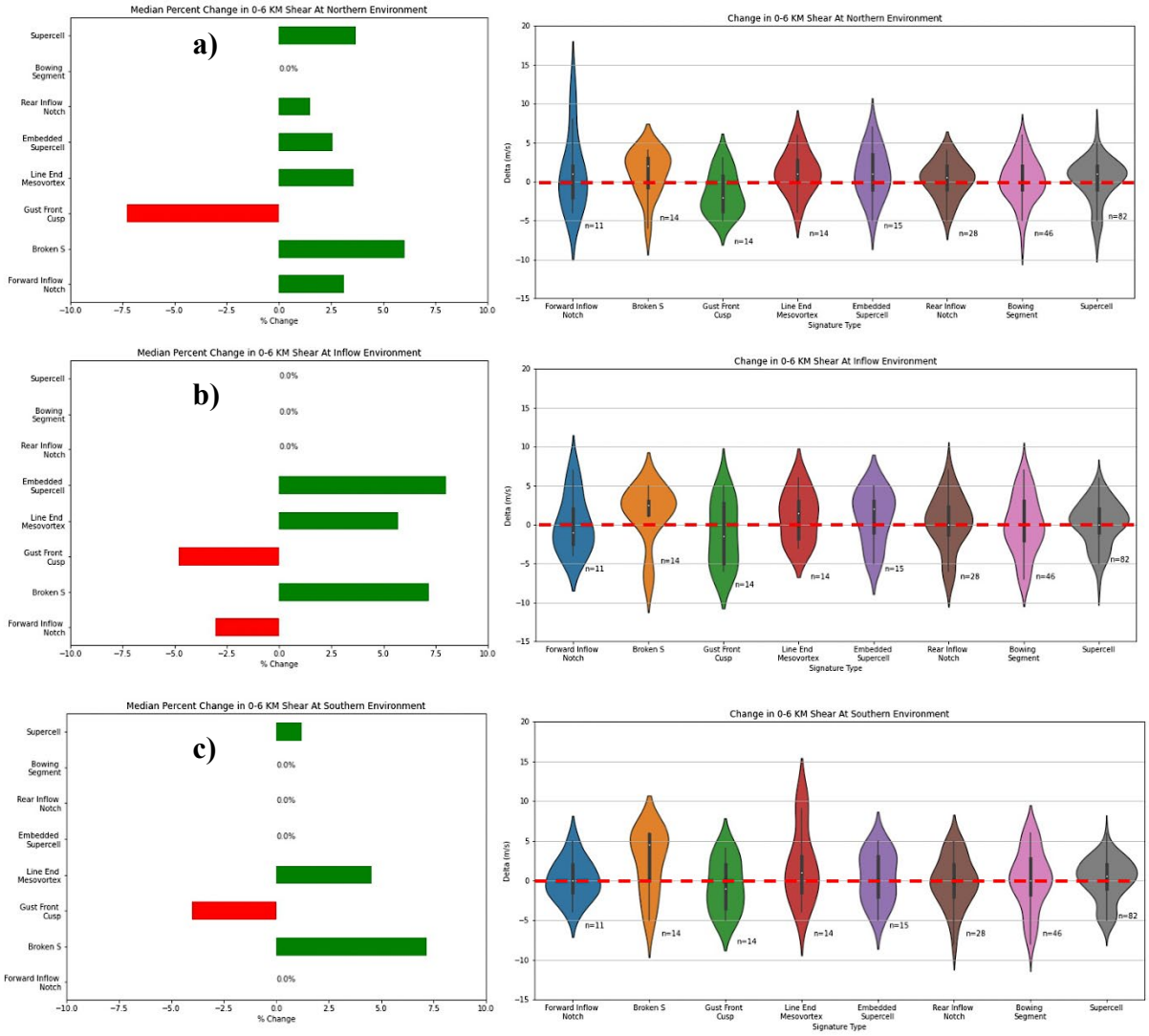

Figure 4.38: Median percent change (left) and raw deltas [(T-0)-(T-1)] (right) of 0-6 km wind shear at a) northern, b) inflow, and c) southern environmental analysis points. On percent change plot: red bars represent negative percent changes; green bars represent positive percent changes. On deltas plot: dotted red line denotes "0" line with sample sizes annotated for each reflectivity signature.

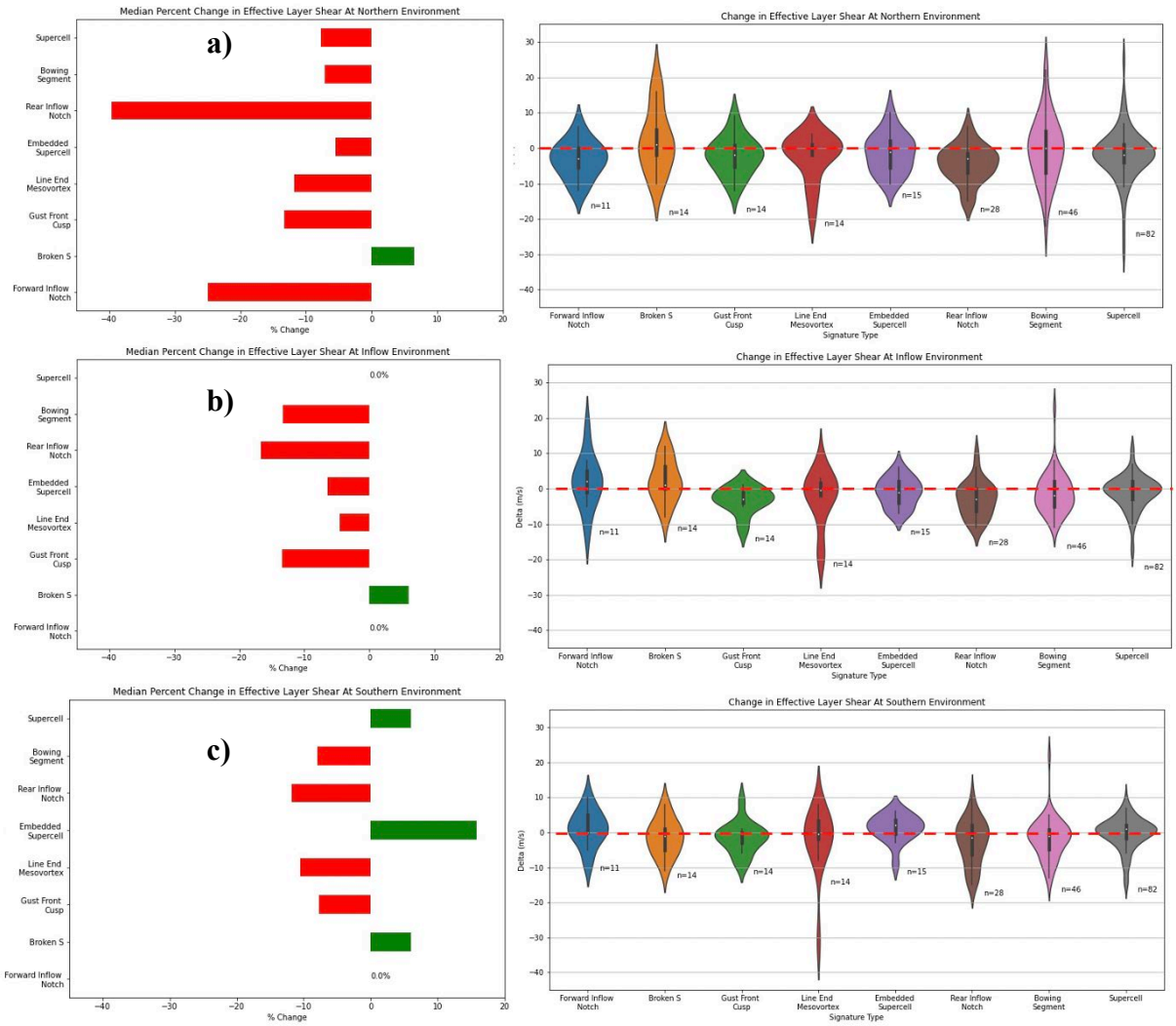

Figure 4.39: Median percent change (left) and raw deltas [(T-0)-(T-1)] (right) of effective layer wind shear at a) northern, b) inflow, and c) southern environmental analysis points. On percent change plot: red bars represent negative percent changes; green bars represent positive percent changes. On deltas plot: dotted red line denotes "0" line with sample sizes annotated for each reflectivity signature.

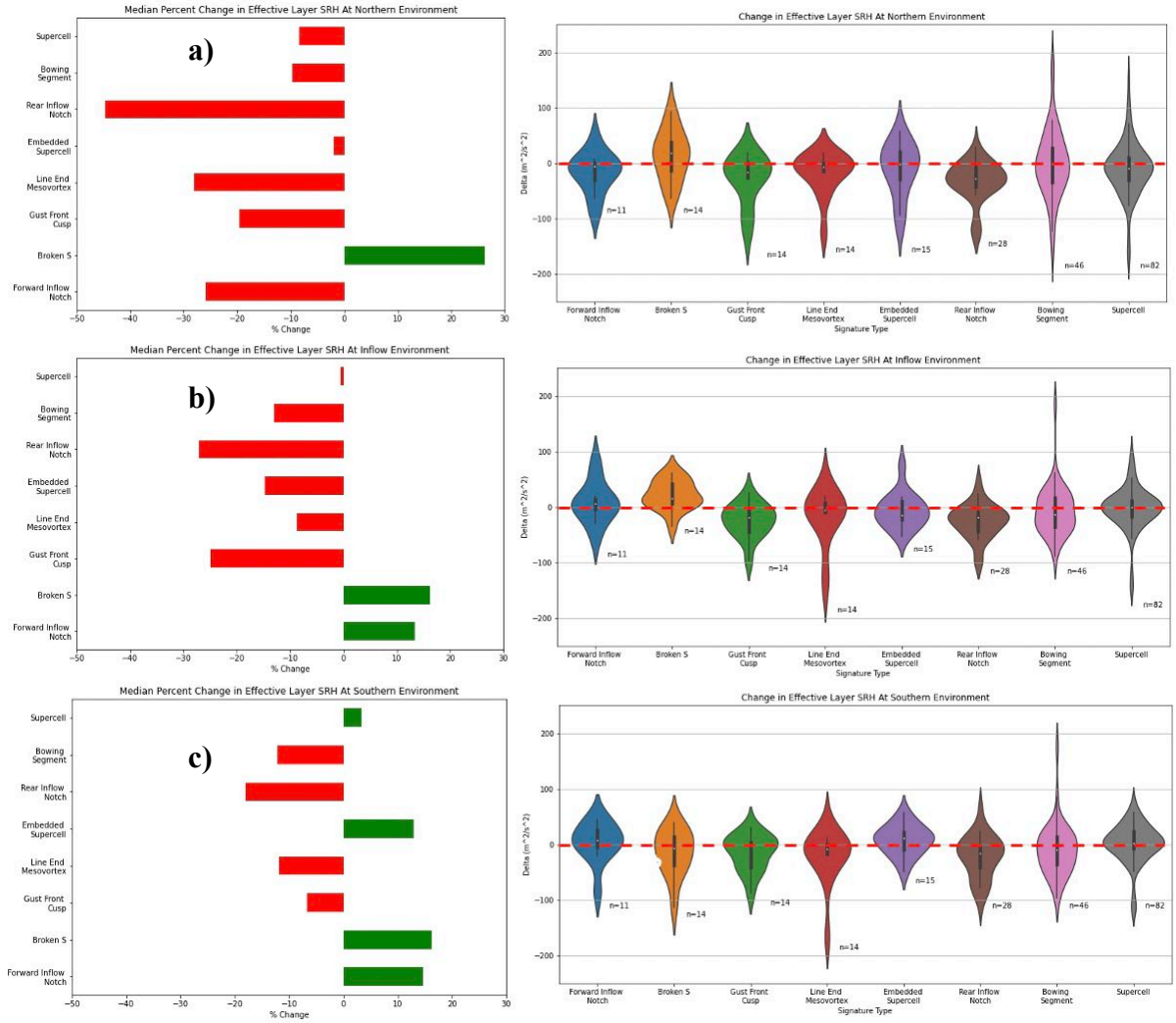

Figure 4.40: Median percent change (left) and raw deltas [(T-0)-(T-1)] (right) of effective layer storm relative helicity (SRH) at a) northern, b) inflow, and c) southern environmental analysis points. On percent change plot: red bars represent negative percent changes; green bars represent positive percent changes. On deltas plot: dotted red line denotes "0" line with sample sizes annotated for each reflectivity signature.

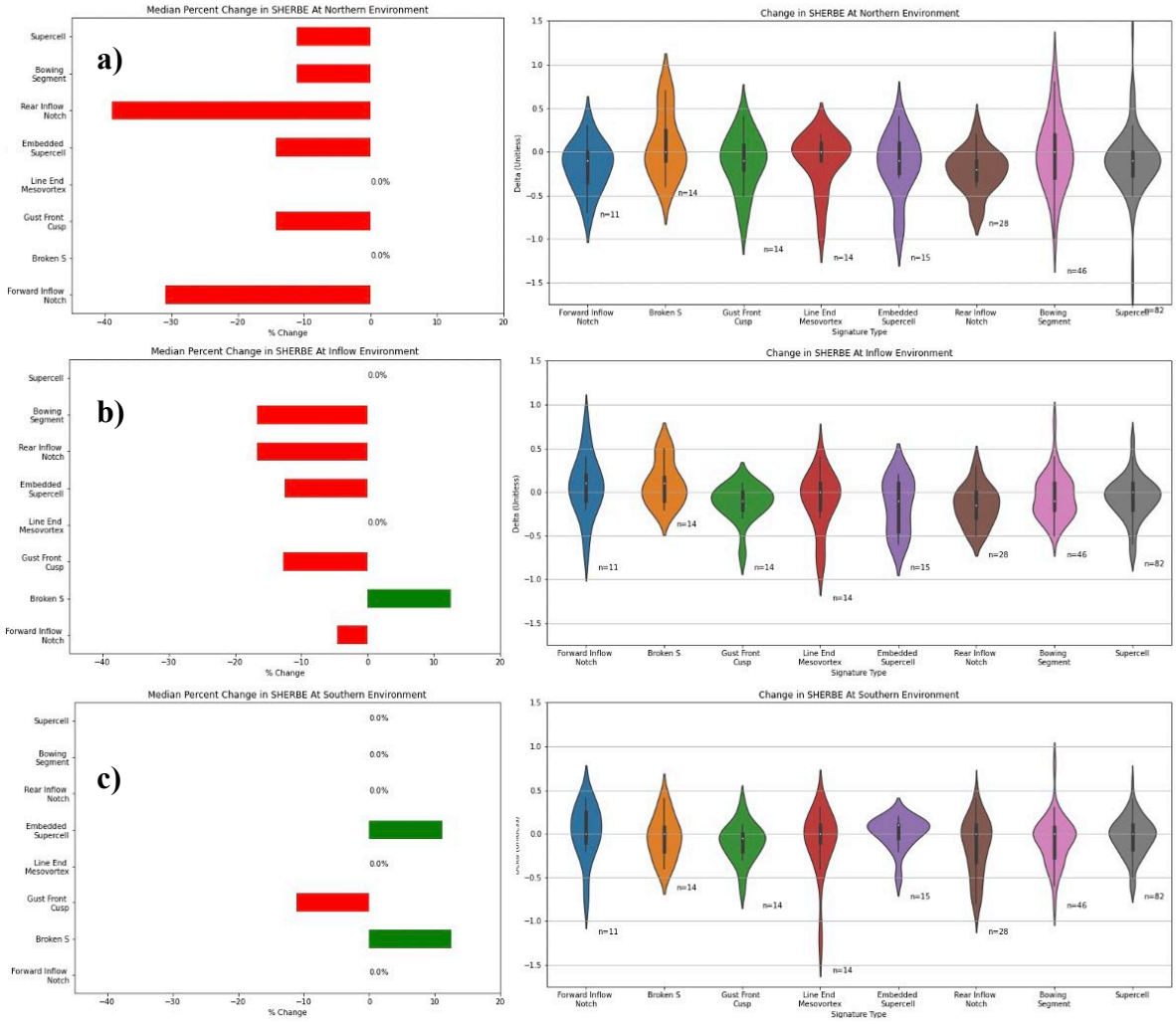

Figure 4.41: Median percent change (left) and raw deltas [(T-0)-(T-1)] (right) of severe hazards in environments with reduced buoyancy, effective layer shear variant (SHERBE) at a) northern, b) inflow, and c) southern environmental analysis points. On percent change plot: red bars represent negative percent changes; green bars represent positive percent changes. On deltas plot: dotted red line denotes "0" line with sample sizes annotated for each reflectivity signature.